Elasticity measurements
at extreme conditions:
application to FeO and FeNi-alloy

Von der Fakultät für Biologie, Chemie and Geowissenschaften
der Universität Bayreuth

zur Erlangung der Würde eines
Doktors der Naturwissenschaften
- Dr. rer. nat. -

genehmigte Dissertation

vorgelegt von
Diplom-Geochemikerin Anastasia Kantor
aus Moskau

Bayreuth, 2008

Prüfungsausschuß:

Prof. St. Peiffer, Universität Bayreuth   (Vorsitzender)

PD Dr. L. Dubrovinsky, Universität Bayreuth   (1. Gutachter)

Prof. St. KKlotz, Universität Paris   (2. Gutachter)

Prof. K. Bitzer, Universität Bayreuth

Prof. D. Rubie, Universität Bayreuth

Tag der Einreichung: 01. August 2007

Tag der wissenschaftlichen Kolloquiums: 05. Februar 2008

To the memory of my teacher

Egorov-Tismenko Yu. K.

Contents

Chapter 3. Results and discussion

Summary

The picture of Earth's deep interior is rapidly improving from the seismic tomography data and indicates more complexity than previously thought. The presence of Earth's seismic anisotropy requires the knowledge of fully anisotropic elasticity data for mineral phases. The single-crystal elastic constants of minerals, C_{ij}, are elements of the fourth-rank elasticity tensor, which relates stress to strain. The fact that elastic strain also defines seismic wave propagation, the elastic tensor of minerals can be applied to interpret the bulk mineralogy of the interior from seismological observation. Knowledge of the elasticity of crystalline materials as a function of pressures and temperature is also of primary interest for solid state physics because elastic tensors reveal the nature of interatomic interactions.

In order to determine the full elastic tensor of minerals under high pressure and temperature, several techniques are available, including ultrasonic interferometry and inelastic x-ray scattering methods. One of the most accurate techniques is high-frequency acoustic interferometry, which is capable for measuring sound wave velocities in very small samples under high pressures. The ultrasonic interferometry system operating at 0.5-2.0 gigahertz (GHz) frequencies was developed in the Bavarian Geoinstitut of the University of Bayreuth for *in situ* high pressure and temperature experiments. Here, GHz-ultrasonic interferometry has been used to study

the elastic properties of monoxide minerals such as FeO, liquids and nanocrystalline samples, each with particular importance to Earth or material sciences.

Fe_xO, wüstite, is the end-member phase of the (Mg,Fe)O solid solution, thought to be the most abundant non-silicate oxide in the mantle. The full elastic tensor of wüstite is determined by three elastic constants (C_{11}, C_{12}, C_{44}), which have been probed at high-pressures. At about 17-20 GPa, FeO is known to undergo a displacive cubic-to-rhomobhedral phase transformation. Prior to this transformation, we observe a pressure-induced mode softening of the C_{44} elastic constant. In addition, previously undetected discontinuities in the pressure derivatives of C_{11} and C_{12} at 4.7 ± 0.2 GPa were observed. This pressure is consistent with that of the magnetic ordering commencement, as was observed by high-pressure Mössbauer spectroscopy in a [57]Fe-enriched sample of FeO. The results indicate that an intermediate, partially magnetic but still cubic phase of FeO probably exists at room temperature and in pressure range from ~5 GPa to ~17 GPa.

In order to provide deeper knowledge of the magneto-elastic coupling in the material, neutron diffraction experiments were performed under ambient pressure and low temperatures. The results indicate that the magnetically ordered cubic phase of Fe_xO that was observed at high pressures also exists at ambient pressure at temperatures between 160 and 201 K.

Combined inelastic x-ray scattering and x-ray diffraction studies on a single crystal of $Fe_{0.95}O$ were performed up to 20 GPa at room temperature. The results show strong anelastic behaviour of wüstite, which should be accounted for at high pressure. Transition-metal oxides, non-stoichiometric compounds, and materials with complex mesostructure have some internal degree of freedom, and could therefore experience internal relaxation and show deviations from normal elastic behaviour.

A methodology to measure inelastic x-ray scattering in externally heated diamond anvil cells have also been developed. This technique was used to study polycrystalline *fcc*-$Fe_{0.78}Ni_{0.22}$ alloy at high pressures (up to 72 GPa) and temperature (up to 715 K). The bulk elasticity and its *P* and *T* derivatives were obtained for the material. No significant deviation of the elastic properties from those of pure ε−iron was observed and furthermore no deviation from Birch's law. Although the bulk elasticity of *fcc* Fe-Ni alloy and ε−Fe seem to be very similar, the elastic anisotropy of hexagonal and cubic phases should be quite different. If the metal phase in the inner core is not hexagonal, but cubic (or a mixture of the two phases exists), seismic anisotropy may provide a better way to discriminate between them two.

Zusammenfassung

Das Bild des Erdinneren, das in den letzten Dekaden mittels der seismischen Tomographie gewonnen wurde, deutet auf eine größere Komplexität hin als ursprünglich angenommen. Das Vorkommen von seismischer Anisotropie im oberen Erdmantel, in der Übergangszone und im unteren Mantel unterstreicht die Bedeutung der Anisotropie in der Mineralphysik bzw. in den Geowissenschaften. Die Einkristallkonstanten C_{ij} sind Elemente eines Tensors vierter Stufe, der eine infinitesimale Spannung mit einer infinitesimalen Deformation verbindet, welche wiederum Tensoren zweiter Stufe sind. Da die elastische Deformation von großer Bedeutung für die seismische Schallwellenausbreitung ist, kann der elastische Tensor von Mineralen ebenfalls für die Interpretation der mineralogischen Zusammensetzung des Erdinneren sowie für das Verständnis von Texturen und Strukturen, die von der Erdmantelbewegung herrühren, angewendet werden. Die Kenntnis des elastischen Verhaltens von Kristallen als Funktion von Druck und Temperatur ist zudem von großem Interesse für die Festkörperphysik/Materialwissenschaft, da der elastische Tensor Aufschluss über die inneratomaren Wechselwirkungen geben kann.

Mehrere Verfahren können angewendet werden, um alle Elemente des elastischen Tensors von Mineralen bei hohen Drücken und Temperaturen zu ermitteln. Zwei dieser Methoden sind die Ultraschallverfahren und die inelastische Photon - Phononstreuung. Eine

der genauesten Methode ist die akustische Hochfrequenzinterferometrie, mittels derer man die Schallwellengeschwindigkeiten von sehr dünnen Proben bis zu hohen Drücken bestimmen kann. Ein Ultraschall – Interferometriemeßstand, der in einem Frequenzbereich von 0,6 bis 2,1 GHz arbeitet, wurde am Bayerischen Geoinstitut, Universität Bayreuth für *in situ* Hochdruck– und Hochtemperaturexperimente entwickelt. Diese Methode wurde hier angewendet, um die elastischen Eigenschaften von Monoxiden wie FeO, Flüssigkeiten oder nanokristallinen Proben zu untersuchen; Materialien, die von besonderer Bedeutung für die Geo- bzw. Materialwissenschaften sind.

Fe_xO, Wüstit, das Endglied der (Mg,Fe)O Mischkristallreihe, ist wahrscheinlich das am häufigsten vorkommende nichtsilikatische Oxid im Erdmantel. Die drei unabhängigen Konstanten des elastischen Tensors *(C_{11}, C_{12}, C_{44})* wurden bis zu einem Druck von 10 GPa mittels GHz – Interferometrie bestimmt. Es ist bekannt, dass FeO zwischen 17-20 GPa eine displazive, kubische $\rightarrow$ rhomboedrische Phasentransformation durchläuft. Bevor dieser Phasenübergang stattfindet, beobachten wir ein druckinduziertes ,Aufweichen' (mode softening) der elastischen Konstante C_{44} um 20% bei 10 GPa. Darüber hinaus wurde eine bislang unbekannte Diskontinuität in den Druckableitungen von C_{11} und C_{12} bei $4,7 \pm 0,2$ GPa beobachtet. Das ist der Druckbereich bei dem die magnetische Ordnung einsetzt, wie mittels Hochdruck – Mössbauerspektroskopie an einer [57]Fe – angereicherten FeO - Probe festgestellt wurde. Dieses Ergebnis deutet darauf hin, dass vermutlich eine intermediäre, teilweise magnetische aber immer noch kubische Phase von FeO bei Zimmertemperatur im Druckbereich von ca. 5 bis 17 GPa existiert.

Um die die magneto-elastische Kopplung in Wüstit besser zu verstehen, wurden Neutronenstreuexperimente bei Atmosphärendruck und niedrigen Temperaturen durchgeführt. Die Ergebnisse lassen darauf schließen, dass die magnetisch geordnete kubische Phase von Fe_xO, die bei hohen Drücken beobachtet wurde, auch bei Normaldruck und bei Temperaturen zwischen 160 und 201 K existiert.

Inelastische Röntgenstreuexperimente zusammen mit Röntgenbeugung wurden an einem $Fe_{0,95}O$ Einkristall bei Drücken bis zu 20 GPa bei Zimmertemperatur durchgeführt. Diese Resultate deuten auf ein starkes anelastisches Verhalten von Wüstit hin, das bei hohen Drücken berücksichtigt werden muss. Übergangsmetalloxide, nicht - stöchiometrische Verbindungen sowie Materialien mit einer komplexen Mesostruktur besitzen interne Freiheitsgrade und könnten somit interne Relaxationsprozesse und Abweichungen vom normalen elastischen Verhalten aufweisen.

Wir haben ebenfalls eine Methode entwickelt, um inelastische Röntgenstreuexperimente in extern beheizten Diamantzellen durchzuführen. Mit dieser Technik wurde eine polykristalline fcc – $Fe_{0,78}Ni_{0,22}$ Legierung bei hohen Drücken (bis zu 72 GPa) und Temperaturen (bis zu 715 K) untersucht. Die Kompressions- und Schermoduli sowie deren P - und T - Ableitungen wurden bestimmt. Keine signifikante Abweichung von den elastischen Eigenschaften des reinen ε-Eisens wurde beobachtet, ebenso wenig eine Abweichung vom Birch – Gesetz.

Chapter 1

Introduction

The subject of this thesis is the experimental approach to the elastic properties of minerals at high pressure and temperature. Since elasticity of a crystal is a tensor value, a short explanation regarding different types of physical properties is necessary.

The physical properties are defined by relations between measurable quantities. Density, for example, is defined from a relation between mass and volume. Now both mass and volume may be measured without reference to direction, and, accordingly, density is a property that does not depend on direction. With the usual definitions of density and temperature it is meaningless to speak of measuring these quantities in any particular direction. Such non-directional physical quantities are called *scalars*, and the value of a scalar is completely specified by giving a single number. On the other hand, there are physical quantities of a different type, called *vectors*, which can only be defined with reference to directions. Mechanical force, velocity are well-known examples.

For a few properties, such as density, all crystals are isotropic. Cubic crystals happen to be isotropic for certain other properties as well, such as conductivity and refractive index, and this sometimes leads to the misconception that they are isotropic for all properties. Nevertheless, the symmetry elements of a cubic crystal are not the

same as those of a completely isotropic body, and, in fact, cubic crystals are anisotropic, often markedly so, for elasticity and some other properties. Cubic crystals must therefore be regarded as potentially anisotropic, and then it can be proved that, for certain properties, they are isotropic. All crystals are anisotropic for some of their properties. As an experimental fact, the electrical conductivity, for example, of many crystals does indeed vary with direction (Grimvall, 1999). In such cases the crystals are said to be anisotropic for the property in question.

In general, any vector may be conveniently represented by an arrow of definite length and direction. As an alternative to specifying a vector by giving its magnitude and direction one may, instead, choose three mutually perpendicular axes Ox_1, Ox_2, Ox_3 and give the *components* of the vector along them. The components are simply the projections of the vector on the axes. If the components of E are E_1, E_2, E_3, one can write

$$E = [E_1, E_2, E_3] \tag{1.1}$$

Thus, when the axes of reference have been chosen, a vector is completely specified by giving the values of its three components along the axes. A vector is also could be considered as *a tensor of the first rank*.

All physical quantities could be considered as tensors, such as (1) A tensor of zero rank (*a scalar*) is specified by a single number unrelated to any axes of reference; (2) A tensor of the first rank (*a vector*) is specified by three numbers, or components, each of which is associated with one of the axes of reference. And going ahead *a tensor of the second rank* is specified by nine numbers, or *components*, each of which is associated with a pair of axes (taken in a particular order). For example in order to specify the conductivity of a crystal, then, we have to specify the nine coefficients σ_{11}, σ_{12},.... They can be conveniently written down in a square array, thus:

$$\begin{bmatrix} \sigma_{11} & \sigma_{12} & \sigma_{13} \\ \sigma_{21} & \sigma_{22} & \sigma_{23} \\ \sigma_{31} & \sigma_{32} & \sigma_{33} \end{bmatrix} \qquad (1.2)$$

The first suffix gives the row and the second the column in which the component appears. σ_{11}, σ_{22}, σ_{33} are the components on the *leading diagonal* (Nye, 1987).

A scalar such as density is written without subscripts (for example, density ρ); the components of a vector have one subscript (for example, E_2); and the components of a second-rank tensor have two subscripts (for example, σ_{12}). The number of subscripts equals the rank of the tensor. The number of components is equal to d^n, where d is the number of dimensions and n is the rank of a tensor.

1.1 Elastic properties of solids

Central to the subject of elasticity are the strain and stress tensors and their relationship.

1.1.1 Macroscopic theory

Elastic strain

If a solid body undergoes an elastic distortion from an initial undistorted equilibrium state, then in order to describe this distortion, one should first identify each particle of the body in the equilibrium state by its location $x = (x_1, x_2, x_3)$ with respect to a Cartesian coordinate system. After the distortion has taken place, the

4

particle that was originally at *x* is located at a new position *X*, and to get there has undergone a displacement *u(x)* = *X(x)* - *x*. The existence of a displacement field *u* does not in itself imply distortion of the body, since it could correspond to a pure translation or pure rotation. If there is to be a local distortion, then the absolute distance between neighbouring particles must change. Two arbitrarily chosen particles at points *x* and *x+δx*, after the displacement has taken place, will be at *X(x)* and *X(x+δx)*. The original distance between the particles, *δl*, is given by

$$\delta l^2 = |\delta x| = \delta x_1^2 + \delta x_2^2 + \delta x_3^2 \tag{1.3}$$

The separation of the particles after the displacement has taken place, *δL*, assuming that *X(x+δx)* can be expanded in a Taylor series in δx_i, is given by

$$\delta L^2 = |X(x+\delta x) - X(x)| = \delta X_k \delta X_k = \frac{\partial X_k}{\partial x_i}\frac{\partial X_k}{\partial x_j}\delta x_i \delta x_j \tag{1.4}$$

The change in the square of the separation is given by

$$\delta L^2 - \delta l^2 = 2\eta_{ij}\delta x_i \delta x_j \quad , \tag{1.5}$$

where

$$\eta_{ij} = 0.5\left(\frac{\partial X_k}{\partial x_i}\frac{\partial X_k}{\partial x_j} - \delta_{ij}\right) \tag{1.6}$$

is called the *Lagrangian strain*, and δ_{jk} is the Kronecker delta function. Equivalently, the strain in terms of the displacement field gradients could be expressed by

$$\eta_{ij} = 0.5\left(\frac{\partial u_i}{\partial x_j} + \frac{\partial u_j}{\partial x_i} + \frac{\partial u_k}{\partial x_i}\frac{\partial u_k}{\partial x_j}\right) \tag{1.7}$$

For infinitesimal displacements, the product term in Eq. 1.7 can be dropped, leading to the definition of the *infinitesimal strain*

$$\varepsilon_{ij} = 0.5\left(\frac{\partial u_i}{\partial x_j} + \frac{\partial u_j}{\partial x_i}\right) \tag{1.8}$$

The nine components of strain ε_{ij}, $i, j = 1, 2, 3$ collectively constitute a second-rank tensor, the strain tensor $\{\varepsilon_{ij}\}$.

Stress

Figure 1.1 depicts an "infinitesimal" cube centred on the point x in a medium. The state of stress in the medium at point x is characterized by the forces per unit area acting across the faces of the cube. Only the three faces shown should be considered, since the forces across opposite faces are equal and opposite, for a uniform stress.
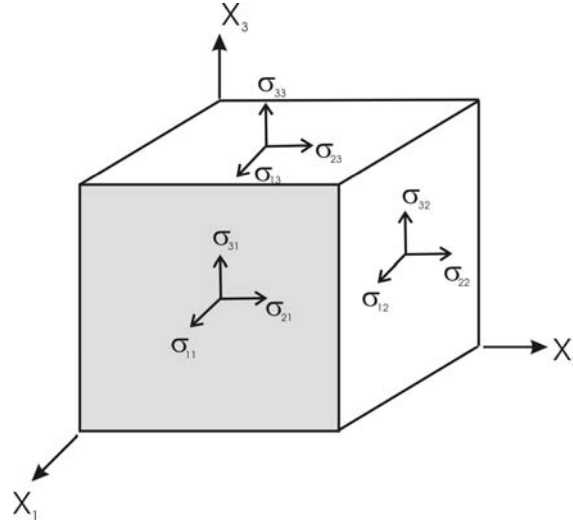

Fig. 1.1.1. The forces on the faces of a unit cube in a homogeneously stressed body.

The nine quantities

$$\sigma_{ij} = {}_{\delta A}\underline{\lim}_{0} \frac{\delta F_i^{\,j}}{\delta A} \; ; \; i, j = 1, 2, 3, \tag{1.9}$$

where $\delta F_i^{\,j}$, is the i'th component of the force acting across the surface facing outwards along the x_j direction and δA is the area of that face, constitute the Cauchy stress tensor $\{\sigma_{ij}\}$. The three diagonal components σ_{ij} are called the *normal components* of

stress, and the remaining six off-diagonal components σ_{ij}, $i \neq j$ are the shear components.

In order for the moment of forces acting on the cube to tend to zero sufficiently rapidly when the size of the cube is reduced to zero (to avoid infinite angular acceleration), the stress tensor must be symmetric with respect to interchange of indices, i.e.,

$$\sigma_{ij} = \sigma_{ji} \tag{1.10}$$

Thereby the torques produced by pairs of forces such as δF_i^j and δF_j^i cancel. Thus there are only six independent stress components. The relation (1.10) continues to hold even when the stress is inhomogeneous, when the body is not in a static equilibrium, and when body-forces (but not body-torques) are present.

One can describe any general stress, by a suitable choice of axes, as the sum of (1) a hydrostatic stress and (2) a shear stress (i.e. a stress whose normal components are all zero). The first could be expressed by matrix

$$\begin{bmatrix} -p & 0 & 0 \\ 0 & -p & 0 \\ 0 & 0 & -p \end{bmatrix}.$$

Pure shear stress is a special case of biaxial stress and could be expressed as

$$\begin{bmatrix} -\sigma & 0 & 0 \\ 0 & \sigma & 0 \\ 0 & 0 & 0 \end{bmatrix}.$$

Stress is a second-rank tensor, but there is an important distinction between the stress tensor and all the other second-rank tensors. Tensors, which measure crystal properties (such as the permittivity and the magnetic susceptibility, represented by quadrics), have definite orientations within a crystal, and they must conform to the crystal symmetry. They are called *matter tensors*. The stress tensor, on the other hand, in common with the strain tensor, can have any orientation within a crystal, and it can

exist just as well in isotropic bodies like glass as in anisotropic crystals. The stress tensor does not represent a crystal property but is akin to a "force" impressed on the crystal; in this respect it is like an electric field, which can, of course, have an arbitrary direction in a crystal. Such tensors are called *field tensors* (Nye, 1987).

Hooke's law

An ideal elastic body becomes strained when subjected to stress, and when the stresses are removed, the strains disappear. Moreover, in the limit of small stresses and strains, these two quantities are linearly related. Linear relations between the components of stress and the components of strain are known generally as *Hooke's law*.

Each stress component, in general, depends on all the strain components, and vice versa. The materials or constitutive relationship can be written in two ways,

$$\sigma_{ij} = c_{ijkl}\varepsilon_{kl} \tag{1.11}$$

and its inverse

$$\varepsilon_{ij} = s_{ijkl}\sigma_{kl}. \tag{1.12}$$

The $3^4 = 81$ coefficients c_{ijkl} are called the elastic *stiffnesses* of the material and are a measure of the resistance of the material to elastic deformation, and the 81 coefficients s_{ijkl} are called the elastic compliances and are a measure of the ease of deformation. The elastic *stiffnesses* and compliances form fourth-rank Cartesian tensors that are reciprocally related, i.e.,

$$s_{ijkl}c_{klmn} = \delta_{im}\delta_{jn} \tag{1.13}$$

8

Stress and strain are field quantities, i.e., they can vary from point to point in a body and also depend on time, whereas the compliances and stiffnesses are materials properties, being constants for a particular homogeneous solid.

<u>Index symmetries</u>

Both the strain and stress tensors are symmetrical with respect to interchange of indices i and j, and there are thus only six independent components of stress and strain. In consequence there are only $6^2 = 36$ independent stiffnesses and compliances. Using only tow suffixes makes it possible to use the matrix notation. Both the stress and strain components are written with a single suffix running from 1 to 6 simply by replacing each pair of indices $i\,j$ with a single index $\alpha = 1, 2, 3$.... 6 as follows:

Tensor notation	11	22	33	23, 32	31, 13	12, 21
Matrix notation	1	2	3	4	5	6

In the s_{ijkl} and the c_{ijk} the first two suffixes are abbreviated into a single one, and the last two are abbreviated in the same way, according to the same scheme.

At the same time factors of 2 and 4 are introduced as follows:

$s_{ijkl} = S_{mn}$ when m and n are 1, 2 or 3,

$2\,s_{ijkl} = S_{mn}$ when either m or n are 4, 5 or 6,

$4\,s_{ijkl} = S_{mn}$ when both m and n are 4, 5 or 6.

The arrays of S_{ij} and C_{ij} written out in squares, thus:

$$\begin{pmatrix} S_{11} & S_{12} & S_{13} & S_{14} & S_{15} & S_{16} \\ S_{21} & S_{22} & S_{23} & S_{24} & S_{25} & S_{26} \\ S_{31} & S_{32} & S_{33} & S_{34} & S_{35} & S_{36} \\ S_{41} & S_{42} & S_{43} & S_{44} & S_{45} & S_{46} \\ S_{51} & S_{52} & S_{53} & S_{54} & S_{55} & S_{56} \\ S_{61} & S_{62} & S_{63} & S_{64} & S_{65} & S_{66} \end{pmatrix} \text{ and } \begin{pmatrix} C_{11} & C_{12} & C_{13} & C_{14} & C_{15} & C_{16} \\ C_{21} & C_{22} & C_{23} & C_{24} & C_{25} & C_{26} \\ C_{31} & C_{32} & C_{33} & C_{34} & C_{35} & C_{36} \\ C_{41} & C_{42} & C_{43} & C_{44} & C_{45} & C_{46} \\ C_{51} & C_{52} & C_{53} & C_{54} & C_{55} & C_{56} \\ C_{61} & C_{62} & C_{63} & C_{64} & C_{65} & C_{66} \end{pmatrix} \quad (1.14)$$

are matrices, (S_{ij}) and (C_{ij}). As with the piezoelectric moduli one should remember that, in spite of their appearance with two suffixes, the S_{ij} and C_{ij} are not the components, and so do not transform like the components, of a second-rank tensor (Nye, 1987). To transform them to other axes it is necessary to go back to the full tensor notation, c_{ijkl} and s_{ijkl}.

<u>The energy of a strained crystal</u>

Consider a body, which in the unstrained state has the form of a unit cube, and suppose it is subjected to a small homogeneous strain with components ε_i. Now let the strain components all be changed to $\varepsilon_i + d\varepsilon_i$. Then the work done by the stress components of acting on the cube faces is

$$dW = \sigma_i d\varepsilon_i \qquad (i = 1, 2,..., 6) \tag{1.15}$$

First suppose that the strain component ε_i is increased to $\varepsilon_i + d\varepsilon_i$, while the other strain components, and the position of the centre of the cube, remain unaltered. The two faces perpendicular to Ox_1, will move outwards by amounts $\frac{1}{2}d\varepsilon_i$ the other four faces will simply increase in area, but the positions of their centres will be unchanged. The work done by the forces on these last four faces is therefore zero. The work done on the faces perpendicular to Ox_1, equals their displacement multiplied by the normal component of the force on them; it is therefore $2\sigma_1\frac{1}{2}d\varepsilon_1 = \sigma_1 d\varepsilon_1$. This is the term with $i = 1$ in (1.15); the terms with $i = 2$ and $i = 3$ are obtained in a similar way.

Now let the cube be sheared by making the two faces perpendicular to Ox_2, move in opposite directions parallel to Ox_3, so as to increase the strain component ε_4 to $\varepsilon_4 + d\varepsilon_4$. In this deformation (simple shear) the mid-points of the faces perpendicular to Ox_2, each move a distance $\frac{1}{2}d\varepsilon_4$. The component of force on the faces in this direction is ε_4. The work done by the forces is therefore $2\sigma_4\frac{1}{2}d\varepsilon_4 = \sigma_4 d\varepsilon_4$. The terms with $i = 5$ and $i = 6$ in (1.15) are obtained in a similar way (Nye, 1987).

It is readily shown that the corresponding equation to (1.15) in tensor notation is

$$dW = \sigma_{ij}d\varepsilon_{ij} \quad (i, j = 1, 2,..., 6) \tag{1.16}$$

When the change is isothermal and reversible dW may be equated with the increase in free energy $d\Psi$. The fact that $d\Psi$ is a perfect differential gives that

$$C_{ij} = C_{ji}, \qquad S_{ij} = S_{ji}; \tag{1.17) (1.18}$$

and the strain energy per unit volume is

$$\tfrac{1}{2} C_{ij}\varepsilon_i\varepsilon_j \tag{1.19}$$

(1.17) and (1.18) reduce the number of independent compliances and stiffnesses from 36 to 21, and the number is further reduced by the material's symmetry.

Anisotropic solids

There are many types of materials that are not isotropic: single crystals, various types of superlattices, fiber-reinforced composites, etc. However, most anisotropic solids do have some degree of symmetry, although it is not full rotational symmetry. There are a limited number of symmetry types. Since the stress-strain relationship is invariant under inversion, the appropriate symmetry classification is by Laue groups. For crystals this means adding inversion where there is none, and this collapses the 32 crystal point symmetry groups into 11 Laue groups. The forms of the elastic constant matrices for the different symmetries are shown in Table 1-1. In each case the Laue group (or groups) is given, followed by the corresponding point groups in brackets.

Triclinic. N [1, -1]. This is the absence of any material symmetry other than inversion. There are no relationships between the 21 elastic constants, and none are zero.

Monoclinic. M [2, m, 2/m]. There is a single mirror symmetry plane with a twofold rotational symmetry axis perpendicular to it. The elastic stiffness matrix for

monoclinic symmetry has only 13 independent components, and the same is true for the compliance matrix S_{mn}.

Orthorhombic. O [222, mm2, mmm]. This symmetry is characterized by three mutually perpendicular mirror symmetry planes and twofold rotational symmetry axes perpendicular to these planes. The elastic constant matrix in orthorhombic symmetry has nine independent nonzero components. Examples: crystals such as aragonite ($CaCO_3$), uranium, and the olivines (a major component of the Earth's upper mantle).

Hexagonal. H I [622, 6mm, -6m2, 6/mmm] and H II [6, -6, 6/m]. There are five independent elastic constants for these groups. Whereas the forms of the second-order elastic constants for the Laue groups H I and H II are the same, this is not true of the third- and higher-order elastic constants.

Tetragonal. T I [422, 4mm, -42m, 4/mmm]. This can be regarded as orthorhombic with the addition of a fourfold rotational symmetry axis along one of the crystallographic axis and mirror symmetry planes containing this axis (x_3) and bisecting the angles between two other axes (x_1 and x_2). The equivalence of the x_1 and x_2 axes has the effect of reducing the number of independent elastic constants from the nine of orthorhombic symmetry to six, through the equalities $C_{11} = C_{22}$, $C_{23} = C_{13}$, and $C_{44} = C_{55}$. Examples: crystals such as $BaTiO_3$, rutile (TiO_2), and zircon ($ZrSiO_4$).

T II [4, -4, 4/m]. These crystals lack the vertical symmetry planes, and as a result have a seventh elastic constant $C_{16} = - C_{26}$, $S_{16} = -S_{26}$. Since the special direction for the x_1 axis does not coincide with any crystallographic direction, the number of parameters characterizing the elastic constant matrix is still seven. The higher-order elastic constants are also different for Laue groups T I and T II.

Trigonal. R I [32, 3m, -3m]. This is characterized by the presence of a threefold symmetry axis, taken to be along the x_3 direction, three equivalent mirror planes containing this axis, and three twofold axes normal to these planes, with the x_1 axis being parallel to one of these diad axes. The elastic constant matrix is that of a hexagonal solid, but with a sixth independent elastic constant $C_{14} = - C_{24} = C_{56}$ and $S_{14} = - S_{24} = 0.5 S_{56}$. Examples: common crystals such as quartz, sapphire, and calcite.

R II [3, -3]. These crystals lack the vertical symmetry planes, and as a result have a seventh elastic constant $C_{15} = - C_{25} = - C_{46}$, $S_{15} = - S_{25} = -0.5 S_{46}$.

Cubic. C I [432, -43m, m3m] and C II [23, m3]. Three independent elastic constants: $C_{11} = C_{22} = C_{33}$, $C_{12} = C_{23} = C_{13}$, and $C_{44} = C_{55} = C_{66}$. The crystals of many elements (e.g., Si, Ge, diamond, etc.), alloys, and compounds are cubic and have had their elastic constants measured. The forms of the third- and higher-order elastic constants differ for the Laue groups C I and C II.

Isotropic solids

An isotropic solid is one in which the properties are the same in all directions. Examples of isotropic solids are amorphous materials (glasses), polycrystalline materials with no texture, ceramics, and so on. For isotropic solids *engineering constants E, G, K*, and ν or the *Lamé constants λ* and μ are favoured. For an isotropic solid the following is true:

(1) A pure shear strain, say ε_4, is accompanied by the single shear stress σ_4, and vice versa. All components of S_{mn} and C_{mn}, for $m = 4, 5, 6$ and $m \neq n$, are therefore identically zero.

(2) Any permutation of the x_1, x_2, and x_3 axes leaves the stiffness and compliance tensors unchanged, so $C_{11} = C_{22} = C_{33}$, $C_{44} = C_{55} = C_{66}$, and $C_{12} = C_{23} = C_{13}$.

(3) The fact that the stiffness and compliance matrices must be unchanged by any rotation of the axes imposes the additional constraint $C_{11} = C_{12} + 2C_{44}$, or equivalently $S_{11} = S_{12} + 0.5\ S_{44}$.

There are thus only two independent elastic constants. The form of the elastic constant matrix for isotropy (and the other material symmetries) is shown in Table 1-1. There the independent constants have been taken to be C_{11} and C_{12}. There are two other widely used choices of elastic constants for isotropic solids.

Lame Constants are represented by the Greek letters λ and μ, and in terms of them

$$C_{12} = \lambda, \qquad C_{44} = \mu, \qquad \text{and} \qquad C_{11} = \lambda + 2\mu, \qquad (1.20)$$

and

$$c_{ijkl} = \lambda \delta_{ij}\delta_{kl} + \mu\left(\delta_{ik}\delta_{jl} + \delta_{il}\delta_{jk}\right) \qquad (1.21)$$

Engineering Constants. In a pure shear test one obtains the shear or rigidity modulus G as the applied shear stress divided by the resulting shear strain, and hence

$$G = \frac{1}{S_{44}} = \mu \qquad (1.22)$$

Similarly, in a simple tensile test, a known uniform tensile stress is applied to a rod and the resulting longitudinal and transverse strains are measured. Young's modulus E is defined as the normal (tensile) stress divided by the longitudinal strain:

$$E = \frac{1}{S_{11}} = \frac{\mu(3\lambda + 2\mu)}{(\lambda + \mu)}, \qquad (1.23)$$

14

Table 1-1. Forms of the $[C_{mn}]$ matrix ($C' = 0.5\,(C_{11} - C_{12})$; $\overline{C}_{mn} = -\,C_{mn}$).

$$
\begin{pmatrix}
C_{11} & C_{12} & C_{13} & C_{14} & C_{15} & C_{16} \\
C_{12} & C_{22} & C_{23} & C_{24} & C_{25} & C_{26} \\
C_{13} & C_{23} & C_{33} & C_{34} & C_{35} & C_{36} \\
C_{14} & C_{24} & C_{34} & C_{44} & C_{45} & C_{46} \\
C_{15} & C_{25} & C_{35} & C_{45} & C_{55} & C_{56} \\
C_{16} & C_{26} & C_{36} & C_{46} & C_{56} & C_{66}
\end{pmatrix}
$$

Triclinic N

$$
\begin{pmatrix}
C_{11} & C_{12} & C_{13} & 0 & C_{15} & 0 \\
C_{12} & C_{22} & C_{23} & 0 & C_{25} & 0 \\
C_{13} & C_{23} & C_{33} & 0 & C_{35} & 0 \\
0 & 0 & 0 & C_{44} & 0 & C_{46} \\
C_{15} & C_{25} & C_{35} & 0 & C_{55} & 0 \\
0 & 0 & 0 & C_{46} & 0 & C_{66}
\end{pmatrix}
$$

Monoclinic M

$$
\begin{pmatrix}
C_{11} & C_{12} & C_{13} & 0 & 0 & 0 \\
C_{12} & C_{22} & C_{23} & 0 & 0 & 0 \\
C_{13} & C_{23} & C_{33} & 0 & 0 & 0 \\
0 & 0 & 0 & C_{44} & 0 & 0 \\
0 & 0 & 0 & 0 & C_{55} & 0 \\
0 & 0 & 0 & 0 & 0 & C_{66}
\end{pmatrix}
$$

Orthorombic O

$$
\begin{pmatrix}
C_{11} & C_{12} & C_{13} & 0 & 0 & 0 \\
C_{12} & C_{22} & C_{23} & 0 & 0 & 0 \\
C_{13} & C_{23} & C_{33} & 0 & 0 & 0 \\
0 & 0 & 0 & C_{44} & 0 & 0 \\
0 & 0 & 0 & 0 & C_{55} & 0 \\
0 & 0 & 0 & 0 & 0 & C'
\end{pmatrix}
$$

Hexagonal H I and H II

$$
\begin{pmatrix}
C_{11} & C_{12} & C_{13} & 0 & 0 & 0 \\
C_{12} & C_{11} & C_{13} & 0 & 0 & 0 \\
C_{13} & C_{13} & C_{33} & 0 & 0 & 0 \\
0 & 0 & 0 & C_{44} & 0 & 0 \\
0 & 0 & 0 & 0 & C_{44} & 0 \\
0 & 0 & 0 & 0 & 0 & C_{66}
\end{pmatrix}
$$

Tetragonal T I

$$
\begin{pmatrix}
C_{11} & C_{12} & C_{13} & 0 & 0 & C_{16} \\
C_{12} & C_{11} & C_{13} & 0 & 0 & \overline{C}_{16} \\
C_{13} & C_{13} & C_{33} & 0 & 0 & 0 \\
0 & 0 & 0 & C_{44} & 0 & 0 \\
0 & 0 & 0 & 0 & C_{44} & 0 \\
C_{16} & \overline{C}_{16} & 0 & 0 & 0 & C_{66}
\end{pmatrix}
$$

Tetragonal T II

$$
\begin{pmatrix}
C_{11} & C_{12} & C_{13} & C_{14} & 0 & 0 \\
C_{12} & C_{11} & C_{13} & \overline{C}_{14} & 0 & 0 \\
C_{13} & C_{13} & C_{33} & 0 & 0 & 0 \\
C_{14} & \overline{C}_{14} & 0 & C_{44} & 0 & 0 \\
0 & 0 & 0 & 0 & C_{44} & C_{14} \\
0 & 0 & 0 & 0 & C_{14} & C'
\end{pmatrix}
$$

Trigonal R I

$$
\begin{pmatrix}
C_{11} & C_{12} & C_{13} & C_{14} & C_{15} & 0 \\
C_{12} & C_{11} & C_{13} & \overline{C}_{14} & \overline{C}_{15} & 0 \\
C_{13} & C_{13} & C_{33} & 0 & 0 & 0 \\
C_{14} & \overline{C}_{14} & 0 & C_{44} & 0 & \overline{C}_{15} \\
C_{15} & \overline{C}_{15} & 0 & 0 & C_{44} & C_{14} \\
0 & 0 & 0 & \overline{C}_{15} & C_{14} & C'
\end{pmatrix}
$$

Trigonal R II

$$
\begin{pmatrix}
C_{11} & C_{12} & C_{12} & 0 & 0 & 0 \\
C_{12} & C_{11} & C_{12} & 0 & 0 & 0 \\
C_{12} & C_{12} & C_{11} & 0 & 0 & 0 \\
0 & 0 & 0 & C_{44} & 0 & 0 \\
0 & 0 & 0 & 0 & C_{44} & 0 \\
0 & 0 & 0 & 0 & 0 & C_{44}
\end{pmatrix}
$$

Cubic C I and C II

$$
\begin{pmatrix}
C_{11} & C_{12} & C_{12} & 0 & 0 & 0 \\
C_{12} & C_{11} & C_{12} & 0 & 0 & 0 \\
C_{12} & C_{12} & C_{11} & 0 & 0 & 0 \\
0 & 0 & 0 & C' & 0 & 0 \\
0 & 0 & 0 & 0 & C' & 0 \\
0 & 0 & 0 & 0 & 0 & C'
\end{pmatrix}
$$

Isotropic

and Poisson's ratio ν is the negative of the ratio of the transverse strain to the longitudinal strain, i.e,

$$\nu = -\frac{S_{12}}{S_{11}} = -E \cdot S_{12} = \frac{\lambda}{2(\lambda + \mu)}. \qquad (1.24)$$

The bulk modulus is the negative of pressure divided by the relative change in volume, and hence

$$K = \frac{1}{3(S_{11} + S_{12})} = \frac{E}{3(1 - 2\nu)}. \qquad (1.25)$$

Rocks in most cases can be considered as isotropic solids. Although rocks consist of anisotropic crystals, their size is negligibly small compared to the sampling scale and relative orientation is nearly random in many cases. In geophysics engineering constants K and G are used to characterize bulk elasticity in the Earth. Recent developments of seismic tomography (Zhao, 2000; Romanowicz, 2003) reveal the existence of some elastic anisotropy in the Earth's interior that could not be described in isotropic assumption.

Thermodynamic considerations

As a broad generalization, static methods of measurement, if executed sufficiently slowly so that thermal equilibrium with the environment is maintained, yield isothermal values of the elastic constants, whereas dynamic methods, in which there is little heat conduction per cycle, yield adiabatic values. The adiabatic stiffnesses are derived from the internal energy per unit mass $U\ (\eta,\ S)$, and the isothermal stiffnesses are derived from the Helmholz free energy per unit mass $F\ (h,\ T)$, (S = entropy, T = absolute temperature, η = Lagrangian strain):

16

$$c_{ijkl}^{S} = \rho \left(\frac{\partial^2 U}{\partial \eta_{ij} \partial \eta_{kl}} \right)_S, \qquad c_{ijkl}^{T} = \rho \left(\frac{\partial^2 F}{\partial \eta_{ij} \partial \eta_{kl}} \right)_T \qquad (1.26)$$

Some situations cannot be categorized in this simple way. At the very high frequencies explored by neutron scattering, for example, the thermal phonon population is not able to relax to the rapidly changing strain field, and it is the zero sound elastic constants that are measured. At the other extreme, e.g., in the infrasonic measurement of the shear modulus of a fiber with the torsion pendulum method, one is justified in asking whether it is the adiabatic or isothermal elastic constants that are measured, or perhaps something in between. In most cases the differences between these various moduli are of the order of 1% or less, which is comparable to the experimental error in absolute measurements, and the distinction is ignored. It is only in solids with exceptionally large thermal expansion coefficients, such as certain polymers and composites, that the differences are appreciable.

Viscoelasticity

In all real materials there is some degree of attenuation of an acoustic wave as it propagates through the medium. Often this attenuation is ascribed to a frequency-dependent viscoelasticity of the material (which is an assumption, however, that overlooks scattering and other mechanisms that can complicate the attenuation process). In viscous fluids the stress is proportional, not to the strain, but to the time rate of change of strain. One therefore thinks of a viscoelastic solid as one in which the relationship between stress and strain takes the form:

$$\sigma_{ij} = \chi_{ijkl} \varepsilon_{ijkl} \frac{\partial \varepsilon_{kl}}{\partial t} \qquad (1.27)$$

The viscosity coefficients χ_{ijkl} form a fourth-rank tensor, which is positive definite and has the same symmetry properties as c_{ijkl} (Nowick and Berry, 1972).

<u>Dispersion and anelastic relaxation</u>

When there are relaxation processes in a system with a characteristic lifetime τ, then the velocities and elastic constants measured at low frequencies, $\omega\tau << 1$, and at high frequencies, $\omega\tau >> 1$, differ to some degree, since in the former case relaxation takes place within a cycle of the motion and in the latter case it does not. Another major source of dispersion is the microstructure of a solid, whether this happens to be the layers of a composite or the crystal lattice of a single crystal. If the microstructure is periodic, then this introduces a characteristic system of dispersion curves/surface and pass- and stop-bands. Starting from the long wavelength low-frequency limit, the dispersion relation $\omega(k)$ tends to flatten out with increasing frequency, corresponding to a decrease in velocity. For crystals, in most cases this effect only becomes evident in the high-gigahertz frequency range as the wave vector starts approaching the Brillouin zone boundary. A lattice dynamics approach is then usually adopted in interpreting the observations. In crystals that lack a centre of inversion in their structure, there is a dispersive effect, called *acoustic gyrotropy*, which is observable even at low-megahertz frequency. This causes a splitting between the velocities of right and left circularly polarized waves in directions where they would otherwise be degenerate, except where they lie at the intersection of symmetry planes. This effect of gyrotropy is well described by a complex wave-vector-dependent elastic constant matrix:

$$c_{ijkl}(k) = c_{ijkl} + id_{ijklm}k_m + ..., \tag{1.28}$$

where d_{ijklm} is a gyrotropic coefficient (Every, 1987a).

<u>Piezoelectric stiffening of elastic constants</u>

Crystals that lack a centre of inversion in their crystal structure, with the exception of point symmetry group 432, are piezoelectric. As a consequence, an

acoustic wave in such a medium is accompanied by an oscillating electric field, which in turn, through the piezoelectric coupling, modifies the stress field. The medium as a result appears elastically stiffer, with effective piezoelectrically stiffened elastic constants

$$c_{ijkl} = c_{ijkl}^{E} + \frac{e_{ijr}e_{kls}n_{r}n_{s}}{\varepsilon_{pq}^{\varepsilon}n_{p}n_{q}},$$ (1.29)

where c_{ijkl}^{E}, are the elastic stiffnesses measured at constant electric field, e_{ijr} is the piezoelectric stress tensor, and $\varepsilon_{pq}^{\varepsilon}$ is the permittivity tensor at constant strain. These effective elastic constants are used rather than the normal elastic stiffnesses in calculating acoustic velocities. In some crystals, such as lithium niobate and Rochelle salt, piezoelectric stiffening has a pronounced effect on acoustic velocities, causing changes of more than 20% in some directions, whereas in others the coupling is very small and the stiffening effect can be ignored (Every, 1987b).

Equation of state (EoS)

An equation of state ($f(P,V,T) = 0$) is one of the most important characteristics of the Earth's materials. Generally, thermodynamics gives:

$$P = -\left(\frac{\partial F}{\partial V}\right)_{T} \qquad \text{and} \qquad V = \left(\frac{\partial G}{\partial P}\right)_{T} \qquad \text{isothermal EoS}$$

$$T = \left(\frac{\partial H}{\partial S}\right)_{P} \qquad \text{and} \qquad S = -\left(\frac{\partial G}{\partial T}\right)_{P} \qquad \text{isobaric EoS}$$

$$P = -\left(\frac{\partial E}{\partial V}\right)_{S} \qquad \text{and} \qquad P = -\left(\frac{\partial H}{\partial P}\right)_{S} \qquad \text{adiabatic EoS}$$

An explicit analytical EoS can only be written for an ideal gas, where interatomic interactions are absent: in this case there are no problems in the analytical representation of the interatomic potential, and entropy can be easily and exactly calculated using the Sackur-Tetrode relation. The classical ideal gas EoS is: $PV_m = RT$, where V_m is the molar volume. For solids and liquids interatomic interactions are essential, and all existing analytical EoSs are by necessity approximate.

Elasticity theory is used to construct the simplest EoSs. The simplest EoS is just the definition of the bulk modulus: $K_T = -V(\partial P/\partial V)_T$. However, at certain point strains cannot be considered as being infinitesimal and the Hook's low is no more valid. That is why this EoS is valid only in a very narrow pressure range: because the bulk modulus K in fact changes rapidly with pressure. The pressure variation of K is determined by the interatomic forces acting within the solid – these forces must be accounted for by accurate EoS formulations.

Assuming that K varies linearly with pressure and denoting $K_0^{'} = (\partial K/\partial P)_{T,P=0}$, the Murnaghan EoS is obtained:

$$P = K_0/K_0^{'}\left[(V/V_0)^{-K_0^{'}} - 1\right] \qquad (1.30)$$

This simple EoS works well in the compression range $|(V - V_0)/V_0| < 0.1 - 0.2$. At larger compressions higher-order derivatives of K become important. Of course, these nonlinearities can be formally incorporated as well, resulting in a more complicated EoS. Better convergence is obtained if, instead of K as a function of pressure, an approximate model for the energy as a function of $x = V_0/V$ or some other measure of strain is used. Using this method, some of the most commonly used EoSs are obtained.

Birch-Murnaghan EoSs (Poirier, 2000).

These EoSs are based on the polynomial expansion of the energy:

$$E = E_0 + af^2 + bf^3 + cf^4 + ... \tag{1.31}$$

in powers of the Eulerian strain f_E:

$$f_E = \frac{1}{2}\left[(V_0 / V)^{2/3} - 1 \right] \tag{1.32}$$

It is advantageous to use the Eulerian finite strain rather than the Lagrangian strain:

$$\eta = \frac{1}{2}\left[1 - (V / V_0)^{2/3} \right], \tag{1.33}$$

because Eulerian strain leads to a better description of the correct $E(V)$ dependence with fewer terms in the expansion (1.31). At infinite pressure, Eulerian strain is infinite, whereas Lagrangian strain remains finite. However, for infinitesimal strains both definitions become equivalent, and

$$df_E = d\eta = da / a_0 = -\frac{1}{3}(dV)/V_0 \tag{1.34}$$

It can be shown that generally

$$9V_0 K_0 = \left(\frac{1}{f} \right)\left(\frac{\partial E}{\partial f} \right)_T \tag{1.35}$$

Truncating (1.31) on the second-order term:

$$E = E_0 + af^2, \tag{1.36}$$

and, noting that

$$a = \left(\frac{9}{2} \right) K_0 V_o, \tag{1.37}$$

it is easy to obtain (see Poirier, 2000) the second-order Birch-Murnaghan EoS:

$$P = 3K_0 f (1 + 2f)^{5/2} \tag{1.38}$$

Or, in a different form:

$$P = \left(\frac{3}{2} \right) K_0 \left[(V_0 / V)^{7/3} - (V_0 / V)^{5/3} \right] \tag{1.39}$$

$$E = E_0 + \left(\frac{9}{8} \right) K_0 V_0 \left[(V_0 / V)^{2/3} - 1 \right]^2 \tag{1.40}$$

Third-order BM EoS is

$$P(V) = \frac{3}{2} K_0 \left[(V_0/V)^{7/3} - (V_0/V)^{5/3} \right] \left\{ 1 + \xi \left[(V_0/V)^{2/3} - 1 \right] \right\},$$ (1.41)

$$E(V) = E(V_0) + \frac{3}{2} K_0 V_0 \times$$
$$\times \left[\frac{3}{2}(\xi-1)(V_0/V)^{2/3} + \frac{3}{4}(1-2\xi)(V_0/V)^{4/3} + \frac{1}{2}\xi(V_0/V)^{6/3} - (2\xi-3)/4 \right]$$ (1.42)

where $\xi = \frac{3}{4}(K_0^{'} - 4)$.

Note that when $K_0^{'} = 4$, the third-order Birch-Murnaghan EoS (BM3) automatically reduces to the second-order one (BM2). In other words, BM2 EoS implicitly assumes $K_0^{'} = 4$. It is remarkable that this estimate of the lowest order of the finite strain theory is often very close to experimental values of $K_0^{'}$ of many crystals (especially with close-packed structures). This is why BM2 EoS, although very simple, works well in many cases. The main problem of all BM EoSs is rather poor convergence with respect to the number of terms beyond the second order for large strains: it turns out that the fourth-order energy term in (1.31) is often larger than the third-order one. The third-order BM EoS is very accurate when $K_0^{'}$ is close to 4; when it is significantly different, this EoS gives poor results at high compressions. For $K_0^{'} < 4$ at large compressions (e.g., for $V/V_0 \cong 0.5$ and $K_0^{'} = 2$) BM3 can give even negative pressures (Poirier and Tarantola, 1998) Being based on a polynomial expansion of the interatomic potential (of the type $\sum\limits_{n=1,2,3...} a_n R^{-2n}$), this EoS must be used with caution when extrapolations are needed – outside the range of fitting the truncated polynomial expansion (1.31) may become invalid (Cohen et al., 2000).

It is possible to derive systematically higher-order BM EoS, but this appears to be of little use since the number of parameters involved will be too large; only fourth order BM EoS:

$$P = 3K_0 f_E (1 + 2f_E)^{5/2} \left\{ 1 + \tfrac{3}{2}(K_0' - 4)f_E + \tfrac{3}{2}\left(K_0 K_0'' + (K_0' - 4)(K_0' - 3) + \tfrac{35}{9}\right)f_E^2 \right\} \quad (1.43)$$

is sometimes used when ultra-high pressures are studied. This EoS is equivalent to the

BM3 EoS when $K_0'' = -1/K_0 \left\{ (3 - K_0')(4 - K_0') + \tfrac{35}{9} \right\}$ – the value implied by the BM3

EoS.

Logarithmic EoSs.

Drawbacks of the Birch-Murnaghan EoSs leave much room for other possible

EoSs. Poirier and Tarantola (1998) have derived the logarithmic EoS, based on the

polynomial expansion (1.31) in terms of natural, or logarithmic (also called Hencky)

strain:

$$f_H = \ln(l / l_0) = \tfrac{1}{3}\ln(V / V_0) , \qquad (1.44)$$

where l is the length of the sample (l_0 in the unstrained sample). The second-order

logarithmic EoS is:

$$P = K_0 (V_0 / V)\ln(V_0 / V) , \qquad (1.45)$$

implicitly assuming $K_0' = 2$. The third-order logarithmic EoS is:

$$P = K_0 (V_0 / V)\left[\ln(V_0 / V) + \tfrac{1}{2}(K_0' - 2)(\ln(V_0 / V))^2 \right] , \qquad (1.46)$$

which implicitly takes $K_0'' = -(1/K_0)\left[1 + (K_0' - 2) + (K_0' - 2)^2 \right]$. In the fourth order, the

logarithmic EoS is:

$$\begin{aligned} P &= K_0 (V_0 / V)\ln(V_0 / V) \times \\ &\times \left[1 + 0.5(K_0' - 2)\ln(V_0 / V) + \tfrac{1}{6}\left\{ 1 + K_0 K_0'' + (K_0' - 2) + (K_0' - 2)^2 \right\}\ln^2(V_0 / V) \right] \end{aligned} \qquad (1.47)$$

Fourth-order logarithmic EoS is superior to BM3, but involves more parameters.

Like the BM3 EoS, the logarithmic EoS has an unphysical behaviour on expansion

($V/V_0 > 1$): the potential corresponding to BM3 behaves nonmonotonically, and the

one corresponding to the logarithmic EoS diverges.

<u>Vinet EoS</u> (Vinet et al., 1986, 1989).

In fact, just like BM and logarithmic EoSs, Vinet EoS is a whole family of EoSs of different orders. The most remarkable feature is very fast convergence with respect to the order of EoS – one seldom needs to use higher than third order Vinet EoS.

The third-order Vinet EoS is:

$$P = 3K_0 \frac{1-(V/V_0)^{\frac{1}{3}}}{(V/V_0)^{\frac{2}{3}}} \exp\left[\frac{3}{2}\left(K_0^{'}-1\right)\left(1-(V/V_0)^{\frac{1}{3}}\right)\right], \qquad (1.48)$$

$$
\begin{aligned}
E(V) = E(V_0) &+ \frac{4K_0 V_0}{\left(K_0^{'}-1\right)^2} - 2V_0 K_0 \left(K_0^{'}-1\right)^{-2} \times \\
&\times \left(5 + 3K_0^{'}\left\{(V_0/V)^{\frac{1}{3}}-1\right\} - 3(V_0/V)^{\frac{1}{3}}\right)\exp\left(-\frac{3}{2}\left(K_0^{'}-1\right)\left\{(V_0/V)^{\frac{1}{3}}-1\right\}\right)
\end{aligned}
\qquad (1.49)
$$

The value of $K_0^{''} = -1/K_0\left[\left(K_0^{'}/2\right)^2 + \left(K_0^{'}/2\right)-19/36\right]$ (Vinet et al., 1989). The bulk modulus can be expressed as (Vinet et al., 1989):

$$
\begin{aligned}
K = &\left(K_0/(V_0/V)^{\frac{2}{3}}\right)\left[2 - (V_0/V)^{\frac{1}{3}} + \left\{(V_0/V)^{\frac{1}{3}} - \frac{3}{2}(V_0/V)^{\frac{2}{3}}\left(K_0^{'}-1\right)\right\}\right]\times \\
&\times \exp\left(\frac{3}{2}\left(K_0^{'}-1\right)\left\{1-(V_0/V)^{\frac{1}{3}}\right\}\right)
\end{aligned}
\qquad (1.50)
$$

This EOS is based on a universal scaled binding curve:

$$E = E_0(1+a)\exp(-a), \qquad (1.51)$$

where E_0 is the bond energy at equilibrium, $a = (R - R_0)/l$, $l = \sqrt{E_0/\left(\frac{\partial^2 E}{\partial R^2}\right)}$ being a scaling length roughly measuring the width of the potential well, and R the Wigner-Seitz radius (the average radius of a sphere in the solid containing 1 atom). The potential (1.48) was first used in 1930s by Rydberg for fitting potential curves of molecules and obtaining their anharmonic coefficients; it turned out (see Sutton, 1993) that it describes very accurately systems with different types of chemical bonding in solids, molecules, adsorbates, etc. The universal binding curve (1.50), however, does not describe long-range forces in ionic and van der Waals crystals.

This means that for such material Vinet EoS will not give accurate description of expansion ($V_0/V<1$). For compression, however, it should be sufficiently accurate, since compression behaviour is dominated by interatomic repulsion, well accounted for by (1.50).

In very rare cases a higher-order Vinet EoS may be needed; such higher-order versions of the Vinet EoS already exist (Vinet et al., 1989). At extreme compressions ($V/V_0 < 0.1$), where solids approach the free electron regime, other EoSs are required (Cohen et al., 2000).

As is shown above, in order to define the equation of state, one should know either free energy as a function of strain (volume), or its derivatives that are pressure and bulk modulus. Free energy cannot be measured directly in experiment, but is the first result of simulation studies. Theoretical studies, including *ab-initio* simulations, usually determine EoS from energy-volume relations. Static compressibility studies allow determining EoS from pressure-volume relation, but require independent pressure calibration. The problem of defining pressure markers and etalon materials EoSs remains quite important for the high-pressure community. Dynamic methods (see section 1.2) allow determining bulk modulus at different pressure. If strain (volume) can be measured simultaneously, EoS can be obtained from bulk modulus-volume relations without any reference to pressure, making possible the primary pressure calibration.

In all the abovementioned EoSs the hydrostatic pressure is used to define the stress tensor, and volume change is the only measure of the strain. The only important elastic constant in this case is the bulk modulus K. This consideration allows making quite simple EoSs with small number of parameters. However, it is true only for isotropic solids under hydrostatic pressure. Birch (1952) demonstrated that such

approach is also valid for crystals with cubic symmetry. In all other cases individual higher order elastic constants are necessary to describe elastic response of the crystal to the finite strain.

For large stresses, the strains are no longer infinitesimal, the stress-strain relation contains terms that are quadratic and higher order in the strains and the strain-energy relationship contains cubic and higher-order terms. The coefficients of these additional terms are the higher-order elastic constants.

Thus, for example, the third-order adiabatic elastic constants can be defined as:

$$c_{ijklmn}^S = \rho \left(\frac{\partial^3 U}{\partial \eta_{ij} \partial \eta_{kl} \partial \eta_{mn}} \right)_S \tag{1.52}$$

and so on (Grimvall, 1999).

Even when higher-order elastic constants can be measured experimentally, the EoS formalism that would incorporate c_{ijklmn} is enormously complicated and thus useless. A large number of experimental studies show that the abovementioned EoS formalism (e.g., Birch-Murnaghan EoS) can be successfully applied to the lower-symmetry crystals. In practice, higher-order elastic constants are quite rarely used; instead, pressure and temperature derivatives of second-order elastic constants are used.

1.1.2 Microscopic approach: Lattice dynamics

At every temperature, at the absolute zero (as a result of zero-point motion) and at finite temperatures (as a result of thermal fluctuations), the atoms in a crystalline solid execute small oscillations about their equilibrium positions. The influence of these lattice vibrations on the thermodynamic properties of solids

together with the masses of the constituent atoms, determine lattice vibrations at a given temperature.

The subject of lattice dynamics is the study of the properties of crystalline solids that are determined or affected by the vibrational motion of the nuclei. The displacement of one or more atoms from their equilibrium positions will give rise to a set of vibration waves propagating through the crystal. In a crystalline solid, the equilibrium atomic configuration can be generated by the repetition of smaller units or cells, the smallest being referred to as the primitive cell. Denoting by $\vec{a_1}$, $\vec{a_2}$ and $\vec{a_3}$, the three vectors along the edges of a primitive cell that share a corner, the equilibrium position of this cell relative to an origin located at some atom is

$$\vec{l} = l_1\vec{a_1} + l_2\vec{a_2} + l_3\vec{a_3} \tag{1.53}$$

where l_1, l_2, and l_3 are integers. The lattice generated by Eq. 1.53 is called the direct lattice of the crystalline solid. The equilibrium position of the dth atom in the lth cell is then

$$\vec{l} + \vec{d}, \tag{1.54}$$

where $\vec{d}$ is the position of the dth atom relative to the corner of the cell as defined by Eq. 1.53.

The basic problem of lattice dynamics is to determine the potential seen by the nuclei of the solid. Once this potential is known, the problem is reduced to the study of the small oscillations of a system of particles around their equilibrium positions in this potential, a well-known problem in mechanics. For a given potential, the motion of the nuclei can be immediately determined assuming that the displacements of the nuclei from their equilibrium positions are small compared to their separation (the quasi-harmonic approximation). This is a very good approximation, except for solids consisting of light nuclei. If the quasi-harmonic approximation is valid, any nuclear

motion can be considered as a superposition of a number of monochromatic waves, the normal vibrational modes or characteristic vibrations of the system. The translational symmetry of crystalline solids simplifies considerably the determination of the frequencies of their normal modes. In this case, the problem is reduced to the determination of the motion of the atoms contained in a unit cell. The normal modes are propagating vibrational waves with propagation wavevector $\vec{q}$ determined by the crystal geometry. If the unit cell contains r nuclei, their frequencies $\omega_j(q)$ are obtained by diagonalizing a $3r \times 3r$ force-constant matrix. The relation

$$\omega = \omega_j\left(\vec{q}\right) \qquad (j = 1,2...3r) \tag{1.55}$$

between the frequency and wavevector is called the *dispersion relation*. It consists of $3r$ branches labelled by the index j. Among these branches there are three acoustic branches whose frequencies approach zero at the long-wavelength limit ($\vec{q} \to 0$) (some branches could be degenerated due to the crystal symmetry). In this limit the dispersion of the acoustic branches is linear, $\omega = \upsilon_j q$ where υ_j is the appropriate sound velocity in the solid, and the propagating vibrational waves in the solid are simply sound waves. The remaining ($3r$-3) branches tend to a finite frequency as $\vec{q} \to 0$, and they are called *optic branches*, since these vibrational modes could interact with light. For each wavevector of a branch, the motion of the nuclei in the cell is determined by solving the equations of motion. The pattern of motion in the cell is specified by the polarization vectors $\vec{e}_d^{\,j}\left(\vec{q}\right)(d = 1,2,...r)$, which provide the direction of motion of the nuclei in the cell. A vibrational mode is called *longitudinal* and *transverse* if the polarization vectors are parallel and perpendicular to the propagation vector, respectively. The allowed values of the propagation vector $\vec{q}$ are determined by the boundary conditions on the surface of the crystal. The bulk

properties of the crystal are not influenced by the specific form of the boundary conditions. For convenience, periodic boundary conditions are usually adopted. Because of the periodicity of the crystal, all physically distinct values of $\vec{q}$ can be obtained by restricting the allowed values of $\vec{q}$ in one of the primitive cells of the reciprocal lattice. Actually, instead of the primitive cell of the reciprocal lattice, it is more convenient to use the first Brillouin zone, which is the volume enclosed by planes that are the perpendicular bisectors of the lines joining a reciprocal lattice point to its neighbouring points. Figure 1.1.2-*a* shows an example of the first Brillouin zone of *fcc*-lattice.

The importance of the Brillouin zone comes from a description of waves in a periodic medium, which can be completely characterized by their behaviour in a single Brillouin zone. There are also second, third, etc., Brillouin zones, corresponding to a sequence of disjoint regions (all with the same volume) at increasing distances from the origin, but these are used more rarely. As a result, the first Brillouin zone is often called simply the Brillouin zone. A related concept is that of the irreducible Brillouin zone, which is the first Brillouin zone reduced by all of the symmetries in the point group of the lattice (Dorner et al., 1987; Alfe et al., 2001).

In the classical description any nuclear motion can be considered as the superposition of propagating waves with various propagation vectors and polarizations. In the harmonic approximation, the motions of the nuclei can be decoupled by a canonical transformation to normal coordinates. By this transformation the nuclear Hamiltonian is reduced to a sum of Hamiltonians corresponding to independent harmonic oscillators, and the quantization of the vibrational field is reduced to that of the harmonic oscillators. Thus, instead of the classical wave description, it turns to the quantum description in terms of quanta,

called *phonons*, which propagate through the lattice with definite energy and momentum. The energy $E_j(\vec{q})$ and momentum $\vec{p}$ of the phonon are related to the frequency and wavevector of the corresponding vibrational wave by the relations:

$$E_j(\vec{q}) = \hbar\omega_j(\vec{q}) \qquad \vec{p} = \hbar\vec{q} \qquad (1.56)$$

The free motion of noninteracting phonons corresponds to the free propagation of the monochromatic waves in the harmonic approximation. The phonons have, however, finite lifetimes, since anharmonic interaction as well as interaction with other elementary excitations in the solid is always present. At thermal equilibrium, brought about by the previously mentioned interactions, the average number of phonons, n_j is given by the Bose-Einstein relation

$$n_j = \frac{1}{\exp(E_j/k_B T) - 1}, \qquad (1.57)$$

where k_B is Boltzmann's constant, and T is the temperature. Notice that at high temperatures ($E_j/k_B T \ll 1$) the number of phonons is proportional to the temperature and inversely proportional to their energy (Maradudin et al., 1963).

Total number of phonons is $3n$, where n is the number of atoms in the irreducible unit cell, and three of them are called acoustic. "Acoustic phonons" have frequencies that become small at the long wavelengths (and tend to zero when wavelength approach infinity), and correspond to sound waves in the lattice. Longitudinal and transverse acoustic phonons are often abbreviated as LA and TA phonons, respectively.

"Optical phonons," which arise in crystals that have more than one atom in the irreducible unit cell, always have some minimum frequency of vibration, even when their wavelength is large. They are called "optical" because in ionic crystals (like sodium chloride) they are excited very easily by light (in fact, infrared radiation). This

is because they correspond to a mode of vibration where positive and negative ions at adjacent lattice sites swing against each other, creating a time-varying electrical dipole moment. Optical phonons that interact in this way with light are called infrared active. Optical phonons, which are Raman active, can also interact indirectly with light, through Raman scattering. Optical phonons are often abbreviated as LO and TO phonons, for the longitudinal and transverse varieties respectively.
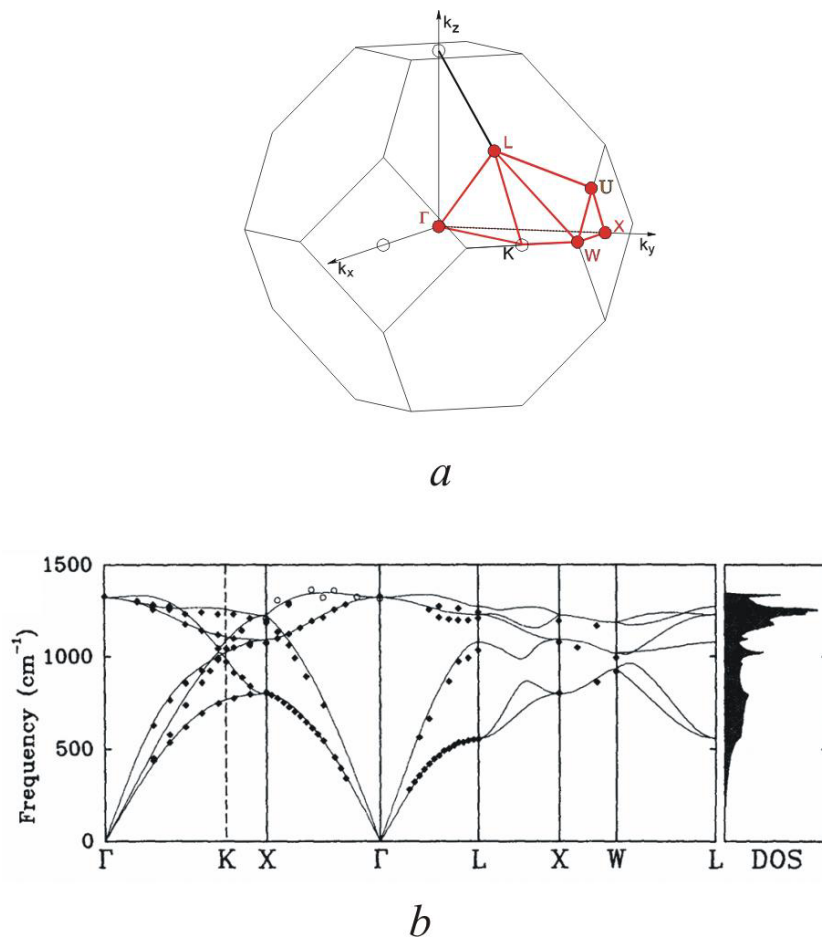

a

b

Fig. 1.1.2. *a*) The Brillouin zone of *fcc*-lattice. The shown critical points of the zone (the points of high symmetry) are: **Γ** - centre of the Brillouin zone, **K** – middle of an edge joining two hexagonal faces, **L** – centre of a hexagonal face, **U** – middle of an edge joining a hexagonal and a square face, **W** – corner point, **X** – centre of a square face; and *b*) an example of phonon dispersion curves and phonon density of states of diamond (Ibach and Lüth, 1996).

Some of the phonon branches could be degenerated due to symmetry elements; for example, along Γ-K direction in diamond all six phonons are different, while only four branches are observed along Γ-X direction due to degeneracy of two TA and two TO phonon branched (see Fig. 1.1.2-*b*).

Information about the phonon dispersion curves of crystalline solids can be obtained by a variety of experimental techniques. The most direct methods involve the scattering (or absorption) of electromagnetic radiation by the solid. In order to obtain elastic constants of solid, only acoustic phonons dispersion branches are necessary.

1.2 Measuring elastic properties

Experimental techniques for determining elastic moduli at high pressures and temperatures are based on the combination of several principles. Pressure apparati that have been modified for such measurements include gas pressure chambers, the piston-cylinder apparatus, multianvil devices, and diamond anvil cells. Measurements of elastic properties in these devices include x-ray diffraction, ultrasonic interferometry, Brillouin scattering, diffraction of light by sound waves, and inelastic x-ray scattering. Each technique offers unique advantages. In some cases, combined techniques provide data that have the potential to become a basis for construction an independent pressure scale.

There are two different ways of measuring elasticity of materials: static and dynamic experiments. Both static and dynamic measurements of elastic moduli at high pressures and temperatures are providing data that are vital to the complete understanding of the elastic properties of materials.

1.2.1 Static measurements

First group of techniques utilize the Hook's law directly and measure elastic response (strain) to the applied stress. Static determinations of elastic properties are among the earliest measurements made with high-pressure devices. *Dilatometry*, one of the most direct methods of measuring compressibility, was pioneered by P.W. Bridgman (1923, 1958). In 1923 he made the most accurate measurements to date on iron and other metals by placing a rod of the metal under hydrostatic pressure in a fluid pressure medium inside a cylinder. He then measured the effect of pressure on the length of the rod by the electrical resistance of a wire attached to the end of the rod. To do this, he had to make a correction for the stretching of the cylinder. The technique is described in details by Bridgman (1958).

In following years, *x-ray diffraction* was substituted for dilatometry for solid samples. Although there had been some earlier measurements, it was not until the 1960s that x-ray techniques for studying samples under pressure were developed to the level that accurate compressibility measurements could be made (Jamieson, 1961; Piermarini and Weir, 1962; Barnet and Hall, 1964; Vereschagin, 1965; Basset et al., 1967). X-ray diffraction provided measurements that depended more directly on the response of the sample and less on the response of the apparatus. Since the 1960s, this method has been an important source of equation-of-state measurements of solid samples at high pressures and temperatures. With few exceptions (Kinsland and Basset, 1976 and 1977; Meade and Jeanloz, 1988), these measurements yielded information only on molar volume and its pressure and temperature derivatives (bulk modulus and thermal expansion).

It has only been within recent years that static measurements have yielded quantitative information about other elastic moduli. Mao with co-authors (1998) and Singh with co-authors (1998) made x-ray diffraction measurements on polycrystalline samples of FeO, α-Fe, and ε-Fe, intentionally subjecting them to nonhydrostatic compression in a diamond anvil cell. Directing an x-ray beam through the sample perpendicular to the load axis yielded diffraction data from which they were able to derive an estimate of the single-crystal elasticity tensor using appropriate equations and incorporating the aggregate shear modulus from independent sources. The major advantage of this technique is that it has yielded quantitative information about the elastic moduli, C_{ij}, to higher pressures than any of the dynamic methods described in following text. It can also be applied as easily to opaque samples as to transparent samples. The result's reported by Mao et al. (1998), and Singh et al. (1998) have very important significance for the understanding of the elastic anisotropy of the solid inner core of the Earth that has been detected by seismologic observations.

The major source of uncertainty in such measurements is unknown degree of stress/strain continuity in the sample. The detailed discussion of this subject together with the full elasticity tensor of pyrite measured up to 45 GPa can be found in the work of Merkel et al. (2002). Elastic constants estimations based on non-hydrostatic powder angle-dispersion diffraction was also performed for Re and Au (Duffy et al., 1999) and FeO (Dubrovinsky et al., 2000a).

1.2.2 Shock waves

Shock wave techniques have been another important source of equation-of-state measurements at high pressures and temperatures (McQueen and Marsch,

1960). Shock wave techniques allow calculating the change of a sample density as pressure and temperature are increased simultaneously along the Hugoniot trajectory in P - T space. Shock wave measurements can yield bulk equation-of-state data to higher pressures than any of the static pressure techniques. However, the derivation of an isothermal or adiabatic equation-of-state from Hugoniot measurements requires making corrections based on the Gruneisen parameter ($\gamma = \alpha K_T / \rho C_V$), where α is a thermal expansivity, K_T is the isothermal bulk modulus, ρ is density, and C_V is constant volume heat capacity. A discussion of the shock wave method and a comparison with other methods for making equation-of-state measurements are given by Duffy and Wang (1998). Shock wave methods in some sense are in between static and dynamic measurements: quite large stresses are applied to the sample (similarly to static methods) but for a quite short time (similarly to dynamic methods). Shock wave compression could provide only the value of bulk modulus. Pressure and temperature cannot be varied independently and only the Hugoniot path in P, T space is possible, and only small variations are possible by varying initial sample density or temperature.

1.2.3 Dynamic measurements

Elasticity measurements at high pressures and temperatures based on dynamic techniques have relied on four basic techniques: (1) ultrasonic interferometry (Anderson, 1961), (2) Doppler shifted Brillouin scattering by thermal phonons (Basset and Brody, 1977), (3) diffraction of laser light by induced sound waves (impulsive stimulated scattering, ISS) (Nelson et al., 1982; Brown et al., 1989), and (4) inelastic x-ray (IXS) and neutron (INS) scattering (Dorner et al., 1986 and 1987; Burkel,

2000). The first requires the use of ultrasonic signals as the probe. Methods 2 and 3 utilize laser light and its interaction with phonons as the means to probe sound wave velocities. Recently, an inelastic x-ray scattering technique that could determine acoustic phonons dispersion curves have also been applied with a large success in a high-pressure diamond anvil cell experiments (Krisch et al., 1997).

Ultrasonic interferometry in different pressure devices

Ultrasonic measurements of elastic constants are based on the solution of Cristoffel equations (Brugger, 1965). The propagation of ultrasonic waves through a solid medium can be considered as an alteration of local compression, expansion and shear deformation of relatively small magnitude. The propagation speed is, therefore, related to elastic properties of a medium. General relation is

$$\rho v^2 = C, \qquad (1.58)$$

where ρ is density, v is the speed of wave propagation, and C is effective elastic constant. The latter is a combination of individual elastic constants C_{ij} that depends on propagation and polarization vectors. Solutions of Cristoffel equations for different crystal symmetries can be found in (Brugger, 1965).

The earliest ultrasonic measurements of elastic moduli on samples as a function of pressure and temperature were performed using gas as the pressure medium. Anderson (1961) describes a typical apparatus (Fig. 1.2.1) based on techniques developed by McSkimin (1961).
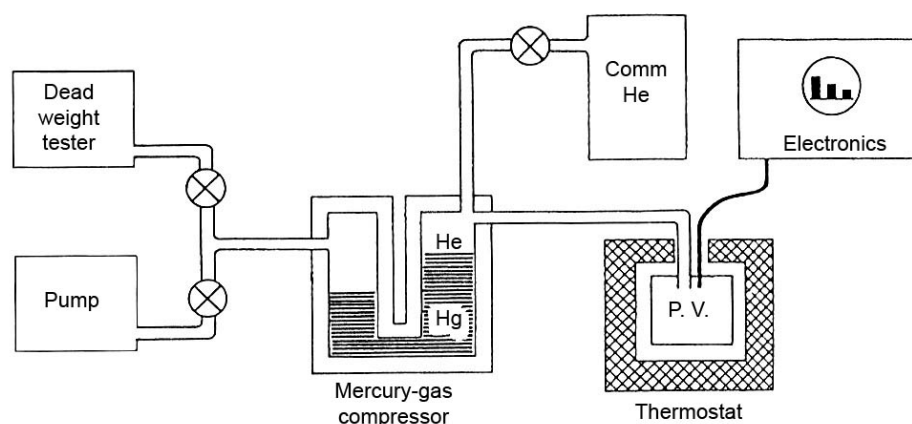
Fig. 1.2.1. Apparatus for obtaining isobaric measurements of sound velocity (after Anderson, 1961).

In this apparatus the sample was surrounded by a gas, usually helium or nitrogen that was held at a very constant and accurately determined pressure by utilizing the dead weight principle. This consisted of a piston with a well-defined surface area loaded with accurate weights. The piston pressed on oil, which also served as its lubricant. The oil was separated from the gas medium by a mercury manometer that had a minimal effect on the pressure measurement. This apparatus was capable of pressures up to 0.5 GPa and temperatures from 2 to 500 K. Pressures could be measured with an accuracy of 3 parts in 10 000. Temperature was measured by a copper-constantan thermocouple to within 1/2 K. The sample chamber could be cooled by immersion in liquid nitrogen or helium.

The ultrasonic measurements were made using pulse superposition interferometry developed by McSkimin (1961). The quartz transducer was sealed to the sample. Frequencies of the order of 10 MHz were used, and the pulses had a width of 2-100 msec with a repetition rate of about a millisecond. Measurements of elastic moduli could be made with an accuracy of about 1 part in 1 000.

Chen with co-authors (1996) used a gas pressure vessel with argon gas as the pressure medium. An internal transducer on the end of a buffer rod delivered acoustic signals to the sample, which was surrounded by a heater. The major innovation was the use of gigahertz frequencies with significantly shorter wavelengths. The shorter wavelengths allowed much smaller samples, thus making it possible to have greater perfection and to study materials for which large crystals are rare.

The *piston-cylinder apparatus* for ultrasonic measurements was developed to reach higher pressures than the gas systems could supply. In piston-cylinder devices the transducer (or transducers) is placed in contact with the sample inside the pressure chamber (Jackson and Niesler, 1982), or the signal is introduced by means of a buffer rod built into the pressure vessel that carries the signal from outside the pressure vessel to the sample inside (Niesler and Jackson, 1989; Heydemann and Houck, 1971).

An example of internal transducers is shown in Figure 1.2.2. In this device a single crystal is subjected to hydrostatic pressures of up to 3 GPa in a fluid medium such as a mixture of pentane and isopentane.

A transducer such as quartz or lithium niobate is bonded to the top of the sample. An additional transducer can also be bonded to the bottom of the sample. Pressure is measured by means of the resistance in a coil of manganin wire surrounded by the fluid. Ultrasonic signals in the range of 10-105 MHz are introduced into the crystal by the upper transducer and are detected either by reflection from the far side of the sample or by a second transducer attached to the bottom of the sample. Interference of acoustic waves by pulse superposition is used to determine travel times. They can be used to calculate velocities and elastic moduli when the dimensions and density of the sample as a function of pressure are known. These can

be derived from an equation-of-state for the sample based on the ultrasonic measurements themselves (with independent pressure determination) or any other source of equation-of-state data for the sample.

The *multianvil high-pressure apparati* can also be used and modifications were made to adapt these high-pressure devices for measurements of elastic properties at pressure using ultrasonic interferometry (Kinoshita et al., 1979; Fukizawa and Kinoshita, 1982; Sasakura et al., 1989 and 1990; Yoneda, 1990; Yoneda and Morioka, 1992; Fujisawa, 1998). Both single-crystal and polycrystalline samples were studied by this method. An example for such setup for ultrasonic measurements at simultaneous high pressures and temperatures in a multianvil apparatus is the one pursued at the Mineral Physics Laboratories of State University of New York (SUNY), Stony Brook (Liebermann and Li, 1998; Liebermann et al., 1998).

At SUNY Stony Brook a 1000-ton uniaxial split-cylinder apparatus (USCA-1000) has been adapted for ultrasonic interferometry measurements at high pressures (Li et al., 1996b). This apparatus consists of eight cubes, each with a truncated corner that presses against a sample having the shape of an octahedron. Pressure is applied to the sample by driving the eight cubes inward against the octahedral sample. The adaptation for ultrasonic measurements consists of truncating diagonally opposite corners of one of the cubes and attaching a lithium niobate transducer to the truncation opposite from the corner that bears on the sample (Fig. 1.2.3).
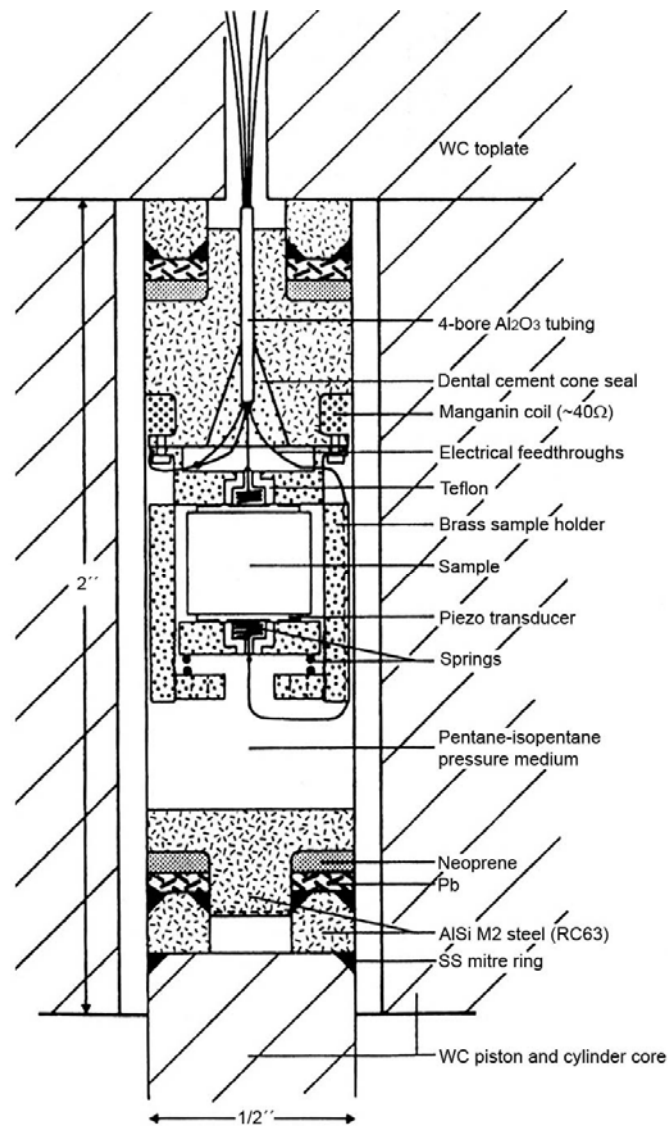
Fig. 1.2.2. The piston-cylinder apparatus used by Jackson and Niesler (1982) for making ultrasonic velocity measurements on a sample at hydrostatic pressures up to 3 GPa. In this configuration the piezoelectric transducers are inside the pressure chamber.

The location of the transducer in the gap between the first-stage anvils and the second-stage cubes does not allow it to experience stress, and the transducer is capable of accurate travel-time measurements in the frequency range of 20-70 MHz. The cube, thus modified, serves as the "buffer rod" to transmit acoustic signals from

40

the transducer to the sample and back. Lead surrounding the sample where it is not in contact with the "buffer rod" serves as a pressure medium. A Teflon disk attached to the sample opposite the "buffer rod" provides an impedance mismatch for reflecting the signal back through the sample.

Runs at different pressures and temperatures can be made on the same sample, and repeat runs can be made with only minor repolishing of the contact face.
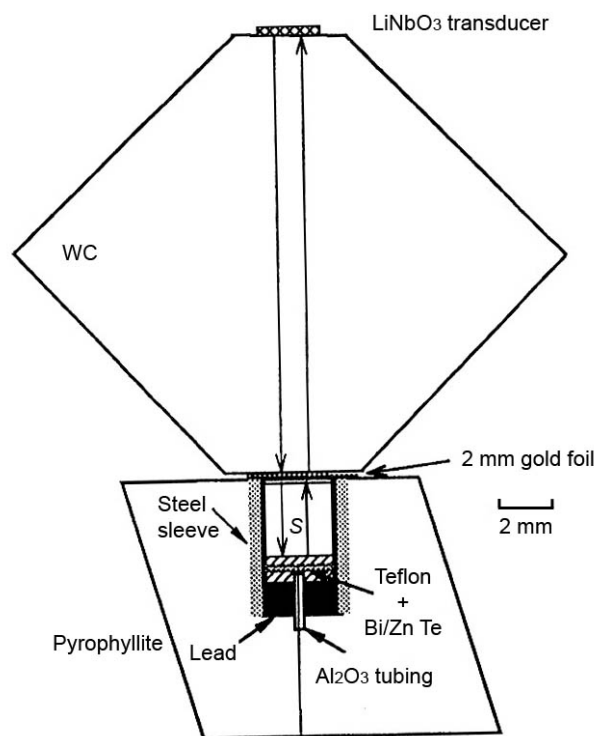
Fig. 1.2.3. A cross-section of one of the eight cubic tungsten carbide anvils (after Li et al., 1998b). The cube anvil, which has flats on opposite corners, serves as a buffer rod to carry the acoustic signal from the external transducer to the sample under the pressure.

Although polycrystalline samples provide valuable information about the elastic properties of samples in a high-pressure device, the complete set of elastic moduli can be obtained only by making measurements on oriented single-crystal samples. The

SUNY Stony Brook group has adapted the DIA-type, cubic-anvil apparatus (SAM 85) for single-crystal measurements (Li et al., 1998a). The sample is centred in the cubic cell assembly and is surrounded by a boron nitride sleeve. The acoustic signal is transmitted from the anvil face to the single-crystal sample by an alumina or fused silica buffer rod. The far end of the sample is pressed against a NaCl disk. A combination of P and S waves with various orientations of the crystal can supply all values of C_{ij}.

Both types of multianvil high-pressure devices just described can be used to subject samples to simultaneous high pressures and high temperatures. Immediately surrounding the sample is a graphite furnace. A thermocouple is used to measure the temperature, and an alumina buffer rod is employed. The NaCl disc in contact with the sample not only serves to make the pressure environment more hydrostatic but also provides a pressure calibrant.

It is now feasible to measure elastic properties by ultrasonic interferometry in samples small enough to be subjected to high pressures and temperatures in a *diamond anvil cell*, thanks to advances in the generation, transmission, and analysis of coherent gigahertz ultrasonic signals (Reichmann et al., 1998; Spetzler et al., 1996; Shen et al., 1998; Basset et al., 2000). At these frequencies, acoustic signals have wavelengths of the order of micrometers, suitable for use with samples that are typically 50-100 microns thick. The ultrasonic signal generated by a thin transducer is transmitted along a sapphire buffer rod coupled by force to one of the diamond anvils. The signal traverses the diamond anvil and enters the single-crystal sample, which is coupled to the anvil face by cement, by adhesion, or by a normal force. Interference of superimposed waves reflected from the near and far faces of the single crystal is used to measure the travel time of the sound waves in the sample.

Figure 1.2.4 shows the diamond anvil cell adapted for gigahertz ultrasonic velocity measurements. The acoustic signal travels along the sapphire buffer rod and through one of the diamond anvils to the sample, which is under hydrostatic pressure inside a gasket between the diamond anvils.
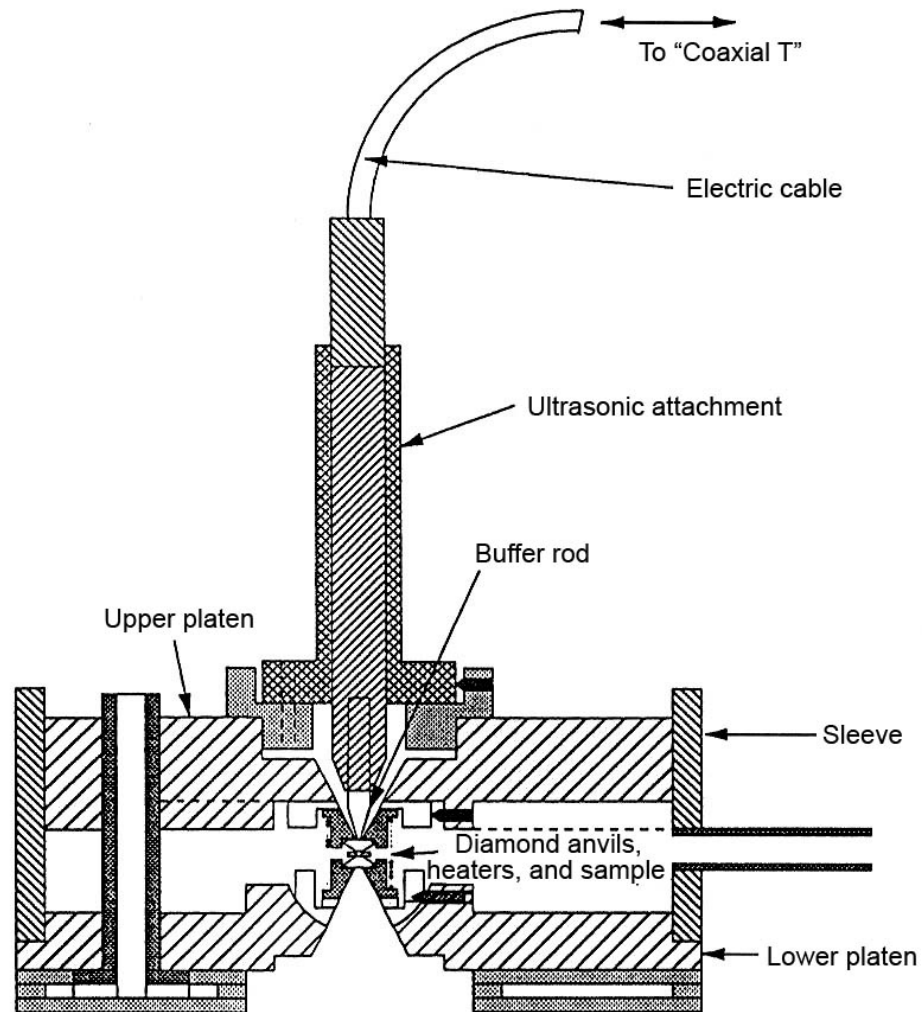

Fig. 1.2.4. Diagram of a diamond anvil cell adapted for gigahertz ultrasonic velocity measurements on very small samples (after Shen et al., 1998).

Brillouin scattering

Brillouin considered (Brillouin, 1921) that the periodic perturbations that a sound wave generates in a medium could scatter a beam of light. Furthermore, because these "gratings" in the medium propagate with the velocity of sound, he predicted that the resulting Doppler effect would lead to a change in the frequency of the light.

From the point of view of lattice dynamics, Brillouin scattering probes the acoustic phonon dispersion branches in the vicinity of the Γ point (see section 1.1.2). A typical radius of the first Brillouin zone is of the order of 10^1 nm^{-1}, while laser light wavelength used to excite thermal phonons corresponds to the wavevector of the order of 10^{-2} - 10^{-3} nm^{-1}. Acoustic phonon dispersion curves are linear in this range, and corresponding sound speed can be directly calculated with very high accuracy and precision (Dorner et al., 1987).

The technique takes advantage of existing thermal phonons in the sample and requires only that a beam of monochromatic laser light enters and exits the high-pressure zone. The transparent diamond anvils of a diamond anvil cell offer this capability. In this method, monochromatic light from a laser passes through one of the diamond anvils, is Bragg-reflected from thermal phonons in the single-crystal sample, and then passes out through the other diamond anvil at 90 degrees to the entering beam. The Brillouin scattered light enters a Fabry-Perot spectrometer, where it is frequency analyzed. The scattered light in such an experiment is Doppler-shifted by the velocities of the phonons that are oriented to Bragg-reflect the light. The spectrum recorded by the Fabry-Perot spectrometer has peaks with both greater and lesser

frequencies due to phonons travelling in opposite directions. The amount of shift of these peaks can be used to determine the phonon velocities (Basset and Brody, 1977).

Hydrostatic pressure is essential for accurate measurements of elastic moduli. Therefore, the single-crystal sample must be surrounded with a fluid contained inside of a gasket between the diamond anvil faces (Fig. 1.2.5).
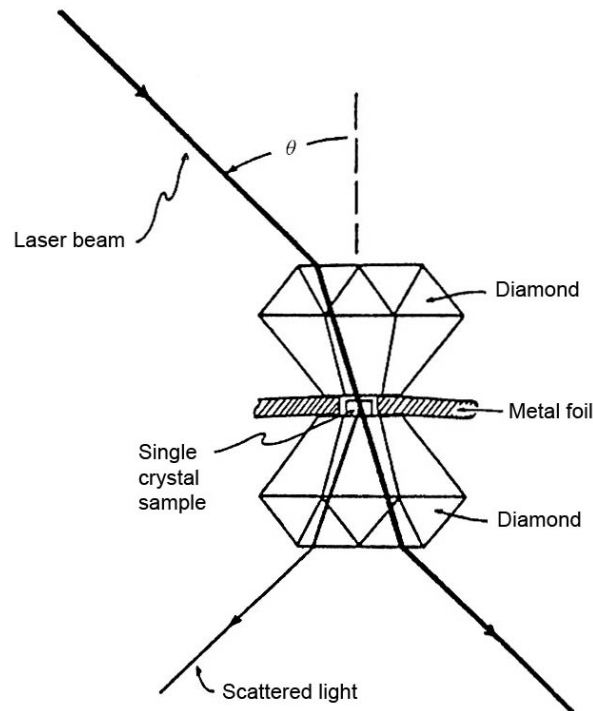

Fig. 1.2.5. Details of the light path trough the diamond anvils and sample (Basset and Brody, 1977).

The fluid most suitable for achieving hydrostatic pressure up to approximately 10 GPa is a mixture of methanol, ethanol and water in a ratio of 16:3:1. There are, in addition, some experimental conditions that greatly simplify the interpretation of the Brillouin scattering measurements. If all of the interfaces through which the light passes are strictly parallel and bisect the angle between the incident and scattered rays, then no correction needs to be made for the refractive indices of any of the materials through which the light passes. When the equations for Doppler shift and for

Snell's law are combined for experimental conditions in which the incident and scattered angle is 45°, then the relationship can be expressed by the equation

$$\upsilon = \left(\Delta \omega \lambda_0 \right)/\sqrt{2} \ , \qquad\qquad (1.59)$$

where υ is the velocity of the phonon, $\Delta\omega$ is the measured frequency shift, and λ_0 is the wavelength of the impinging light. Similarly, a derivation can be carried out in terms of conservation of momentum and energy in the interaction of the quanta of light and sound. The final relationship is the same (Basset and Brody, 1977).

The technique almost exclusively limited to transparent samples but recently developed extensions of Brillouin light scattering experiments to the surface Brillouin scattering allows measuring also opaque samples (Crowhurst et al., 1999). Crowhurst and co-authors used a cell with cubic zirconia anvils. In their cell the sample in the form of a thin film was squeezed between glass surface and silicone oil. A laser beam passing through the glass was reflected off the surface of the sample while it was under pressure. As in the more standard technique employed with transparent samples, the frequency shift due to scattering from surface phonons can be used to calculate velocities as a function of pressure. Their successful measurement of the change of C_{44} of gold as a function of pressure using this technique demonstrates its promise for studying other opaque samples under pressure by Brillouin scattering (Crowhurst et al., 1999).

Impulsive stimulated scattering in the diamond anvil cell

As in the Brillouin scattering technique, laser light scattered by sound waves in a single-crystal sample can be used to calculate elastic moduli. Unlike Brillouin scattering, however, the sound waves in the impulsive stimulated scattering (ISS)

method are stimulated in the sample by means of laser radiation (Yan et al., 1998; Fayer, 1986; Nelson et al., 1982; Miller et al., 1984). Brown and his colleagues have adapted the ISS method, also known as laser-induced phonon spectroscopy, for application with single-crystal samples under hydrostatic pressure in a diamond anvil cell (Brown et al., 1989; Zaug et al., 1992).

The ISS method requires two forms of laser radiation, one to stimulate the sound waves, and the other to probe the velocity of the sound waves (Fig. 1.8, *a*). Two successive pulses are selected from a train of pulses (or are split by mirrors from a single pulse) produced by a Q-switched, mode-locked Nd:YAG laser ($\lambda = 1064$ nm). Another pulse is selected and passed through a frequency-doubling crystal to provide green light ($\lambda = 532$ nm) to serve as the probe. The pulses of 1064-nm radiation simultaneously enter the sample with an angle, 2θ, separating them. Inside the sample, the pulses are combined so that their interference pattern produces a spatially periodic distribution of pressure and temperature (Fig. 1.8, *b*), which in turn launches acoustic waves that proceed to travel in opposite directions simultaneously. The highest frequency could be excite is limited only by the laser pulse width. There was no sample heating due to the excitation and probe pulses found to be a significant factor in the measurements (Crowhurst et al., 2004).

Variation in the refractive index from crest to trough along each of these sound waves acts like a picket fence. As the two "picket fences" travel past each other in opposite directions, they cause the amount of 532-nm probe light that is Bragg-reflected off the sound waves to fluctuate. This fluctuation is detected by means of a controlled increase in the delay between the stimulating pulses and the probing pulse using a variable time-of-flight device (Fig. 1.2.6, *a*). The wavelength of the sound

waves λ_A depends on the wavelength of the stimulating radiation, λ_L, and the angle, 2θ, between the stimulating laser beams.

$$\lambda_A = \lambda_L / 2\sin\theta \ , \tag{1.60}$$

The fluctuation in the intensity of the probe light yields the frequency, f_A, of the acoustic waves. The velocity, V_A, of the acoustic waves can be calculated from the equation

$$V_A = \lambda_A f_A \ , \tag{1.61}$$

In an anisotropic crystal, the thermal pressure of stimulating radiation launches three counter propagating acoustic waves, one - quasi-longitudinal and two - quasi-transverse. Rotation of the diamond anvil cell around an axis perpendicular to the diamond anvil faces permits the measurement of velocities in all directions perpendicular to that axis.

Resonant ultrasonic spectroscopy under gas pressure

In resonant ultrasonic spectroscopy (RUS) normal mode frequencies in a sample (having the shape of a parallelepiped or sphere) are used to determine the elastic properties of the sample. Several years ago the method has been adapted for making measurements on samples under pressure (Isaak et al.,1998; Ohno et al., 2000). In both of these studies the technique was applied to the measurement of elastic properties of a silica glass sphere in a pressure vessel in which the pressure medium was helium gas. Two transducers were in contact with the sample sphere. One was used to excite the normal mode frequencies, and the other detected the response.
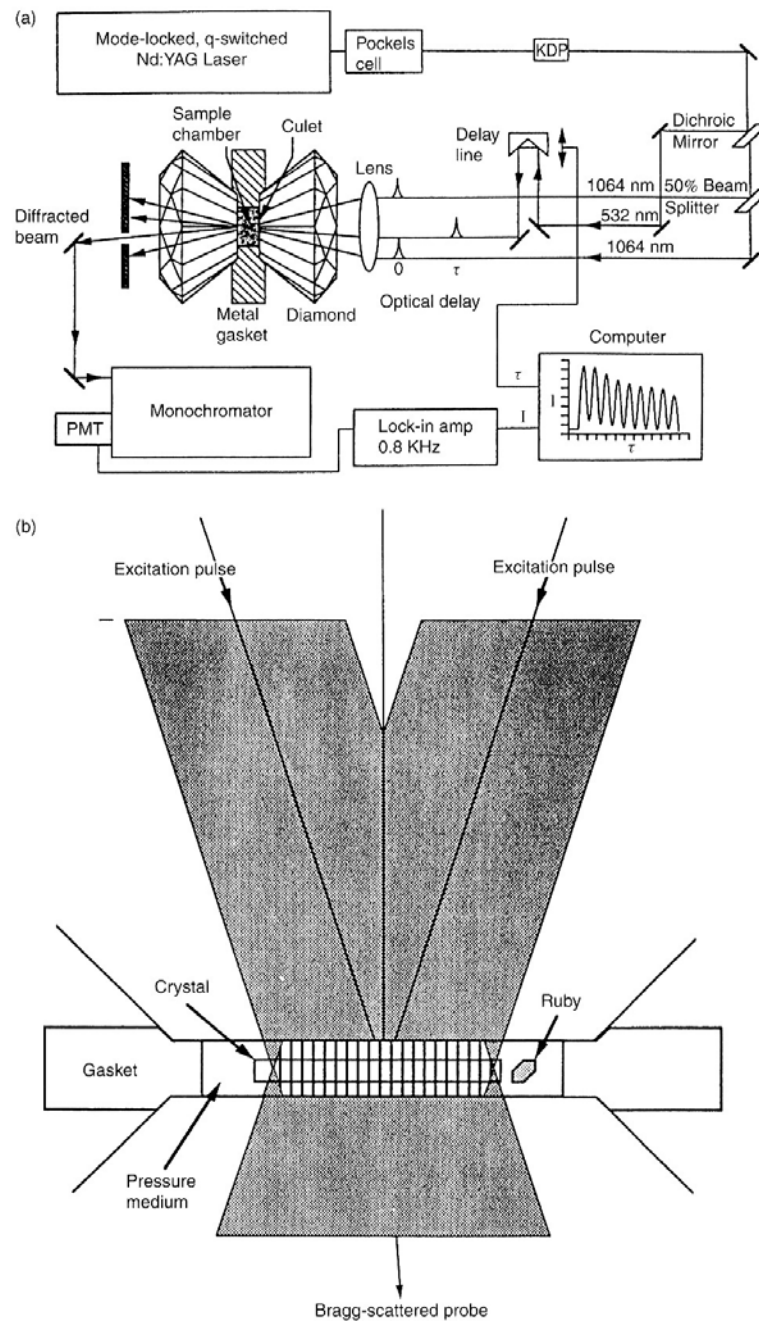
Fig. 1.2.6. (a) Schematic diagram of the apparatus used to make ISS measurements of phonon velocities in a sample under hydrostatic pressure inside a diamond anvil cell, from Baer et al. (1998). The top and bottom laser beams interfere to create a diffraction grating inside the sample. The middle beam of light is diffracted of the grating. Intensity as a function of delay between the exciting and the analyzing pulses is used to calculate the velocity. (b) Details of the diffraction grating created in the sample by interfering excitation pulses (after Zaug et al., 1992).

Information about the phonon dispersion curves of crystalline solids can be obtained by a variety of experimental techniques. The most direct methods involve the scattering (or absorption) of radiation by the solid.

Inelastic neutron scattering (INS)

By far, most of the information available on the dispersion curves of solids has been obtained using the more powerful neutron-scattering techniques. The reason for the central role played by this technique in the development of the field of lattice dynamics is that the energy and wavevector of the neutrons available in a neutron source are of the same order as those of the normal vibrations in a solid (for a typical normal mode in a solid, $\nu = \omega / 2\pi \approx 10^{12}$ Hz = 1 THz $\approx$ 4 meV $\approx$ 50 K, and $q \approx 10^8$ cm^{-1} = 1 Å^{-1}).

The phonon dispersion curves can be obtained directly by studying the one-phonon coherent scattering of a monochromatic beam of neutrons (of wavevector $\vec{k}_0$ and energy $E_0 = \hbar^2 k_0^2 / 2m$) from a single crystal. In these studies, one simply measures the momentum and energy transfer involved in the coherent scattering of an incident neutron with wavevector $\vec{k}_0$ to a final state with wavevector $\vec{k}_1$ due to the creation of a single phonon of frequency $\omega_j(\vec{q})$.

Inelastic neutron scattering technique is one of the most powerful tools for the study of the lattice dynamics of solids. However, for the measurements only relatively big samples (at least 1 mm^3) are necessary, consequently the maximum pressure is limited to about 15 GPa. Until recently, inelastic neutron scattering was used to determine the elastic constants in cases for which one could not use more

conventional techniques: crystals that are difficult to handle, such as barium, and materials that are available only in polycrystalline form. Nevertheless, today the technique finds its most important application in the study of the elastic constants, of the high-temperature and high-pressure phases of various solids. Finally, the technique is unique for the study of magnetoelastic effects in solids (Klotz and Braden, 2000).

Inelastic x-ray scattering (IXS)

IXS complements the well-established inelastic neutron scattering (INS) spectroscopic methods in cases where neutron techniques are difficult to apply. This concerns the study of collective excitations in disordered systems, where well defined excitations typically exist only up to momentum transfers of a few nm^{-1}. In particular for disordered systems with a high speed of sound (>2000 m/s), the low energy (E) and momentum transfer (Q) region is difficult, or even impossible, to access by neutron scattering owing to kinematic limitations. Furthermore, the small source size and beam divergence of modern synchrotron sources opens up the possibility of studying materials available only in small quantities down to 10^{-5} mm^3. This is of particular interest for the study of matter under high pressure, since it allows one to employ diamond anvil cell techniques, and therefore access pressure regimes up to 100 GPa and beyond.

Some specific features of inelastic x-ray scattering, as compared to the Brillouin scattering of light, arise from the fact that the wavelength, λ of x-rays is four orders of magnitude shorter than that of the visible light photons. The most important difference, in comparison with the phonon-induced scattering of light and thermal

neutrons, is the extremely small energy transfer, ΔE, with respect to the x-ray energy, $E \approx 10^4$ eV. Even for acoustic phonons with wavevectors at the Brillouin zone boundary, which have an energy of $\hbar\omega \approx 0.02$ eV, the ratio $\Delta E/E = \hbar\omega/E$ is only 2 · 10^{-6}. For 300 MHz phonons, which have energy of $\hbar\omega \approx 10^{-6}$ eV, the ratio $\hbar\omega/E = 10^{-10}$ is practically zero.

IXS cross-section and kinematics will be described in the next Chapter. For geophysics, the high frequencies (in order of THz) used in IXS experiments have the interest of getting close to the infinite frequency limit, comparatively to the low frequency limit provided by radial x-ray diffraction modelling.

The overview and comparison of discussed above techniques is presented in table 1-2.

Table 1-2. Comparison of various methods for elasticity measurements.

Experimental method	Sample type	Sample size (minimal)	Sample requirements	Obtained elastic constants	P and T limits	Specific limitations*	Measuring frequency	Examples†
XRD upon static compression in a DAC	single crystal	10x10x10μm³	none	bulk modulus and linear compressibility	~50 GPa / ~4000 °C		<10⁻² Hz	[1]
	powder	10x10x10μm³	fine-grained powder	individual C_{ij} (Singh et al., 1998)	~300 GPa	knowledge of stress-strain conditions in the sample are necessary	<10⁻² Hz	[2]
XRD upon static compression in a large-volume press	powder	1x1x1mm³	none	bulk modulus and linear compressibility	25 GPa / 2500 °C	synchrotron-based method	<10⁻² Hz	[3]
Shock-wave compression	powder	1x1x1 mm³	none	bulk modulus	600 GPa / ~5000 °C	only Hugoniot P,T path is possible	~10³ Hz	[4]
Ultrasonic measurements in a DAC	single crystal	50x50x20 μm³ (depends on sound velocities in the sample)	optical parallel polishing; high crystal quality	individual C_{ij}	~50 GPa	extreme sensitivity to the sample quality; knowledge of density and sample thickness is necessary	~10⁹ Hz	[5]
	liquids		none	bulk modulus	~1000 °C (resistive heating)	thickness and density should be measured independently		
	nanocrystalline materials	0.1x0.1x0.1 mm³	crystallites size < 40 nm	bulk and shear moduli				
Ultrasonic measurements in a large-volume press	single crystal	1x2x2 mm³	high crystal quality	individual C_{ij}	~5 GPa / ~1200 °C	thickness and density should be measured independently	~10⁶ Hz	[6]
	powder	1x1x1 mm³	no texture	bulk and shear moduli	25 GPa / 2500 °C			

Table 1-2 (continuation). Comparison of various methods for elasticity measurements.

Experimental method	Sample type	Sample size (minimal)	Sample requirements	Obtained elastic constants	P and T limits	Specific limitations	Measuring frequency	Examples
Brillouin scattering in a DAC	single crystal	20x20x20 μm³	optical polishing	individual C_{ij}	~50 GPa ~4000 °C (laser heating, never applied so far)	only transparent samples; density should be measured independently	~10^{15} Hz	[7]
	powder		no texture	bulk and shear moduli	~300 GPa (was not applied so far)			
Impulsive-stimulated scattering in a DAC	single crystals	20x20x20 μm³	optical polishing	individual C_{ij}	~50 GPa ~4000 °C (laser heating, never applied so far)	only transparent samples; in transmission geometry elastic properties of pressure medium are required for reflection geometry	~10^{9} Hz	[8]
	liquid	0.1x0.1x0.1 mm³	none	bulk modulus	~300 GPa (was not applied so far)			
Inelastic X-ray scattering in a DAC	single crystal	20x20x20 μm³	none	individual C_{ij}	~50 GPa		~10^{4} - 10^{9}	[9]
	powder		no texture	bulk and shear moduli	~300 GPa (was not applied so far) ~1000 °C (resistive heating)			
	liquid		none	bulk modulus	~50 GPa			
Inelastic neutron scattering	single crystal or powder	80x80x80 μm³	none	individual C_{ij}	~50 GPa ~1000 °C (resistive heating)		~10^{6} - 10^{15}	[10]

* There are some common limitations for different groups of techniques. All single-crystal methods require preservation of single crystal during experiment. All inelastic scattering methods have additional limitations for sound velocities or phonons of the sample should not overlap with those of diamond anvil (usually higher than sample) and those of pressure transmitting medium (usually lower than sample).

† Example's references are listed below.

Some examples for measured elastic properties of Earth's materials by mean of various techniques (see table 1-2):

[1] Single crystal of FeO and (Mg,Fe)O to 51 GPa (Jacobsen et al., 2005b)

[2] Iron to 300 GPa and 1350 K (Dubrovinsky et al., 2000b)

[3] Polycrystalline specimens of two polymorphs of Mg_2SiO_4: forsterite and wadsleyite (Li te al., 2004); ferropericlase to 9 GPa (Kung et al., 2002)

[4] Iron (Brown and McQueen, 1986); forsterite to 150 GPa (Duffy and Ahrens, 1995a); periclase to 27 GPa (Duffy and Ahrens, 1992); forsterite to 150 GPa (Duffy and Ahrens, 1992); periclase to 27 GPa (Duffy and Ahrens, molybdenum to 81 GPa (Duffy and Ahrens, 1994)

[5] Single crystal of (Mg,Fe)O to 10 GPa (Jacobsen et al., 2002a); natural single crystals of pyrope and almandine at ambient conditions (Chen et al., 1997); single crystal of FeO to 10 GPa (Kantor et al., 2004a)

[6] San Carlos olivine up to 3 GPa (Mueller et al., 2002); single crystal periclase and forsterite to 1800K (Isaak et al., 1989a, b); polycrystalline olivine to 10 GPa and 1300K (Li et al., 1998b); wadsleyite to 7GPa and 873K (Li et al., 2001); $MgSiO_3$ perovskite to 8GPa and 800K (Sinelnikov et al., 1998)

[7] Natural samples of olivine, orthopyroxene and garnet to 20 GPa (Brown et al., 1989: Zaug et al., 1993: Chai et al., 1997a,b; Abramson et al., 1999); natural majorite-pyrope solid solution under pressure (Sinogeikin and Bass, 2002)

[8] Single crystal of low albite $NaAlSi_3O_8$ (Brown et al., 2006); single-crystal of San Carlos peridotite (Brown et al., 1989)

[9] Polycrystalline iron to 110 GPa (Fique et al., 2001)

[10] Single crystals of FeO, bcc-Fe and some other materials to 12 GPa (Klotz, 2001); powder of FeO to 48 GPa (Struzhkin et al., 2001); magnetite to 5.3 GPa (Klotz et al., 2006)

1.3 Geophysical implications

Understanding the mineral composition of Earth's interior is a major challenge in geophysical studies. The direct sampling is limited to rocks formed maximum in the first few hundred kilometers of depth (Anderson, 2007). Investigations of the elastic state of the Earth, however, are a powerful tool for determining the mineral composition of Earth's interior. Profiles of compressional and shear wave velocities V_P and V_S in the Earth are calculated from seismic studies. These profiles, when compared with the elastic properties of minerals measured at high pressures and temperatures in laboratory studies, are the primary means by which one can constrain plausible compositional models of Earth's interior. Although most of the laboratory measurements are carried out at the conditions far from those in the Earth's deep interior, the frequencies of waves generating in laboratories are usually far from those of seismic waves, the measurements themselves, being only the first step in interpreting seismic velocities, are rather important, since no "long way" is possible without a first step.

1.3.1 Wave velocities and proper thermodynamic interpretations

The primary geophysical data are the longitudinal and shear wave velocities. They are related to the isotropic bulk and shear moduli, K_S and G, and density, ρ, as

$$V_P = \left[\frac{K_S + \frac{4}{3}G}{\rho} \right]^{\frac{1}{2}} ,$$
(1.62)

and

56

$$V_S = \left[\frac{G}{\rho} \right]^{\frac{1}{2}},$$
(1.63)

The K_S modulus in Eq. 1.62 is the adiabatic bulk modulus and is defined by

$$K_S = -V \left(\frac{\partial P}{\partial V} \right)_S = \rho \left(\frac{\partial P}{\partial \rho} \right)_S,$$
(1.64)

where P is pressure, V is volume, and S is entropy. The isothermal bulk modulus, K_T, where T is temperature, is given as

$$K_T = -V \left(\frac{\partial P}{\partial V} \right)_T = \rho \left(\frac{\partial P}{\partial \rho} \right)_T,$$
(1.65)

and generally applies to the bulk modulus when used in equation-of-state formulations. Dynamical experiments such as resonance ultrasound, plane-wave propagation, and Brillouin scattering necessarily obtain data leading to K_S. Static pressure-strain experiments (for example, diamond anvil cells or large-volume presses experiments) obtain data relevant to K_T. The relation between K_S and K_T is as follows:

$$K_S = K_T \left(1 + \frac{\alpha^2 V K_T}{C_V} T \right),$$
(1.66)

where α is the volume coefficient of thermal expansion, C_V is the specific heat capacity at constant volume, and temperature (T) is in Kelvin. While

$$\frac{C_P}{C_V} = \frac{K_S}{K_T},$$
(1.67)

where C_P is the specific heat capacity at constant pressure, the Eq. 1.66 could be written as K_S

$$K_T = \frac{K_S}{1 + \frac{\alpha^2 V K_S}{C_P} T},$$
(1.68)

or, alternatively,

$$K_S = K_T \left(1 + \alpha\gamma T\right),$$ (1.69)

where γ is the Grüneisen parameter.

Equations 1.66 and 1.68 show that $K_S = K_T$ at $T = 0$, but $K_S > K_T$ for $T > 0$. The difference between K_S and K_T at room temperature is small, being about 1-2 % for most minerals, because α is small. The difference between K_S and K_T increases, however, with increasing temperature (Isaak, 2001).

There is no need to distinguish between isothermal and adiabatic values of the shear modulus. The difference between adiabatic and isothermal quantities arises from adiabatic heating or cooling with volume changes. The shear modulus, however, relates shear stresses to volume-conserving shear strains.

1.3.2 Importance of single-crystal elasticity data in geophysical studies

When polycrystalline material studied, the irregular effects of the specimen (such as porosity, texturing, and grain boundaries) usually influence the results of measurements. These effects could be eliminated when hot-pressed polycrystalline aggregates are probed. Such studies have been successfully accomplished and have provided crucial data on the elasticity of high-pressure mineral phases relevant to Earth's mantle (Liebermann and Li, 1998; Gwanmesia et al., 1990a; Gwanmesia and Liebermann, 1992). Performing measurements on high-quality single-crystal specimens is even better, since there is no porosity, texturing, or grain boundaries. However, this is not the major importance of single-crystal studies in geophysics.

Geophysical records of the last decade resolved some local seismic anisotropy in the Earth's interior. For many regions in the Earth such anisotropy is believed to be a

reflection of non-isotropic orientation of rock-forming crystallites. In order to reconstruct the model for texturing in anisotropic regions, a solid knowledge of individual elastic constants for the corresponding phases is necessary. Individual elastic constants could be measured precisely only when probing the single crystals.

Selected examples of minerals studied by mean of various techniques for elasticity measurements are referred in table 1-2.

1.3.3 Velocity profiles of Earth's interior

The general structure of the Earth's interior has been known from seismology for about 80 years, and the knowledge of the fine structure is improving continuously. The main divisions are the crust, the mantle and the core. Although, the body of our planet is inhomogeneous, it is generally considered that Earth's interior behaves elastically roughly as a layered sequence of isotropic material. This simplification ignores lateral inhomogeneities that are a much more subtle effect than the radial changes. The primary considerations are the radial dependence of ρ, V_P and V_S. Figure 1.3.1 shows Earth profiles of V_P and V_S versus depth. The regions represented by the figure, the upper mantle, transition zone, and lower mantle, form the rocky part of Earth's interior. These regions, collectively, are called the mantle and they consist primarily of silicate oxide materials. The mantle extends to a depth of about 2890 km, nearly half the way to Earth's radius. D" layer separates silicate mantle and metal core and exhibits anomalous seismic waves gradients. The deeper part of Earth consists of the metallic molten outer core (depth about 2890-5150 km) and solid inner core (depth about 5150-6370 km) (Anderson, 2007).

Compositional models of Earth's interior are constrained by several indirect evidences, including studies on geochemistry, phase equilibrium, and cosmic elemental abundances. The elastic-wave profiles of Earth's interior, however, present especially powerful constraints on possible mineralogical models. Figure 1.3.1 reveals several major features about Earth's mantle that ultimately must be reconciled with the mineral elasticity data. First, there is an overall increase in V_P and V_S with depth in the mantle. Second, the boundary between the upper mantle and transition zone is marked by sudden discontinuities in both V_P and V_S. Third, the rate of increase of V_P and V_S, i.e., $dV_{P,S}/dz$, where z is depth, in the transition zone is greater than the $dV_{P,S}/dz$ for the deeper parts of the upper mantle and for the lower mantle. Finally, there is a second major discontinuity in V_P and V_S between the transition zone and the lower mantle. Any acceptable mineralogical model of the Earth should ultimately explain all the features of the elastic profile of the mantle (Isaak, 2001).
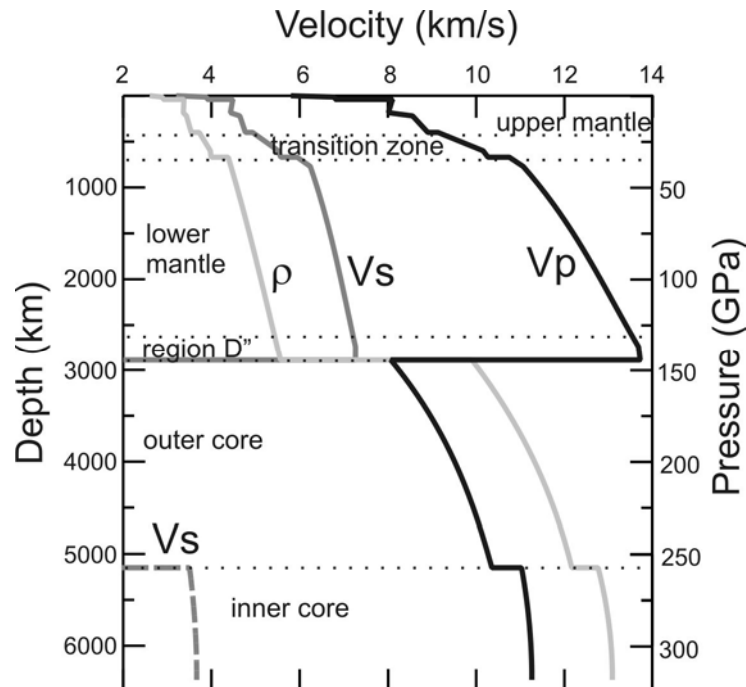
Fig. 1.3.1. V_P and V_S profiles in the Earth (data are taken from Dziewonski and Anderson, 1981).

In order to fit the physical properties of a set of minerals to seismic and density profiles of the deep Earth one could use two general point of view. One approach is to adiabatically decompress the mantle to zero pressure and the temperature appropriate for the foot of the adiabat. The resulting physical properties (density and wave velocities) are then compared with those from zero-pressure data for a set of minerals. This approach was pioneered by Birch (1952) and used by many researchers (e. g. Stacey, 1995 and 1998; Jackson, 1998; Stacey and Isaak, 2000). The primary use of this first method is in applications to Earth's lower mantle. A second method is to use appropriate equations of state and extrapolate mineral properties to the P, T conditions of the mantle for direct comparison with Earth profiles (Isaak, 2001). The consistency of these two approaches, when sufficient data on the P and T effects of elasticity for minerals are available, is demonstrated by Jackson (1998).

The seismic discontinuity at 410 km

The discontinuities in V_P and V_S near 410 km provide a good starting point for constructing compositional models of Earth's mantle. One explanation for this discontinuity is that it represents sudden changes in chemical composition with depth (Anderson and Bass, 1986). It is usually understood, however, that the discontinuities in V_P and V_S near 410 km are related to the phase transition of Mg-rich olivine to the β-phase (Anderson, 2007).

Birch (1952) predicted that around 300-km depth, ferro-magnesium silicates would begin transforming to close-packed, high-pressure phases. Soon afterwards, Ringwood (1956) predicted the olivine-spinel transition. Since that time, the olivine to modified spinel transformation has been demonstrated in the lab (Ringwood and

61

Major, 1966 and 1970; Akimoto and Fujisawa, 1966) and this transition has been used to estimate the amount of olivine in Earth's mantle.

While it is commonly assumed that the four dominant minerals of Earth's upper mantle are olivine, orthopyroxene, clinopyroxene, and garnet, different compositional models ascribe varying amounts (by volume) of these four minerals to the upper mantle. Interestingly enough, each competing model appeals to the 410-km seismic discontinuities for its support. The pyrolite model introduced by Ringwood (1975) assigns the following mixture: olivine, 57%; orthopyroxene, 17%; clinopyroxene (omphacitic), 12%; and garnet (pyrope-rich), 14%. The term "pyrolite model" is understood to be a mineralogical model of Earth's upper mantle containing 50% or more olivine by volume. Since the introduction of pyrolite, other models of the upper mantle with the content of olivine somewhere between 16 and 75% have been proposed (Bass and Anderson, 1984; Bina and Wood, 1987; Weidner, 1985 and 1986; Weidner and Ito, 1987; Anderson, 1988; Duffy and Anderson, 1989; Gwanmesia et al., 1990b; Rigden et al., 1992; Ita and Stixrude, 1992; Duffy et al., 1995b).

The main reason these studies disagree in their conclusions about the amount of olivine in Earth's mantle is that they make different assumptions about the elastic properties of the high-pressure β-$(Mg,Fe)_2SiO_4$ phase at the P, T conditions of the 410-km discontinuity (Isaak, 2001). The amount of olivine in a proposed model would be that required to account for the 4 - 5 % and 4.0 - 4.6 % increase (Grand and Helmberger, 1984; Mechie et al., 1993; Nolet et al., 1994) in the respect to V_P and V_S profiles at 410 km. Room-temperature data on the elasticity of α and β-$(Mg,Fe)_2SiO_4$ indicate that these velocity increase would be satisfied with 30 – 40 % olivine content by volume in the upper mantle (Duffy et al., 1995b). However one should make the comparison at the certain P-T conditions of 410 km (13.8 GPa, 1800 K). The first

measurements for $(\partial K_S / \partial P)_T$ and $(\partial G / \partial P)_T$ for the β-$(Mg,Fe)_2SiO_4$ phase were made on polycrystalline specimens (Gwanmesia et al., 1990b; Gwanmesia and Liebermann, 1992) resulting in respective values of 4.8 and 1.7 (Gwanmesia et al., 1990a). Further measurements on the pressure effects of elasticity of the β-$(Mg,Fe)_2SiO_4$ phase suggest $(\partial K_S / \partial P)_T$ and $(\partial G / \partial P)_T$ are closer to 4.2 and 1.5, respectively (Li et al., 1996a; Li et al., 1998a).

Uncertainty about the temperature derivatives of elastic properties, especially that of the shear modulus, for the β-$(Mg,Fe)_2SiO_4$ phase prevents a more definitive interpretation of the olivine content. If $(\partial G / \partial T)_P$ for the β-$(Mg,Fe)_2SiO_4$ phase has a relatively large (negative) magnitude compared to the α-$(Mg,Fe)_2SiO_4$, the change in V_P and V_S due to the α - β transition will be reduced at elevated temperature, necessitating more olivine in the mineralogy to account for the observed seismic discontinuities (Isaak, 2001).

Elastic properties of the transition zone

The transition zone is the part of the mantle somewhere between 410 and 660 km. In this region the V_P and V_S gradients are greater than can be explained by isochemical and isostructural changes in a mineral assemblage with Mg_2SiO_4 as the main component (Bullen, 1940). The gradients throughout the transition zone could account for the gradual transitions of minerals from low-velocity to high-velocity phases: pyroxene to garnet; β- to γ-$(Mg,Fe)_2SiO_4$; and garnet to perovskite (Isaak, 2001). Researchers, however, are not yet in full agreement on this problem.

At around 100-km depth, orthopyroxene begins to transform to clinopyroxene (Ito and Takahashi, 1987; Irifune, 1987). Around 275 km, orthopyroxene is no longer stable. At about 300 km (10 GPa), the clinopyroxene begins transforming to garnet (majorite). This transformation is complete, however, before 500 km (Gasparik, 1990; Irifune, 1993). The pyroxene to majorite transformation cannot, therefore, explain the high gradients throughout the entire transition zone even if some amount of Ca-rich clinopyroxene persists to much higher pressure as suggested by Ito and Takahashi (1987).

The β- to γ-$(Mg,Fe)_2SiO_4$ phase change is also complete well short of the major discontinuity at about 660 km. Katsura and Ito (1989) find that this wadsleyite-ringwoodite transition terminates between 505 and 545 km. The garnet-perovskite transition begins between 580 and 720 km (Jackson and Rigden, 1998).

Agee (1998) made a review implying that our present understanding of the seismic gradients in the transition zone does not match our knowledge of the elastic minerals present in that region. Jackson and Rigden (1998), however, state that known phase transitions in the region from 410-660 km adequately account for seismic structure of the transition zone. Their conclusion is that the combined effect of the pyroxene to garnet, β- to γ-$(Mg,Fe)_2SiO_4$, and garnet to perovskite transitions produce the overall large gradients in V_P and V_S in the transition zone.

A further complication to interpreting the mineralogy of this region is the possibility of a global seismic discontinuity around 520 km (Shearer, 1990, 1991, 1996; Kato and Jordan, 1999; Gaherty et al., 1999). This discontinuity is much more subtle than the discontinuities at 410 km. Some have even questioned whether the resolution of the seismic is sufficient to see discontinuous changes in wave velocities

at 520 km (Bock, 1994), although the prevailing understanding is that this discontinuity is indeed present.

Agee (1998) discusses possible causes for a 520-km discontinuity in terms of: (1) the β- to γ-$(Mg,Fe)_2SiO_4$ phase change; (2) the clinopyroxene + majorite garnet to majorite garnet + perovskite transition; (3) a combination of (1) and (2); and (4) a compositional change. The β- to γ-$(Mg,Fe)_2SiO_4$ transition is the most widely accepted explanation for the 520-km discontinuity. Jackson with coauthors (2000) measured the elastic properties of γ-$(Mg,Fe)_2SiO_4$ to 873 K using Brillouin scattering and concluded that olivine content of 30-50% in the transition zone is sufficient to account for the shear impedance contrast at 520 km. Conclusions based on compressional waves are less strict because of the uncertain value of $(\partial K_S / \partial P)_T$ of the β-phase (Fei et al., 1992; Meng et al., 1993; Li et al., 1998b). Jackson with co-authors (2000) also note that some studies indicate relatively large local (sub-Eurasian mantle) values for ΔV_P (~2-3%) (Mechie et al., 1993) and discuss the difficulty in explaining these changes in terms of the β- to γ-$(Mg,Fe)_2SiO_4$ transition for a mineral assemblage of even 100% olivine. They suggested that local instances of chemical heterogeneity may explain such large changes in ΔV_P, and they cite the accumulation of subducted material above the 660-km discontinuity as one possible mechanism.

The seismic discontinuity at 660 km and the lower mantle

The second major discontinuity in seismic wave velocities occurs at 660-km depth. It is now widely accepted that this discontinuity represents the breakdown of olivine to perovskite $(Mg,Fe)SiO_3$ and magnesiowüstite $(Mg,Fe)O$. Ming and Bassett (1975) observed the breakdown of a range of compositions of olivines at 25 GPa and

1700ºC. Their interpretation was similar to what others suggested at that time - the new phases were believed to be magnesiowüstite and stishovite. Soon afterwards, Liu (1976) and Ito (1977) found that Mg_2SiO_4 spinel disassociates to $MgSiO_3$ perovskite and MgO periclase. Now there exists a large body of experimental evidence that points to the disassociation of spinel to perovskite and magnesiowüstite as the reason for the 660-km discontinuity. The implication from the olivine phase diagram is that this depth, which is at a pressure of 24 GPa, has a corresponding temperature of about 1900 K (Ito and Katsura, 1989). Many details of 660 km discontinuity are still not clear. Many questions regarding influence of minor components (Ca, Al, fluids) still remain open. Iron partitioning between perovskite and magnesiowüstite which could have dramatic effect on this dissociation reaction remains controversial (Frost and Langenhorst, 2002; McCammon, 1997; Lauterbach et al., 2000). Several interesting effects in addition to the density and elasticity gradients discontinuity also occur on this boundary. For example, $(Mg,Fe)_2SiO_4$ polymorphs (olivine, wadsleyite and ringwoodite) does not incorporate significant amount of Al^{3+} and Fe^{3+} in their crystal structure. Contrary, perovskite easily incorporates a large amount of Al^{3+} substituting Si^{4+} in octahedral position, and charge balance could be easily maintained by oxidation of Fe^{2+} to Fe^{3+}. The upper/lower mantle boundary therefore also represents a strong gradient in Fe^{2+}/Fe^{3+} ratio in the Earth interior (McCammon, 2005).

Below 660 km the velocity profile varies relatively smoothly without sharp discontinuities with depth. These profiles also indicate that from 660 to 2700 km (about 200 km before the core-mantle boundary) the physical properties can be described in terms of a chemically and structurally homogeneous material that is self-compressing.

Relative amounts of major Earth mantle phases could be calculated within general thermodynamics with the experimental inputs of several parameters including elastic properties (Fig. 1.3.2).
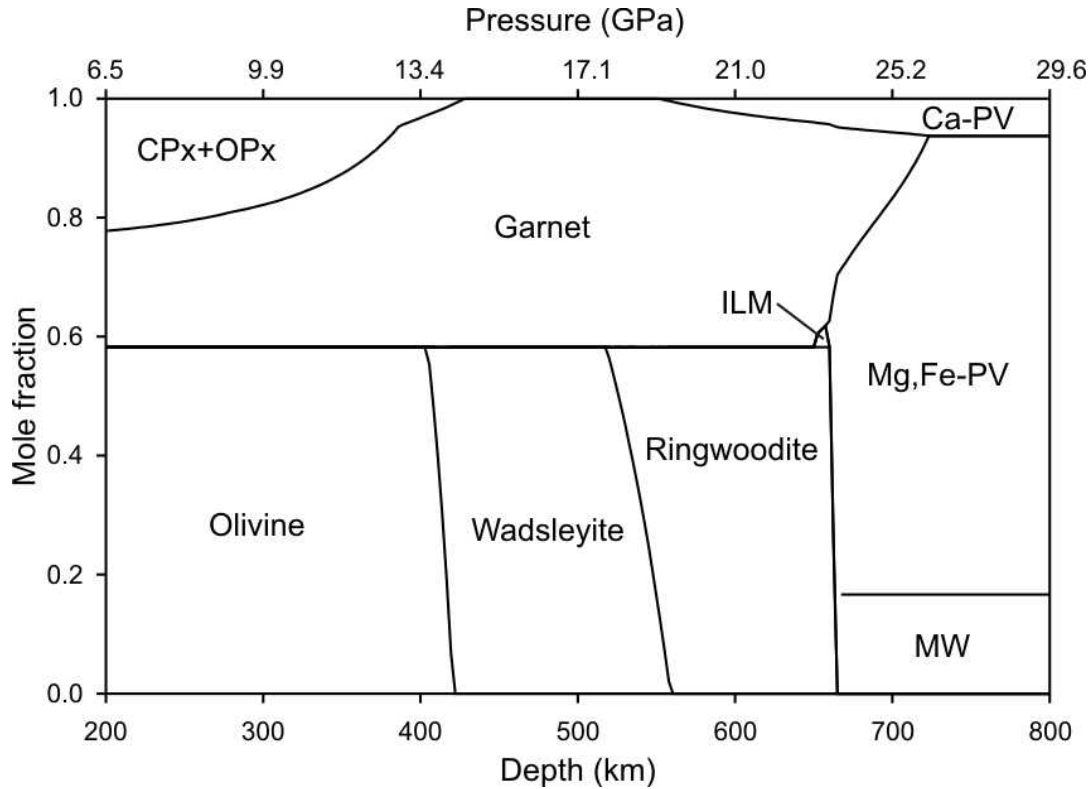
Fig. 1.3.2. Mole fraction of main mantle minerals as a function of depth. "CPx" and "OPx" – ortho- and clino-pyroxenes; olivine, wadsleyite and ringwoodite are α, β, and γ-$(Mg,Fe)_2SiO_4$, "ILM" – ilmenite, "MW" – $(Mg,Fe)O$ magnesiowüstite, "Mg,Fe-PV" – $(Mg,Fe)(Si,Al)O_3$ perovskite, "Ca-PV" – $CaSiO_3$ perovskite.

If the compressibility, bulk and shear moduli of these minerals are known, V_P and V_S could be calculated in order to compare to seismological observations (Fig. 1.3.3, 1.3.4). General trends are reproduced correctly, however, in many fine details there is still no good agreement between those two profiles.
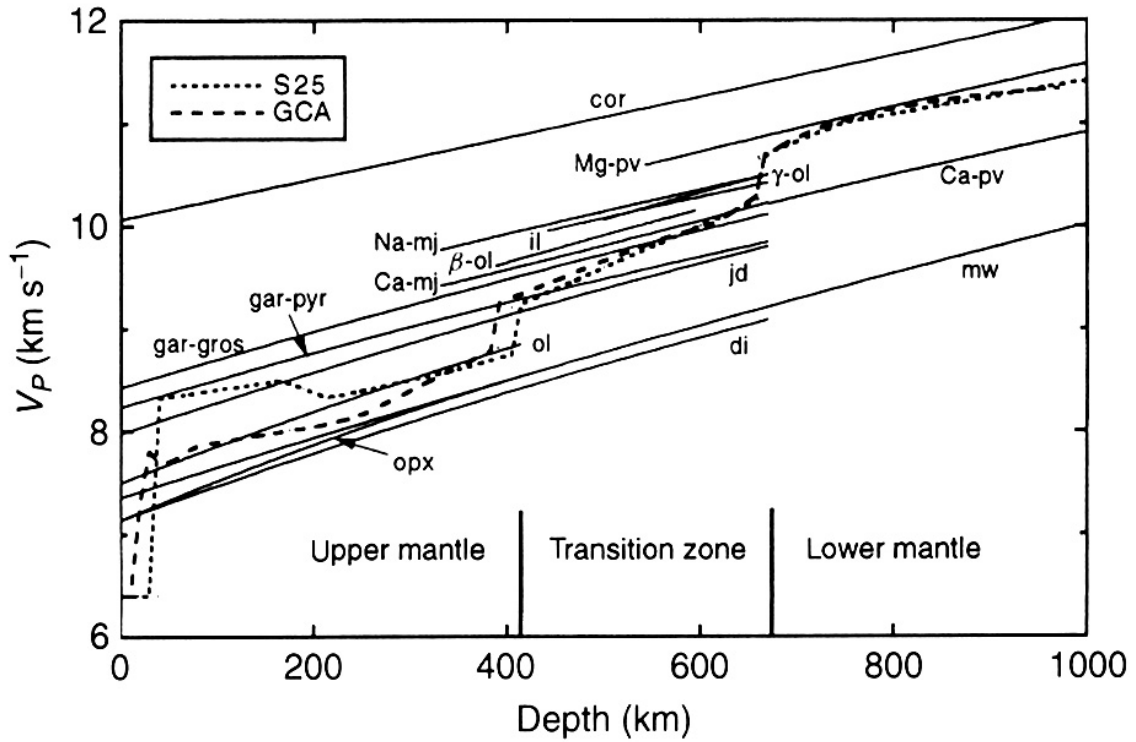
Fig. 1.3.3. Comparison of mineral V_P values determined initially along an adiabatic geotherm with Earth V_P profile. "S25"-dependence is taken from LeFevre and Helmberger (1989); "GCA" - from Walck (1984). Mineral names are as following: "cor" – corundum; "Mg-pv" – $(Mg,Fe)SiO_3$ perovskite; "Ca-pv" – $CaSiO_3$ perovskite, "ol" – olivine, "β-ol" – wadsleyite, "γ-ol" – ringwoodite, "Na-mj" and "Ca-mj" – sodium and calcium-rich majorites, "il" – ilmenite, "opx" – orthopyroxene, "di" – diopside, "jd" – jadeite, "gar-pyr" and "gar-gross" – pyrope and grossular garnets, "mw" – magnesiowüstite (after Duffy and Anderson, 1989).
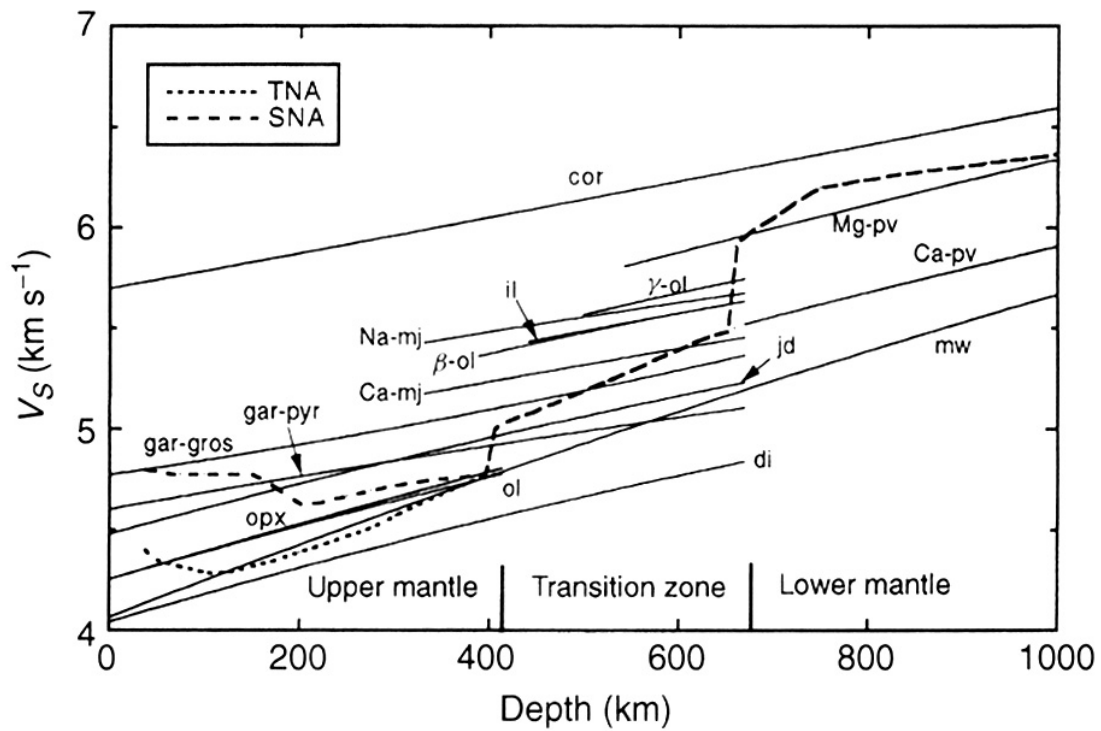
Fig. 1.3.4. Comparison of mineral V_S values determined initiated along an adiabatic geotherm with Earth V_S profile. See Fig. 1.3.3 for notations. After Duffy and Anderson (1989).

1.4 Aims of the study

In order to interpret seismic observations from the point of view of mineral physics and to clarify most of the abovementioned problems very high-quality experimental data on high-pressure and high-temperature elastic properties of minerals are necessary. Such data could be provided mostly from single-crystal elasticity data investigated by mean of Brillouin scattering experiments. Many of geologically important minerals are not transparent, and ultrasonic interferometry combined with diamond-anvil cell technique is one of the best solutions of described above problems. This gives the motivation for this work that is the development of *in*

situ high-pressure and high-temperature GHz interferometry at Bavarian Geoinstitut and application of this and other experimental techniques to study high-pressure and high-temperature elasticity of minerals.

Chapter 2

Developed methods and instrumentation

2.1 GHz ultrasonic interferometry laboratory at Bavarian Geoinstitut (BGI)

One of the main goals of the present work was the development of the gigahertz ultrasonic interferometry (GUI) system for the *in situ* high-pressure and high-temperature measurements of sound velocities in crystals. Although possibility of simultaneous high-pressure and high-temperature GUI measurements in diamond anvil cell was demonstrated already five years ago up to temperature of 250°C (Jacobsen et al., 2002b), *in situ* pressure measurements were not possible. The necessity of determination P and T simultaneously always appears because pressure in diamond anvil cell changes upon heating. So raised a problem of developing the experimental setup for simultaneous sound velocities measurements and pressure determination under high temperature.

Over 50 years ago, Birch (1952) recognized that the constitution of Earth's inaccessible interior could be interpreted from seismological observation, provided that the elasticity of its constituent materials could be measured or calculated at relevant

conditions of pressure and temperature in the laboratory. A new gigahertz ultrasonic interferometer with shear-wave capabilities (Jacobsen, 2002a) has been developed for high-pressure and high-temperature elasticity measurements in the diamond anvil cell (DAC). The acoustic instrumentation can be interfaced to nearly any type of DAC, and measures single-crystal compressional and shear-wave travel times with high precision. Measured travel times and their P–T derivatives are converted to sound velocities and elastic moduli for direct application to problems in geophysics.

Gigahertz-ultrasonic interferometry was initially developed by Spetzler et al. (1993), although the idea of using high-frequency ultrasound (at ~100 MHz) in order to study micro-crystals and to eliminate unwanted diffraction effects can be traced back to McSkimin (1950). By extending ultrasonic measurements to thousands of MHz (i.e. GHz), the acoustic wavelengths in minerals are reduced to a few micrometers (μm), permitting single-crystal ultrasonic travel-time studies on samples as thin as a few 10's of μm in length. Since its initial application in the gas-loading piston–cylinder at Colorado (Chen et al., 1996), the GHz technique, at various stages of development, has been used successfully in the DAC with compressional waves (Spetzler et al., 1996; Shen et al., 1998; Reichmann et al., 1998; Bassett et al., 2000). Later a new method of generating GHz shear-waves has been developed for ultrasonic interferometry (Jacobsen et al., 2002a), and has already been used to determine the complete elastic tensor of a high-pressure phase of silicate ringwoodite (Fo_{90}) recovered from the multi-anvil press (Jacobsen et al., 2004a). Shear-waves have since been transmitted into the DAC for acoustic interferometry (Jacobsen et al., 2004b), and the elastic tensor of some opaque iron-oxide minerals including magnetite (Reichmann and Jacobsen, 2004), magnesiowüstite (Jacobsen et al., 2002a), and wüstite (Kantor et al., 2004a) have been determined to ~10 GPa.

Transducers and buffer rods

Ultrasonic interferometry is a single-transducer delay-line experiment. The basic principles are unchanged from MHz-ultrasonic interferometry (see section 1.2 in Chapter 1), with the major exceptions being within the electronics and transducer technology, discussed in this section. GHz frequency electronics require special attention because high-frequency electromagnetic fields suffer higher attenuation in cables and are extremely sensitive to impedance mismatch. There are additional complexities for high-pressure ultrasonics because the travel-time of the carrier signal through the cables and circuitry approaches that of sound velocities through thin mineral plates, causing additional interference effects. The design challenges for ultrasonics at GHz frequencies have therefore mainly to do with impedance matching to avoid unwanted reflections in the circuitry.

Contact to the delicate transducers, which are only about 1 μm thick, is made through transmission-line connectors, designed to match the nominal 50 Ω impedance of the system. Transmission lines consist of a conductor–insulator–conductor sandwich; one measures about 1 mm thick and 3 mm wide, and is soldered to a standard SMA connector. The lead contact consists of a polished pin mounted onto the end of a leaf spring, which protrudes through the insulating and ground layers. Contact to the transducer is made by gently pushing the transmission line against the transducer. With these connectors, no additional soldering is necessary and different buffer rods can be switched in-and-out of the same connector.

The transducers used for producing the primary waves are thin-films of ZnO, developed in collaboration with K. Müller and H. Ohlmeyer at the University of Bayreuth. Figure 2.1.1 shows the structure of a compressional wave transducer. Thin

films of chrome (5–10 nm thick) and then gold (~500 nm thick) are vacuum-coated onto a single-crystal buffer rod substrates, usually made of *c*-axis sapphire (Al_2O_3) for P-waves or [100]-oriented cubic yttrium aluminium garnet ($Y_3Al_5O_{12}$ or simply "YAG") in the case for shear-waves. Deposition of the zinc oxide (ZnO) transducer is a sputtering process, requiring about 2 hours for each micron of ZnO growth. To achieve transducers that can be driven at ~0.5–2.5 GHz, the ideal ZnO transducer thickness is 1.5 μm. Finally, a second Cr–Au layer is precision coated onto the transducer for the lead contact. The diameter of the ZnO is normally about 1 mm, and the diameter of the top electrode is about 0.3 mm (Jacobsen et al., 2005a) (Fig. 2.1.1).

The compressional waves produced by this kind of transducers even at GHz-frequencies have very good quality, but they are not suitable fro producing shear waves. For the time being there are no shear-wave transducers for such high-frequencies available. Earlier it was tried by Chen and co-workers (Chen et al., 1997) to thin down a commercial MHz-frequency ultrasonic shear transducer produced near-GHz shear-waves. Unfortunately all they could do was a transducer of relatively low quality and only over a narrow frequency range of 590–605 MHz. Later the problem was solved by Jacobsen and co-workers with developing a GHz shear-wave buffer rod that produces purely polarized shear-waves by P-to-S conversion (Jacobsen et al., 2002a) (Fig. 2.1.2).
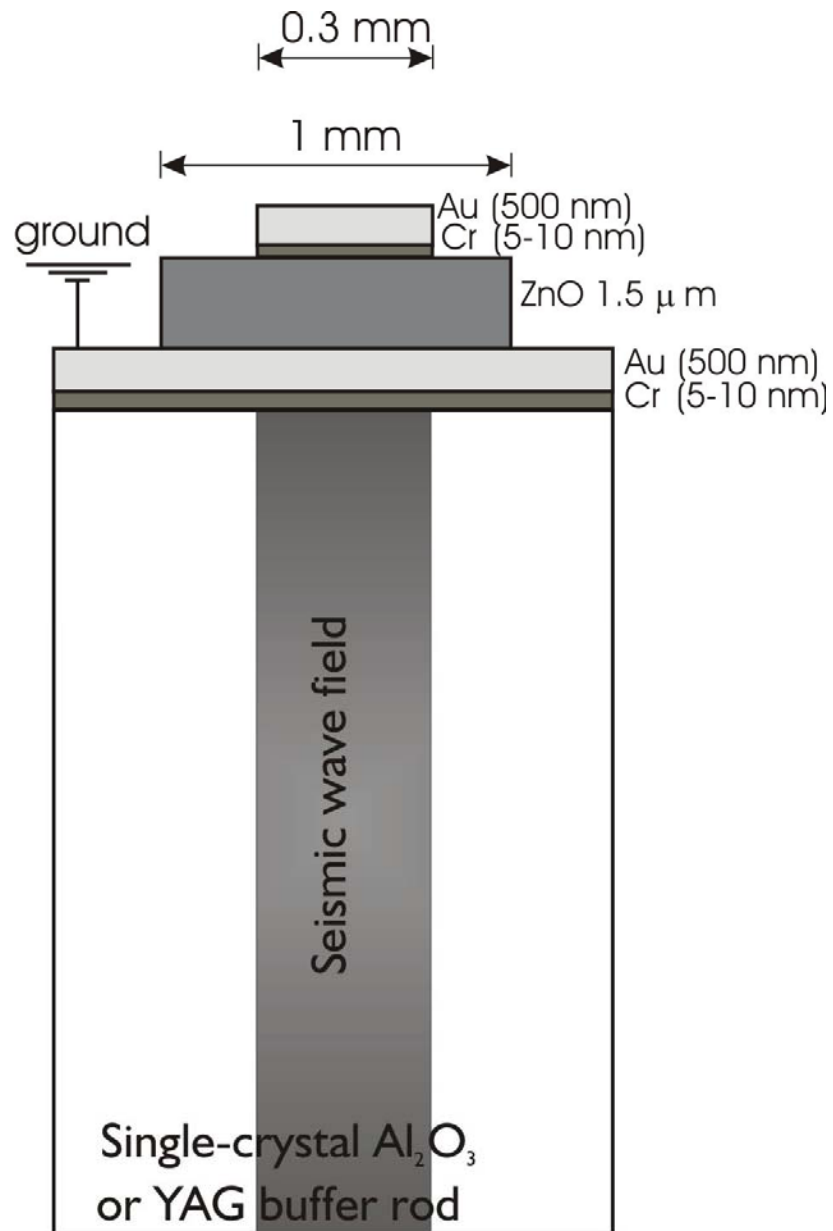
Fig. 2.1.1. Schematic view of the thin-film piezoelectric transducer, sputtered onto a single-crystal buffer rod for ultrasonic interferometry.
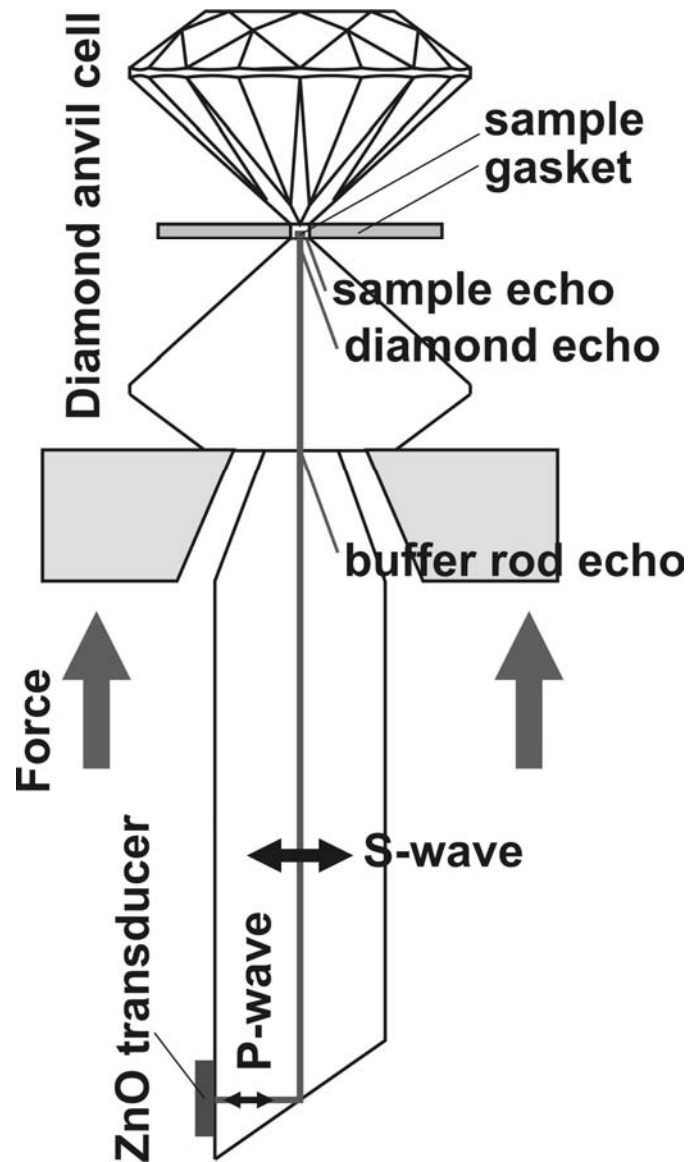
Fig. 2.1.2. Schematic view of the high-pressure ultrasonic experiment for shear-waves measurements.

The GHz shear-wave buffer rod works on the principle of Snell's law. An incident P-wave strikes a polished conversion facet on a YAG single crystal at an angle of incidence (i) such that the converted S-wave is orthogonal to the incident P-wave (Fig. 2.1.2). If the incident P-wave is travelling in the [100] direction of the cubic YAG crystal, from Snell's law, the velocities are:

$$\frac{V_P^{[100]}}{\sin(i)} = \frac{V_S^{[010]}}{\sin(j)}, \tag{2.1}$$

where the angles i and j are measured between the incident P and converted S-wave from the normal of the conversion facet. For the converted shear-wave to propagate as a pure shear-wave (i.e. no compressional component or splitting), it must travel in another pure-mode direction (e.g. [010] for the cubic crystal buffer rod). The S-wave will be orthogonal to the incident P-wave when $i + j = 90º$. Substituting $i = 90º - j$ into Eq. (2.1) and using the identity $sin\,(90º\text{-}j) = cos\,(j)$ yields:

$$\frac{\sin(i)}{\cos(i)} = \tan(i) = \frac{V_P^{[100]}}{V_S^{[010]}}, \tag{2.2}$$

which gives the angle of incidence (i) producing an orthogonal conversion in any cubic crystal. For YAG, there were $V_P^{[100]}$ and $V_S^{[010]}$ velocities measured on the bench and determined $i = 59.5º$. The useful feature of a P-to-S conversion buffer rod is that the polarization of the shear-wave is known precisely, being defined by direction of the incident P-wave because there is no rotation of the polarization vector across the conversion (Jacobsen et al., 2002a).

Electronic components

The high-frequency ultrasonic interferometer consists of four main components: (1) a radio-frequency (RF) generator or microwave synthesizer, (2) a pulse generator – either internal to the microwave synthesizer or external to the RF signal generator, (3) a high-frequency digitizing main-frame oscilloscope with trigger and channel set, and (4) a personal computer to drive the system and save the raw amplitude data.

The signal generator provides a highly stable radio-frequency (RF) source to the interferometer. This allows measuring ultrasonic travel times to a small part of an interference fringe, or about 1 part in 10^4 if the round-trip travel-time through a sample is about 100 ns (samples 0.2–0.6 mm thick) and to about 1 part in 10^3 if the sample thickness is an order of magnitude shorter (in the DAC). The GHz system in BGI uses the Gigatronics 6062A signal generator, with 10 MHz to 2.1 GHz bandwidth, 0.1 kHz resolution, output power up to 12 dB, and high-stability 10-MHz quartz-oscillator reference.

The continuous output from the RF generator is gated by a pulse generator, providing phase-coherent pulses of programmable duration and delay. The GHz-system in BGI uses the Stanford Research Systems DG535 Digital Delay/Pulse Generator, but in practice the instrument could be internal to a microwave synthesizer provided that it can produce gated signals as short as ~100 ns in duration and with appropriately fast rise times of about 3–5 ns (Jacobsen et al., 2005a).

The digitizing oscilloscope has GHz-bandwidth and picoseconds resolution. The interferometer now at the BGI uses the HP54750 system (i.e. HP54750A scope with the 20 GHz HP54751A trigger module). The systems provide a maximum of 500 ps/div resolution (5 ns full window) when the trigger rate is 10 kHz.

Data collection and reduction

Ultrasonic P- and S-waves are delivered to the sample through the buffer rod (and one of the [100]-oriented diamond anvils in case of high-pressure experiment). Acoustic coupling between the buffer rod and the sample (or one of the diamond anvils) is achieved by applying a small mechanical force. In high-pressure experiments the sample

must have also a good acoustic coupling to the acoustic diamond. Impedance contrasts at the buffer rod – diamond interface, the diamond – sample interface, and at the sample – pressure medium interface produce reflections, which are detected by the source transducer (Jacobsen et al., 2005a). The round trip through the system is normally about 3 μs. Echo train at 1.2 GHz from the shear-wave buffer rod and attached sample of San-Carlos olivine is shown in Figure 2.1.3.
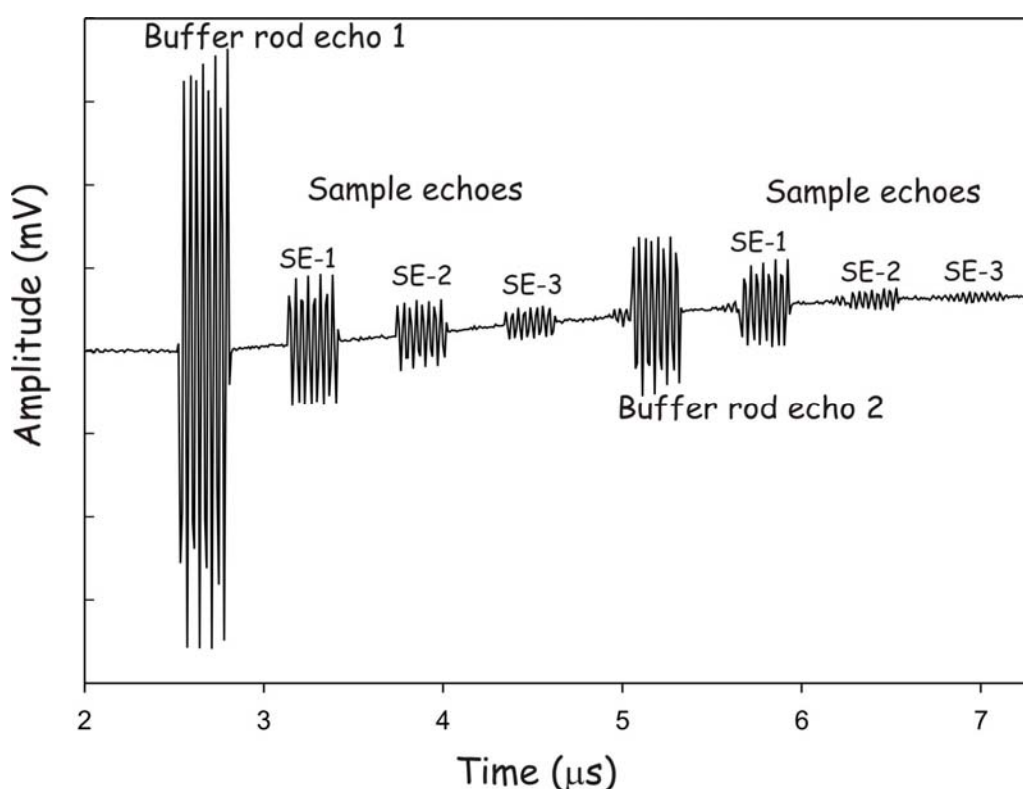

Fig. 2.1.3. Echo train at 1.2 GHz showing reflections internal to the buffer rod and multiple S-wave echoes from the sample at ambient conditions.

In both ambient and high-pressure experiments the travel time is extracted from the interference data achieved by overlapping the acoustic echoes from buffer rod and sample (or diamond and sample). An interference pattern is produced by measuring the amplitude of the combined signal at a position where there is first-order interference between the diamond and sample echoes and scanning the frequency (Fig. 2.1.4). Travel

times are determined from each fitted frequency maxima and minima of interference by experimentally fitting the integer number of wavelengths in the round trip through sample. Additional details on data reduction are given by Spetzler et al. (1993).
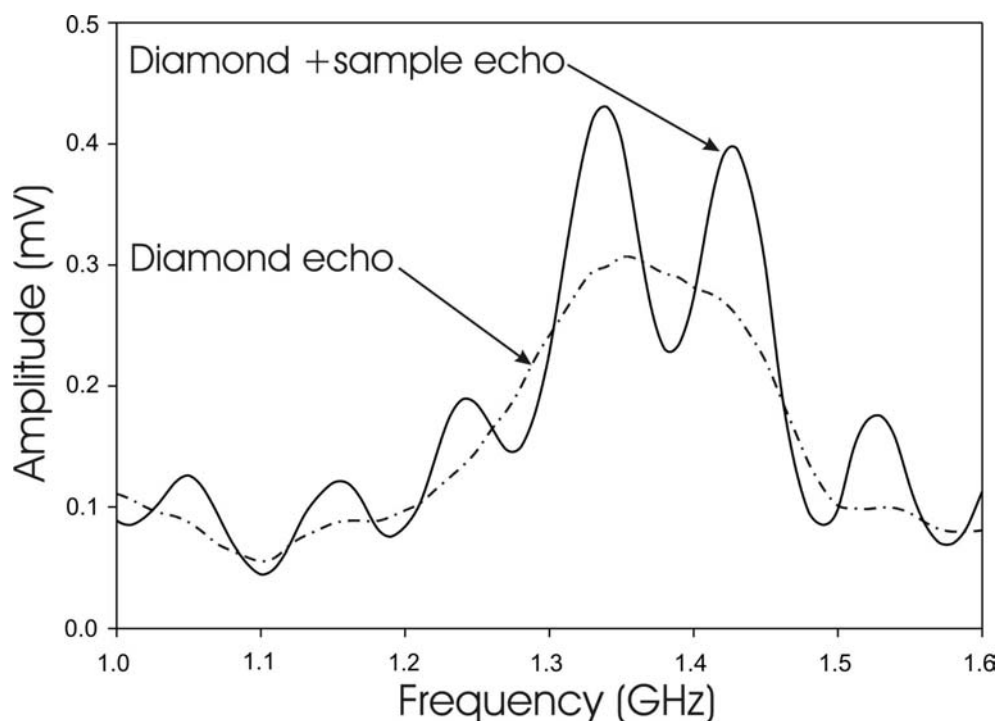
Fig. 2.1.4. Compressional-wave interferometry data from a crystal of $Fe_{0.94}O$ at ~8.1 GPa in the diamond anvil cell.

Diamond anvil cell and equipment for simultaneous high-pressure and high-temperature ultrasonic measurements

GHz-ultrasonic interferometry can be interfaced to nearly any type of diamond anvil cell (DAC), provided that the buffer rod fits into the conical access of the diamond anvil supporting seat for direct contact to the back of the diamond anvil. In the hydrothermal DAC (Bassett et al., 2000), ultrasonic interferometry has been carried out to ~9 GPa at room temperature (Reichmann and Jacobsen, 2004), and to 250°C at ~2.5 GPa (Jacobsen et al., 2002b). A miniature three-pin DAC 30 mm in diameter is now used

for ultrasonic measurements in Bayerisches Geoinstitut. For simultaneous high-temperature experiments the DAC is equipped with a miniature internal resistive heater (Fig. 2.1.5) (Kantor et al., 2005a) with thermocouple fixed at a very small distance from the sample chamber. Temperature of the cell is controlled by back-feed power supply system with accuracy of 1 to 3 K within time of measurements.
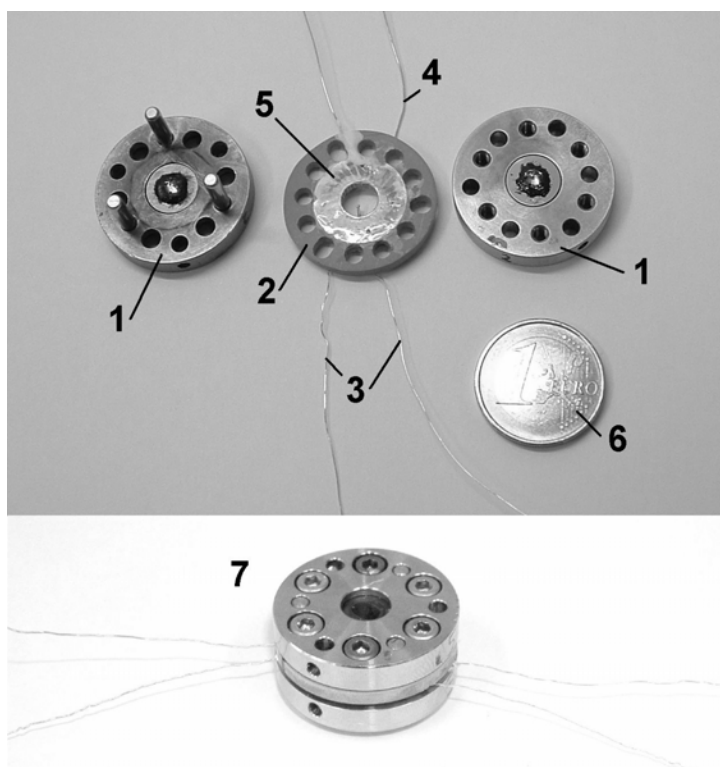
Fig. 2.1.5. Diamond anvil cell with the heating assembly for high-P, T GHz experiments: 1 - diamond anvil cell; 2 - ceramic (pyrophilite) heater; 3 – thermocouple; 4 - platinum wires; 5 - mica for electrical isolation; 6 - one Euro coin for scale; 7 - entire assembly (after Kantor et al., 2005a).

DAC is mounted inside a tilting platform (Fig. 2.1.6-A) fixed on the end of the rotating hand (Fig. 2.1.6-B), and can be moved to three different positions: on the top of a P-buffer rod for compressional wave velocities measurement, on the top of S-buffer rod for shear wave velocities measurement and under the microscope, equipped with laser

and portable high-resolution spectrometer for ruby fluorescence measurements (Fig. 2.1.6-C). DAC under high temperature could be easily moved between these three positions, and independent pressure, temperature, S- and P-wave velocities measurements could be done simultaneously at each data point (Fig. 2.1.6-D).
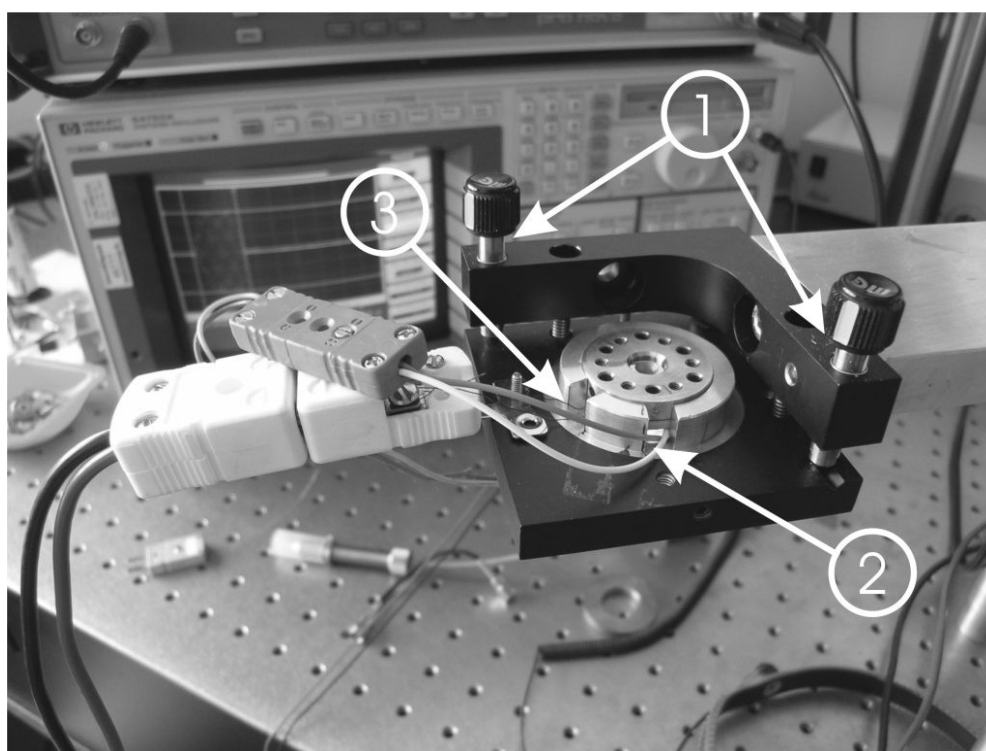
Fig. 2.1.6-A. Diamond anvil cell mounted for high-*P* and high-*T* experiment: 1 – two screws for tilting cell alignment; 2 – R-type thermocouple; 3 – wires from the internal resistive heater.
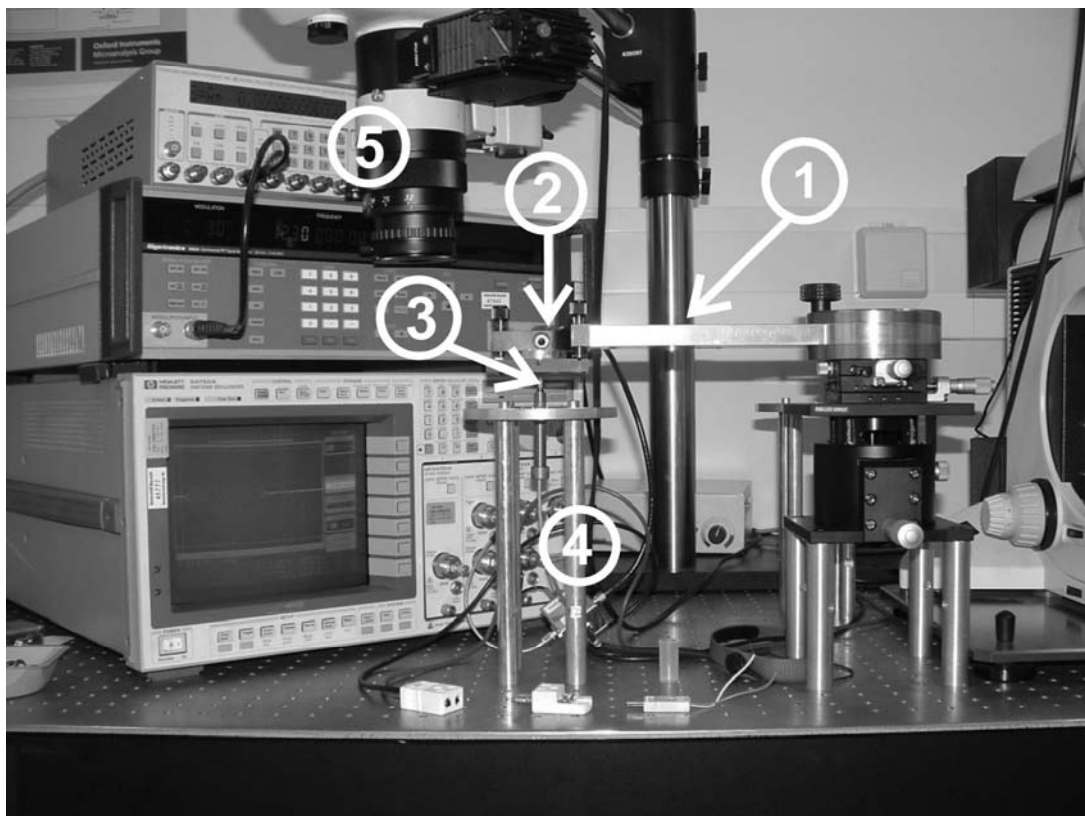
Fig. 2.1.6-B. The rotating hand (1) places the DAC (2) on the top of P-BR (3) fixed in a holder and a stage (4). The microscope (5) is used for performing the visual alignment of DAC against a buffer rod.
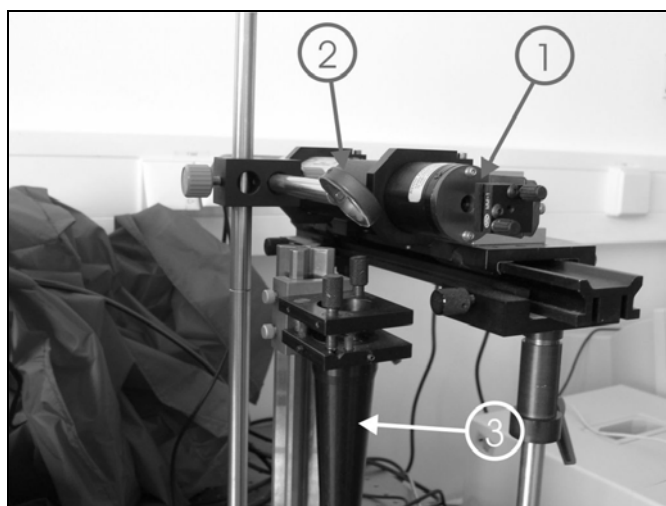
Fig. 2.1.6-C. The laser for *in situ* pressure measurements: 1 – He-Ne laser; 2 – beam splitter (semitransparent mirror); 3 – focusing lens of the detector (high-resolution compact spectrometer).
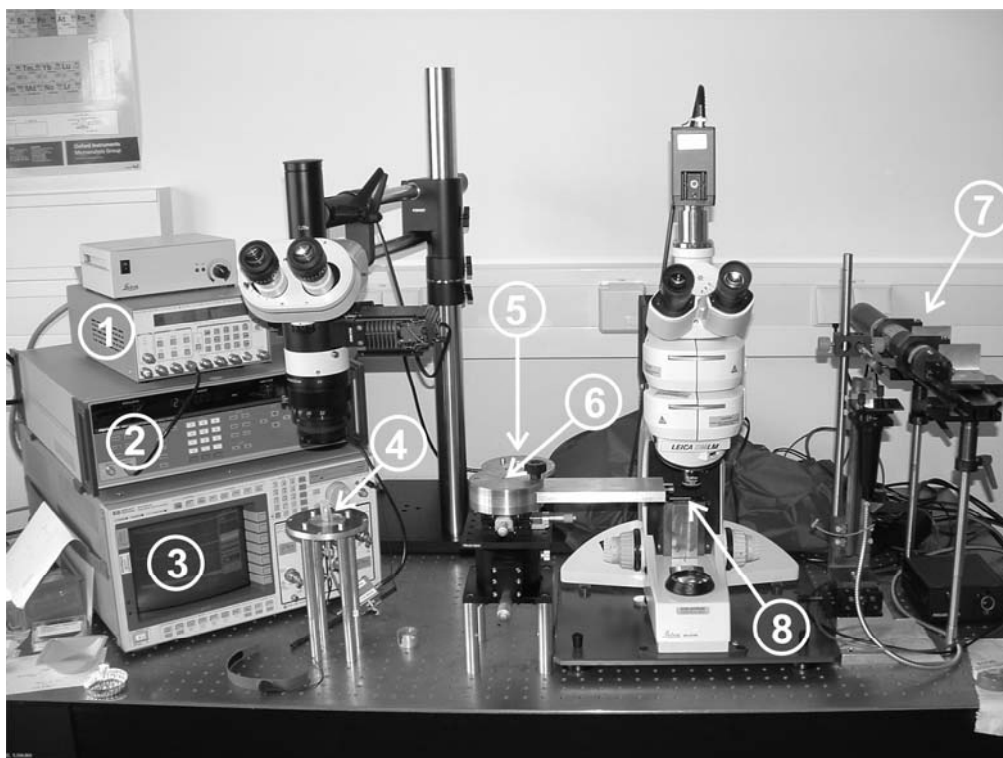
Fig. 2.1.6-D. New experimental setup for GHz high-*P,T* experiments: 1 – pulse generator; 2 – RF signal generator; 3 – sampling oscilloscope; 4 - stage for P-buffer rod; 5 – stage for S-buffer rod; 6 – rotating stage; 7 – laser for pressure calibration; 8 – DAC fixed inside a tilting assembly.
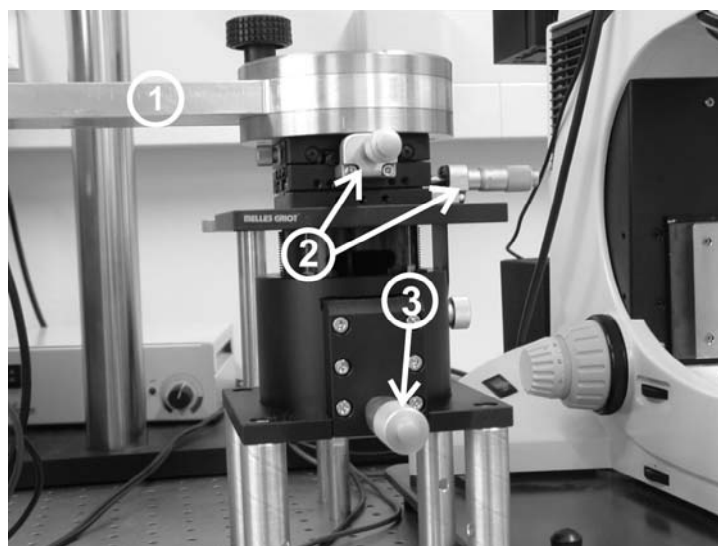
Fig. 2.1.6-E. XYZ-stage allows aligning the DAC against buffer rot: 1- rotating hand, connecting the tilting platform (with DAC fixed in it) with the XYZ-stage; 2- X- and Y- translation screws; 3 – Z-translation screw.

The alignment is achieved by visually inspecting the polished flat of the buffer rod against the acoustic anvil using a zoom stereomicroscope with on-axis illumination (see Fig. 2.1.6-B). The buffer rod is fixed in a holder and could be only moved up and down for few millimetres, while the DAC is sitting in a tilting assembly attached to a XYZ-stage (Fig. 2.1.6-E), that provides a simple way to align the diamond surface against the buffer rod. While the diamond cell is still open, the polished flat of the buffer rod, typically about 250–300 μm in diameter is carefully brought close to the diamond table. The interference fringes between the flat and the diamond are used to guide the buffer rod parallel to the diamond table. Parallelism is achieved using a tilting platform in which the DAC sits, while within a plane the DAC could be easily moved using X-Y translation set (see Fig. 2.1.6-D). Finally, once the buffer rod flat appears grey or black against the diamond, the buffer rod is pushed up against the diamond with an advancing screw. The positions of the XYZ-screws are recorded and after loading the DAC could be placed exactly the same way. Some fine adjustment is possible also after loading the cell.

Preparing the experiment

The samples are prepared as oriented single-crystal plates; polished with parallel faces and flat to about $\sim 1/10\lambda$ with thicknesses ranging from about 25 to 40 μm. The plates have a finish polishing of optical quality, and are placed directly on the culet of the acoustic transmitting anvil. Samples are oriented with single-crystal x-ray diffraction, resulting in a typical uncertainty of about ±1°, due mainly to transferring of the crystal from the diffractometer to a glass slide for polishing. The number of orientations required to obtain the complete tensor depends on the crystal system of the mineral (see section 1.1.1). For example, in the cubic system, just one crystal oriented on [110] direction

could be used to determine all three C_{ij} because there is one compressional and two shear modes, but it is preferable to have two or three pure-mode directions for redundancy (see Eqs. 2.5 – 2.11 below). The number of measurements required to obtain all the C_{ij} increases with decreasing symmetry such that six different orientations would be required to obtain the nine unique C_{ij} in the orthorhombic system and so on.

Samples are kept in place on the acoustic anvil by adding a small amount of silica aerogel to the usual 16:3:1 methanol:ethanol:water pressure-transmitting medium. Aerogel is a highly compressible porous material with the lowest density of any known solid ($\rho \sim 0.1$ g/cm^3). Once wetted, the gel acts like a transparent sponge to gently press the sample against the anvil, while the overall pressure-transmitting medium remains alcohol. The uniaxial stress produced by aerogel is negligibly small compared to hydrostatic pressure and elastic moduli of minerals, and stress conditions in the DAC can are considered as pure hydrostatic pressure (Jacobsen et al., 2005a).

The described setup was used for the high-pressure measurements up to about 10 GPa. The oriented diamond anvils with the culet size of 400-500 μm were used. The 200-300 μm-thick steel or rhenium gasket typically is pre-indented to 80–100 μm thickness, and a 200-300 μm-diameter hole is drilled for samples that are typically 25–40 μm thick and 150–200 μm wide. Pressure is determined using the ruby fluorescence scale (Mao et al., 1986). The pressure was limited to about 10 GPa by solidification of the used pressure-transmitting medium. Above this point the sample bends under the non-hydrostatic pressure and the measured back-echo signal does not allow calculating elastic constants because stress tensor is unknown.

Calculating elastic constants and moduli from single-crystal ultrasonic data

Compressional (V_P) and shear (V_S) velocities are related to the sample length (L) and the measured round-trip travel times (t) by:

$$V = 2L/t \qquad (2.3)$$

At ambient pressure, the length can be measured with a micrometer when the sample is sufficiently thick (i.e. > 0.1 mm). In the DAC, samples have typically only 25–40 μm thickness, so often the initial length is calculated from the measured zero-pressure travel-time using a known velocity measured on a thicker sample. In the case that a thick sample is not available, the initial thickness can be measured using laser interferometry. The elastic constants at ambient or high pressures are determined from the acoustic travel times from similar identities:

$$C_{ij} = C_{ij}^0 (\rho/\rho_0)(L/L_0)^2 (t/t_0)^2, \qquad (2.4)$$

where the zero subscript or superscript indicates an initial (ambient pressure) value, ρ is the density, and the subscripts ij indicate the element of the elastic tensor corresponding to the various pure-mode directions in the single crystal. In the cubic system:

$$C_{11} = \rho \left(V_P^{[100]} \right)^2 \qquad (2.5)$$

$$C_{44} = \rho \left(V_S^{[100]} \right)^2 \qquad (2.6)$$

$$C_{11} + 4C_{44} + 2C_{12} = 3\rho \left(V_P^{[111]} \right)^2 \qquad (2.7)$$

$$C_{11} + C_{44} - C_{12} = 3\rho \left(V_S^{[111]} \right)^2 \qquad (2.8)$$

$$C_{11} + 2C_{44} + C_{12} = 2\rho \left(V_P^{[110]} \right)^2 \qquad (2.9)$$

$$C_{11} - C_{12} = 2\rho \left(V_S^{[110]} pol^{[-110]} \right)^2 \qquad (2.10)$$

$$C_{44} = \rho \left(V_S^{[110]} pol^{[001]} \right)^2 \tag{2.11}$$

The superscripts to V indicate the crystallographic direction of wave propagation and the superscripts to pol indicate the direction of shear-wave polarization if it is not degenerated (Brugger, 1965). The change in length with pressure in a cubic mineral is given by:

$$L(P) = L_0 \left[\rho(P) / \rho_0 \right]^{-1/3} \tag{2.12}$$

where $\rho(P)$ can either be measured *in situ* with x-ray diffraction, or, calculated from a known P–V equation of state such as the third-order Birch-Murnaghan (Eq. 1.41, see Chapter 1).

Once the full elastic tensor is known (C_{11}, C_{44}, C_{12}), the isotropic equivalent or polycrystalline bulk (K_S) and shear (G) moduli can be calculated. The methods of Voigt and Reuss assume uniform strain, or uniform stress, respectively. Hill (1952) showed that the Voigt and Reuss limits represent upper and lower bounds of the isotropic moduli, so the widely used Voigt–Reuss–Hill (VRH) method simply refers to the average, although there is no physical basis for it. The Voigt and Reuss bounds are equivalent for the bulk modulus in a cubic crystal:

$$K_S = 1/3 \left(C_{11} + 2C_{12} \right) \tag{2.13}$$

The Voigt (G_V) and Reuss (G_S) bounds on the shear modulus of a cubic crystal are:

$$G_V = 1/5 \left(2C_S + 3C_{44} \right) \tag{2.14}$$

$$G_R = \frac{5C_S C_{44}}{2C_{44} + 3C_S} \tag{2.15}$$

where

$$C_S = 1/2 \left(C_{11} - C_{12} \right) \tag{2.16}$$

Ultrasonic data from polycrystalline material

Many of high-pressure phases cannot be synthesized as a quality single-crystal. In addition, high-pressure reconstructive transitions often destroy single crystals under *in situ* study. Ultrasonic measurements are routinely made at MHz frequencies (with millimetre wavelength) on polycrystalline samples with grain sizes of about 50μm, resulting in a wavelength-to-grain size ratio of about 20. At 1 GHz the acoustic wavelengths in minerals are about 1-10 μm. It is therefore theoretically possible to perform the acoustic elasticity experiments at GHz frequencies on polycrystalline samples with grain sizes of about 50 nanometres or less. The possible application of gigahertz ultrasonic interferometry to nano-polycrystalline materials is being explored.

The idea was tested and confirmed by preparing several nanocrystalline samples under high-pressure. TiO_2 anatase with grain size about 30 nm compressed in a DAC with 800 μm culets. The sample was squeezed between two diamonds up to about 14 GPa using a hardened-steel gasket pre-indented to the thickness of 80 μm with a 400 μm diameter hole. The resulting dense material (Raman spectroscopy showed that anatase was completely transformed to α-PbO_2 – structured phase) was placed (unpolished) on the P-wave bench-top buffer rod and a good sample echo was obtained. A P-wave travel time t_P = 10.11(6) ns was measured, but requires a more quantitative density and thickness analysis for interpretation of a bulk elasticity.

Several other samples of nanocrystalline TiO_2 were prepared in a multianvil press using a different grain size powder as a starting material (4 nm, 6-10 nm and 50 nm). For the first sample the density 4.28 (3) g/cm^3 of a resulting material was measured. Several peaces were polished down to about 85 μm and both compressional and shear velocities

were obtained: V_P = 7274 m/s and V_S = 3980 m/s that corresponded to the bulk and shear moduli of K_S = 135.3 GPa and G = 67 GPa.

Next sample for the elasticity measurements was prepared from the 6-10 nm grain size initial material compressed in a multianvil apparatus. A bit less sufficient acoustic echo signal from the polished sample was obtained. And the measured resulting velocities showed the numbers 6142 m/s and 3434 m/s for longitudinal and transverse modes respectively. The effect of grain size on elastic properties seems to be quite strong in the nm-range. The present results along with literature data are given in Table 2-1. The bulk modulus of nanocrystalline phase seems to be much lower, than the same modulus of bulk anatase or other phases of TiO_2.

Table 2-1. Experimentally observed sound velocities and bulk moduli of titanium dioxide.

Phase	V_P, m/s	V_S, m/s	Bulk modulus, GPa	Reference
Nanoanatase, 4 nm grain size	7274	3380	135.3	Present study
Nanoanatase, 6-10 nm grain size	6142	3434	-	Present study
Bulk anatase	-	-	178	Swamy and Dubrovinsky, 2001
			179	Arlt et al., 2000
Baddeleyite-type TiO_2	-	-	303	Swamy et al., 2002
			290	Arlt et al., 2000
Rutile	9240	5160	210.3	Isaak et al., 1998b

The sample compressed from a 50 nm grain size TiO_2 showed no acoustic echo signal probably due to very small wavelength-to-grain size ratio or might be also due to the low quality of the sample.

Nanocrystalline anatase was also tested as a high-pressure sample in a DAC. The ultrasonic signal was good enough but the problem of thickness measurements (while the sample is just squeezed between two diamond culets) was not solved sufficiently good to interpret and analyse the resulting data.

Some other polycrystalline samples were also tested for GHz measurements. Pyrolitic BN was used as a starting material in order to synthesise the cubic phase of boron nitride for further elasticity measurements. X-ray diffraction revealed the 14 nm grain sizes in a probed sample. It was characterized by black colour and semi-transparency, density was determined to be 3.495 g/cm^3. The ambient conditions sound wave velocities were obtained from two peaces of 96 μm thick, and the found values were 15166.9 m/s and 9968.85 m/s for compressional and share waves, respectively (Table 2-2). In this case only ambient pressure experiments were performed, since the sound velocities are too high and even within a thick sample the travel times were only 12-18 ns. When polishing the sample down to the thickness sufficient for the high-pressure experiment, travel time would decrease to 2-3 ns, which is impossible to detect with the equipment used now in the described laboratory.

Table 2-2. Comparison of present results with previous experiments for cBN.

V_P, m/s	V_S, m/s	Bulk modulus, GPa	Reference
15166.9	9968.9	340.9	Present study
		377	Solozhenko et al., 1998

So far the possibility of application the GHz ultrasonic interferometry to the nanocrystalline materials was tested and confirmed. The grain size limitation (grains should be smaller than ~40 nanometres) was revealed for the frequency range up to 2.1 GHz.

The current system is also capable for measuring compressional wave travel time in liquids (which was tested on the liquid phase of argon) but the problem of thickness knowledge does not allow a quantitatively interpretation of the data.

High-P-T in situ measurements

The GHz system in BGI was developed to the high-temperature experiments only recently, and there were performed just the pioneer tests of *in situ* measurements. The sample of MnO was chosen as a testing material. The usual procedure of loading the cell with methanol-ethanol-water mixture as a pressure-transmitting medium was performed. Small ruby spheres were loaded along in order to provide possibility for simultaneous pressure-measurements (Fig. 2.1.7).

The sample of MnO was commercially available from MaTecK Co. The crystals were oriented using x-ray diffraction and several samples were prepared for the ultrasonic measurements. Those for ambient conditions were 250 microns thick and for high-pressure experiments were ~29 μm thick. First the bench-top experiments for both P-and S-wave measurements were performed and the obtained velocities along the [100] crystallographic direction were 6547 m/s and 4093 m/s for longitudinal and transverse waves respectively. These observed numbers allow calculating the individual elastic constants C_{11} and C_{44}, which are presented in Table 2-3 along with literature data for the same material.
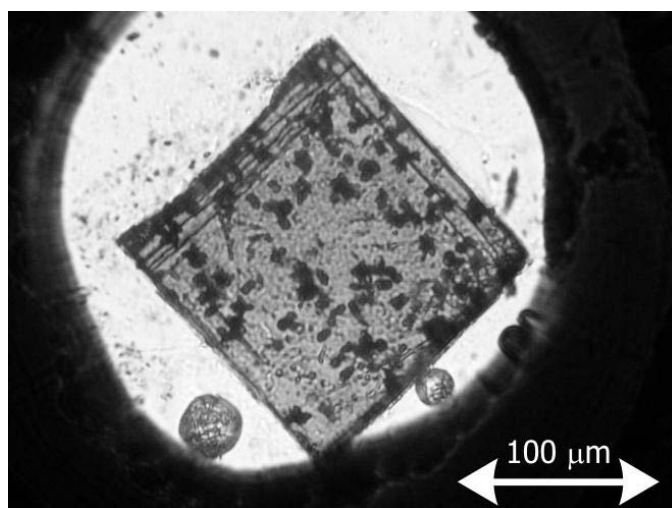
Fig. 2.1.7. MnO single crystal inside a DAC. The black spots within the crystal are the Mn_3O_4 inclusions. The ruby spheres allow pressure measurements upon compression and heating.

Table 2-3. Comparison of present results for MnO with previous experiments at ambient conditions.

C_{11}, GPa	$\left(\partial C_{11}/\partial P\right)_T$ (unitless)	C_{44}, GPa	Reference
229.2(3)	11.3(2)	89.9(5)	Present study
226.4(2)	9.26(9)	79.0(1)	Webb et al., 1988
233	8.54	79.4	Sumino et al., 1980

For the share-wave velocity measurements only the thin piece was used because no acoustic echo was obtained from the thick one due to the strong S-waves attenuation on Mn_3O_4 lameli (see Fig. 2.1.7). These secondary-phase inclusions were also observed in the single-crystal specimen of Webb et al. (1988), who carried out a very thorough and careful analysis using optical microscopy, TEM, XRD and electron diffraction. Their results identified the phase as polycrystalline Mn_3O_4 (hausmannite), which appears to have formed as an exsolutions precipitate during cooling of the single-crystal.

94

After initial bench-top experiments one of the thin pieces was loaded to the DAC equipped with a small Pt-resistive heater in order to perform simultaneous compression and heating experiment. The size of the sample was about 200 μm, small ruby spheres were placed inside a sample chamber in order to measure the pressure (see Fig. 2.1.7). The compressional wave's velocities were measured at several pressures at room temperature, at 50, 100 and 150°C. Figure 2.1.8-A shows the interferometry data recorded at 100°C and 5 GPa from the studied sample in the DAC. The measured travel times usually decrease upon compression at constant temperature (Fig. 2.1.8-B). Six pressure points (from 2.3 to 8.4 GPa) at room temperature showed the usual increase of sound velocities in good agreement with the literature data (Pacalo and Graham, 1991) resulted in $\left(\partial C_{11}/\partial P\right)_T$ value equal to 11.3 (see Table 2-3). At least one more crystal orientation is necessary for both, P- and S-waves, in order to determine the full elastic tensor together with pressure and temperature derivatives of individual elastic constants of MnO.
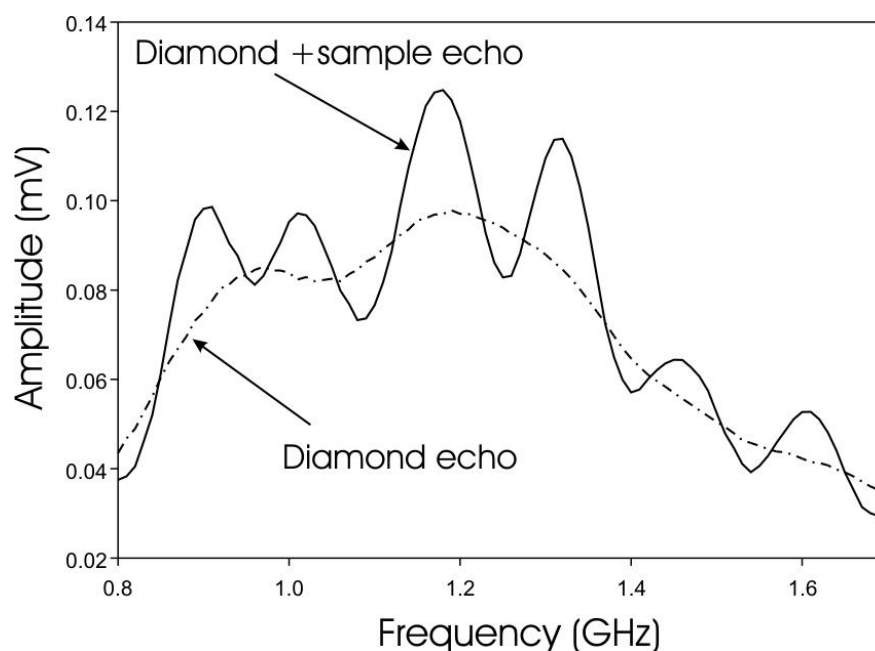
Fig. 2.1.8-A. Compressional-wave interferometry data from a single-crystal of MnO at 5 GPa and 100°C.
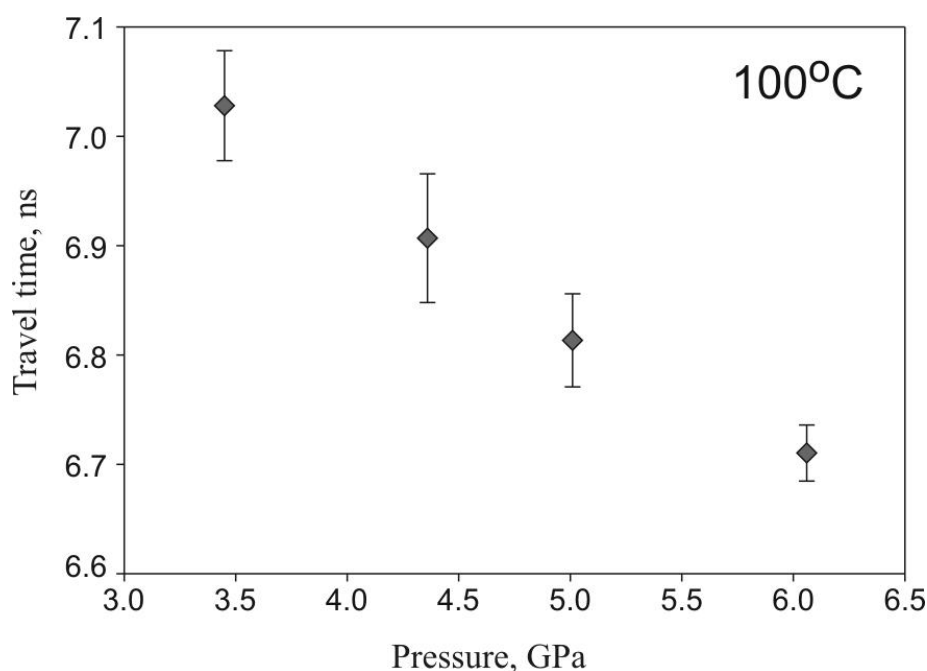
Fig. 2.1.8-B. The P-waves' travel time evaluation in the [100] crystallographic direction of MnO sample with pressure at a temperature of 100°C.

Summary and further developments

So far the developed gigahertz ultrasonic system could be used to get the full elasticity tensor of single-crystals under high pressure and temperature simultaneously. The pressure is limited now only by conservation of the parallel-faced sample inside a DAC. Loading the cell with helium as a pressure-transmitting medium will move the pressure limit and using neon pressure medium allows heating to higher temperatures. With the increasing temperature it was found that the intensity of the acoustic signal decreases. This problem can be potentially solved using additional high-frequency amplifier, which increases the intensity in several times. Additional amplifier also increases noise, and in this case the GHz-system has to use the internal pulse generator.

In order to reach higher pressures its necessary to use thinner samples and hence the shorter wavelengths are required. For the samples size less than about 25 microns, higher frequencies are essential for sound wave velocity measurements.

The elasticity of nanocrystalline and liquid materials could be also measured but the problem of thickness determination should be solved beforehand. Measuring sound velocities in metals, which could be really interesting and challenging task, unfortunately is not possible with the described technique, because mechanical polishing of the metal single crystal to optical quality produces a thin layer of polycrystalline metal on the surface, and the acoustic signal in completely absorbed by the sample and therefore no backscattered echo could be recorded.

The GHz-ultrasonic interferometry technique is promising for many geologically important applications, but is quite complicated for routine usage. High requirements to the sample quality, the complicated assembly (buffer rods and transducers), which is not available commercially and should be prepared "in house" limit the application of GUI system as well as the wide employment of the technique. From this point of view, BGI in the University of Bayreuth is probably one of the best places for the further development and utilization the system, while the transducers, for example, are sputtered at the physics department of the university by K. Müller.

2.2 Inelastic x-ray scattering technique

Inelastic scattering of x-rays from phonons is expected to supply similar information about the dynamics of the observed system as a coherent inelastic neutron scattering. Within the limits of the adiabatic approximation, the electrons are expected to follow the movements of the nuclei instantaneously. Therefore, phonons, i.e. low-

frequency motions of the nuclei, will cause electron charge density variations, which can be directly observed by inelastic x-ray scattering (IXS).

Cross-section and geometry

IXS method of studying elastic properties of solids is based on the interaction between x-rays and acoustic phonons. A general scattering experiment is shown schematically in figure 2.2.1. An incoming photon of well-defined wavevector $\vec{k}_i$, energy E_j and polarization unit vector ε_i is scattered into the solid-angle element $d\Omega$ under the scattering angle 2θ. The scattered beam is completely defined by the new wavevector $\vec{k}_f$, energy E_f and the polarization unit vector ε_f. The scattered intensity is described by the double-differential cross section $d^2\sigma/(d\Omega d\omega_f)$. It is given by the removal rate of particles out of the incident beam as the result of being scattered into a solid angle $d\Omega$ with a frequency range of $d\omega_f$ (Burkel, 2000).
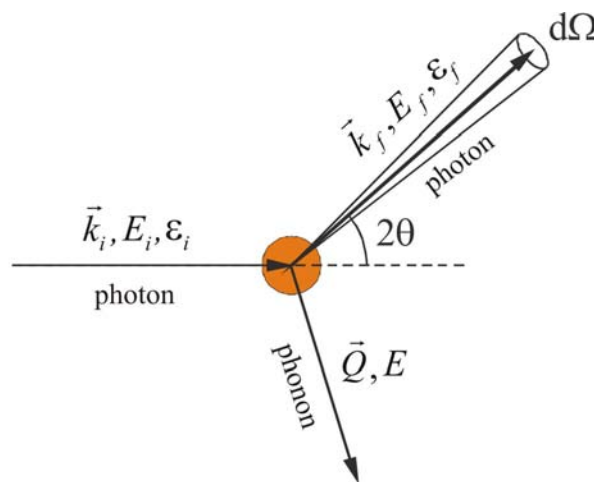
Fig. 2.2.1. The scattering kinematics in IXS experiment.

The scattered beam is usually distributed over a range of energies E_f. There can be beam contributions that have been scattered elastically with no change of energy and other contributions that have changed energy due to inelastic scattering. Therefore, the scattering process contains information on energy and momentum transfers by

$$E \equiv E_f - E_i \quad \text{and} \quad \vec{\hbar Q} \equiv \hbar\left(\vec{k}_f - \vec{k}_i\right) \tag{2.18}$$

Within the scattering of x-rays the transferred energy is normally smaller than the photon energy ($E << E_i$). In this case the momentum transfer $\hbar Q$ is simply connected with the scattering angle θ by

$$\hbar Q = 2\hbar \cdot k_i \cdot \sin\theta \tag{2.19}$$

IXS cross section is proportional to $f(Q)^2 Q^2 \rho/\mu$ where ρ is the specific volume, μ is the absorption coefficient and Q - the wave vector. The optimal signal for DAC experiments is obtained if the absorption length $t = 1/\mu$ is of the order of 10–40 μm, typically spanning elements with Z between 30 and 50. However, previous experiments have shown that studies on lower Z (Occelli et al., 2001) and higher Z materials (Loa et al., 2003) are as well possible.

Elasticity measurements utilizing IXS method are based on sound wave velocity determination along specified directions with a particular polarization vector. In the low-Q part of the Brillouin zone (close to the Γ-point, see Fig. 1.1.2) acoustic phonons dispersion is strictly linear, and sound wave velocity, that is proportional to the $E(Q)$ slope, is independent on wavelength or sampling frequency. For practical applications dispersion curve is obtained from several constant Q energy scans. For each pressure point several directions are measured, and several q for each direction are required for better statistics. An example of the constant Q energy scan is presented in Fig. 2.2.2. It is characterized by an elastic contribution centred at zero energy and two symmetric features, the Stokes and anti-Stokes peaks of acoustic phonons. Each peak has the

different energy positions at different Q-values, which are plotted in a $E(Q)$ diagram. If a single crystal is studied, dispersion can be measured down to low Q (~ 1 nm^{-1}) and fitted as a line to obtain sound velocity.
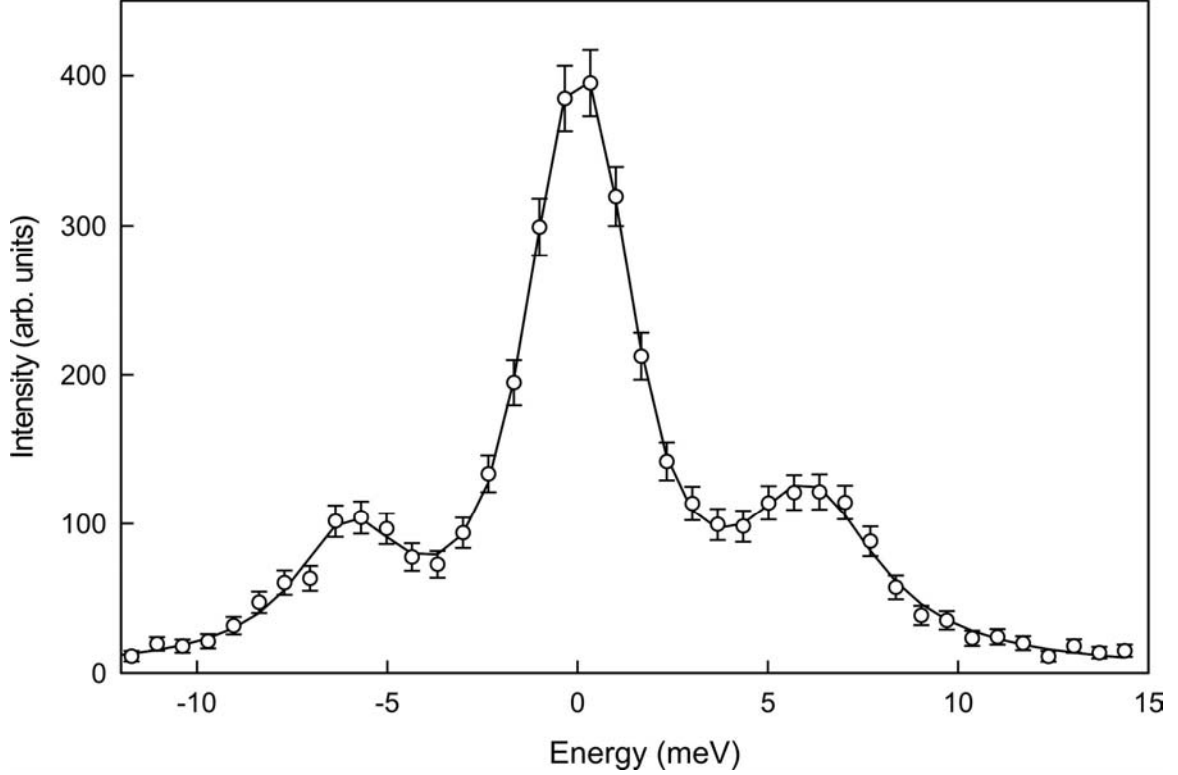

Fig. 2.2.2. An IXS-spectrum from a single crystal of wüstite under 11 GPa and room temperature. Open circles show the experimental points and the solid line represents the fit to the experimental data.

In case of polycrystalline powder overall resolution is lower and elastic peak is usually stronger, that does not allow phonons detection at very low Q-values. Dispersion is then measured to higher Q up to the first Brillouin zone boundary and fitted to non-linear relationship, given by Born-von Karman lattice dynamic theory (Ashcroft and Mermin, 1976). Within the framework of this model the solution of the dynamical matrix can be written as:

$$M\omega^2 = \sum_n \Phi_n \left(1 - \cos\left(\pi \frac{Q}{Q_{max}} \right) \right),$$ (2.20)

100

where M is the atomic mass, ω is the angular frequency and Q is the wave vector of the considered normal mode, Q_{max} is half the distance to the nearest reciprocal lattice point in the direction of Q, and Φ_n is the interplanar force constants (the force between an atom and the nth neighbour plane normal to Q). The shape of acoustic phonon dispersion curve depends on the number of neighbour interactions included in the analysis. For simple monatomic solids it is usually enough to consider only first nearest neighbours interactions. Taking into account only the first term (nearest-neighbours interactions) and substituting $\omega=E/h$ where h is the Plank constant, it can be rewritten as

$$E^2 = \frac{h^2\Phi}{M}\left[1-\cos\left(\pi\frac{Q}{Q_{max}}\right)\right],$$ (2.21)

or, equally

$$E = \sqrt{\frac{2h^2\Phi}{M}}\sin\left(\frac{\pi Q}{2Q_{max}}\right).$$ (2.22)

Taking into account that in long-wavelength limit $V = \frac{2\pi}{h}\frac{\partial E}{\partial Q}$ (with $Q \to 0$), the final result is

$$E = \frac{h}{\pi^2}Q_{max}V\sin\left(\frac{\pi Q}{2Q_{max}}\right),$$ (2.23)

or, equally

$$V = \frac{\pi^2}{h}E\left[Q_{max}\sin\left(\frac{\pi Q}{2Q_{max}}\right)\right]^{-1},$$ (2.24)

where V is the sound wave velocity. Values for V can be consequently derived from the equation 2.24 (Fig. 2.2.3). Q_{max} is the radius of the Brillouin zone. Since Brillouin zone is not spherical, Q_{max} is an averaged radius over multiple directions. It can be calculated using Monte-Carlo method or assuming Brillouin zone to be spherical with volume equal

to its real volume. In all cases Q_{max} values are quite close to each other and do not affect significantly calculated velocity values (Antonangeli et al., 2004). For practical usage it is probably better to leave Q_{max} as a free parameter of the fit.
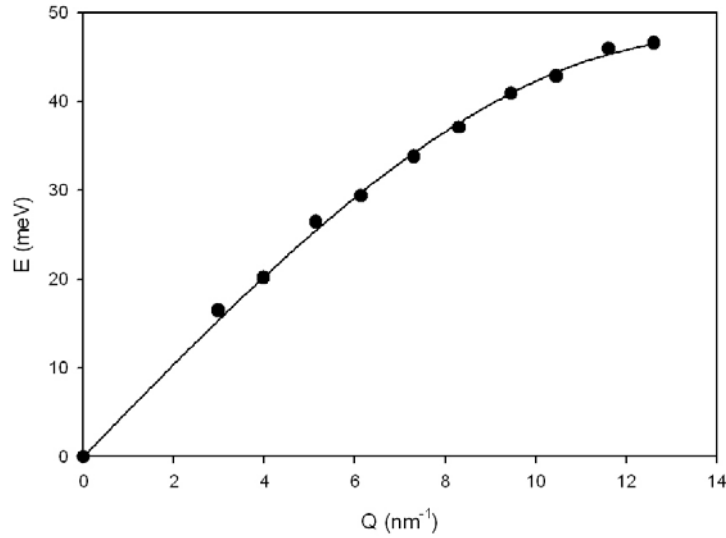

Fig. 2.2.3. A sinusoidal fit to the experimental *E(Q)* relation for FeNi-alloy IXS-spectra collected at 72 GPa and 715 K.

Polycrystals contain a variety of randomly oriented single crystallites. There is no distinct orientational direction as in single crystals and, therefore, the direction of the momentum transfer $\hbar Q$ is not defined. Because of the averaging over the orientations only the absolute value, $|Q| = Q$, is defined. This means that the scattering process takes place on a spherical shell in the reciprocal space and not on a point, as in the case of single crystals. In a polycrystalline material this is only possible in the first Brillouin zone with the reciprocal lattice vector τ equal to 0, which leads to the fact that the momentum transfer $\hbar Q$ equals $\hbar q$ (Burkel, 2000). This shows that only longitudinal (compression) phonon modes are measured within the first Brillouin zone.

Although intrinsic anisotropy of the material could still produce some anisotropy even in an orientationally averaged polycrystalline sample, this effect is probably

negligible, and in many instances one can consider the sample as an isotropic polycrystalline material. In this case, the measured V_P is the bulk longitudinal sound velocity, and the transverse (shear) sound velocity V_S can be obtained according to the relation:

$$V_S^2 = \frac{3}{4}\left(V_P^2 - \frac{K}{\rho}\right),$$
(2.25)

where ρ is the density and K is the adiabatic bulk modulus. As seen from above the knowledge of density and bulk modulus is required.

At present, there are four instruments for IXS-measurements operational at third-generation synchrotron radiation centres (two at ESRF (France), one at APS (USA), and one at SPring-8 (Japan)).

The optical layout at an ID-28 at ESRF, where several experiments of the present work were performed, is shown in figures 2.2.4 and 2.2.5. The photon source is an undulator providing a highly collimated beam. After pre-monochromatization to $\Delta E/E = 2 \times 10^{-4}$ by a silicon (111) double crystal, the photon beam impinges on the backscattering silicon crystal, which is operated at a Bragg angle, θ_B, of 89.98°, and diffracting in the vertical plane. A specific Si (*hhh*) backscattering reflection of the main monochromator is chosen by tuning the premonochromator to the correct energy. This x-ray beam with meV energy resolution impinges on a gold-coated toroidal mirror, which provides a focal size of 250×60 μm^2 H × V (FWHM) at the sample position. For high-pressure studies, where much smaller horizontal beam sizes are generally needed, the focusing optics have been upgraded recently (Krisch et al., 1997). By using the cylindrical side part of the mirror and a horizontally focusing multilayer with a lattice spacing gradient, located at 2 m from the sample, a spot size of 25×60 μm^2 H × V (FWHM) can be achieved.
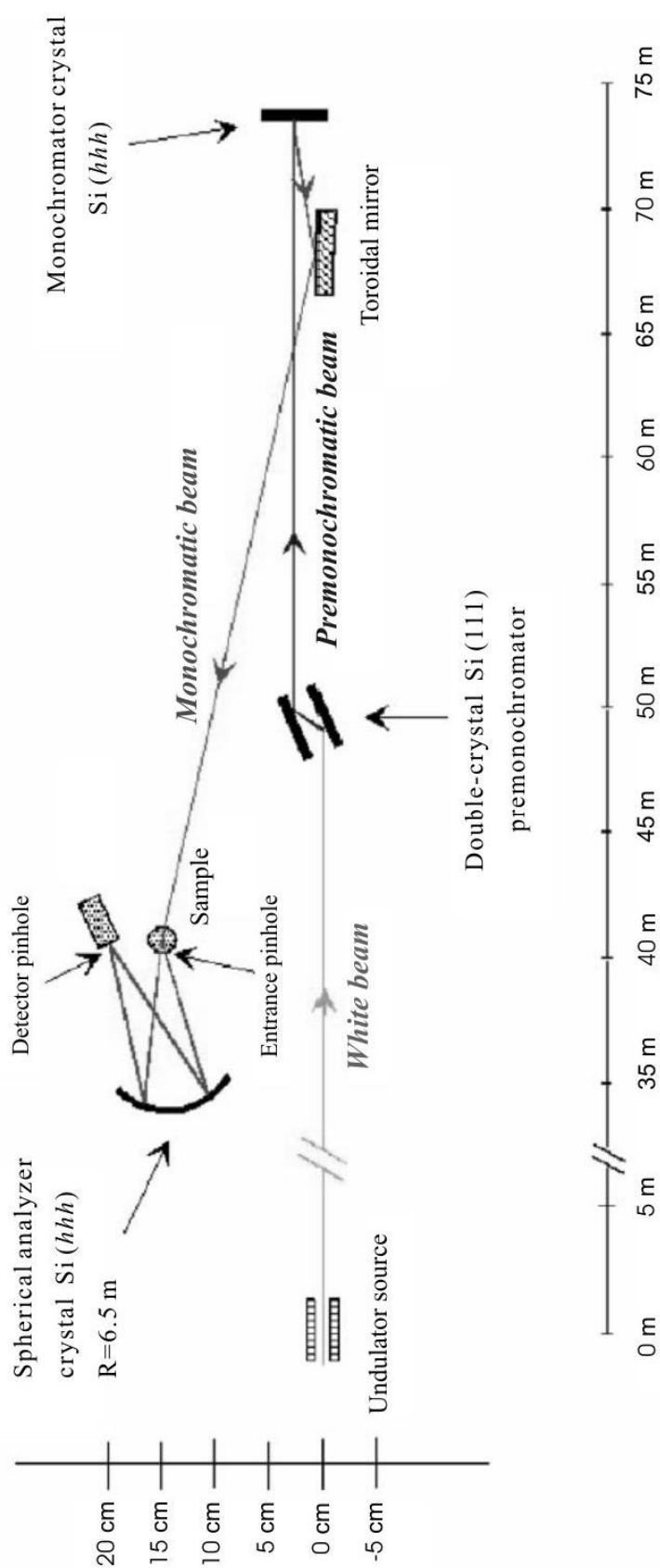
Fig. 2.2.4. Optical layout of ID28 beamline at ESRF (European Synchrotron Radiation Facility, Grenoble, France) (after Fiquet et al., 2004).
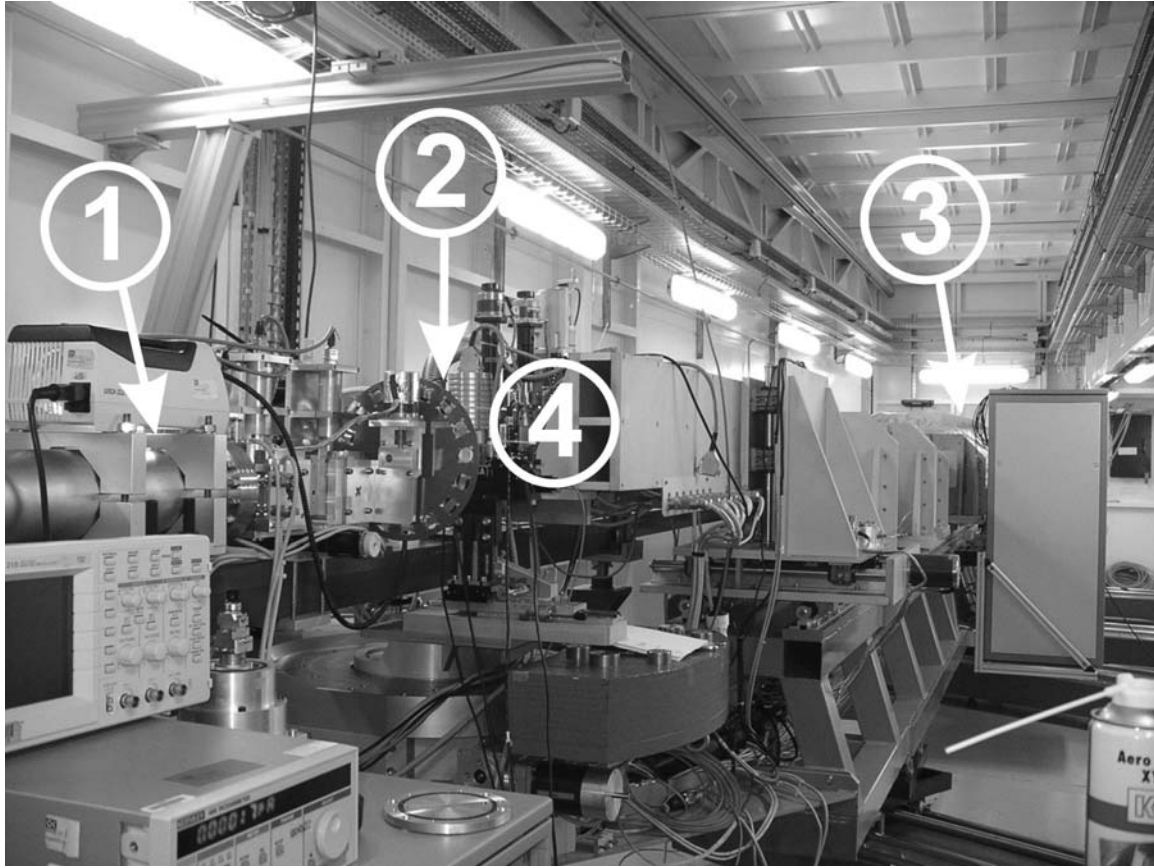
Fig. 2.2.5. Photograph of the experimental layout at ID28 (ESRF). 1 – The tube, from which monochromatic beam comes out; 2 – position of the sample; 3 – position of the analyzer; and 4 – detector.

The photons scattered from the sample are energy-analyzed by a spherical perfect silicon crystal analyzer, operated in Rowland geometry, and at the same *(hhh)* reflection order as the monochromator and a Bragg angle of 89.98°. The momentum vector, *Q*, is selected by rotating the analyzer arm in the horizontal plane. Diffracted from the analyzer crystal x-rays are recorded by a Peltier-cooled silicon diode. Inelastic x-ray scans are typically performed in a constant-*Q* mode by keeping the analyzer temperature fixed, and scanning the temperature of the monochromator. In fact a relative change of the monochromator temperature, ΔT, induces a relative variation in the lattice constant and, according to Bragg's law, at a fixed Bragg angle, a relative energy variation $\Delta E / E = -\Delta d / d$. Considering that $\Delta d/d = \alpha \Delta T$, with the thermal expansion coefficient α

= 2.58 × 10^{-6} K^{-1} for silicon at room temperature (Krisch, 2003), in order to obtain an energy step of about one tenth of energy resolution ($\Delta E/E \sim 10^{-9}$), it is necessary to control the monochromator and analyser crystal's temperature with a precision of mK.
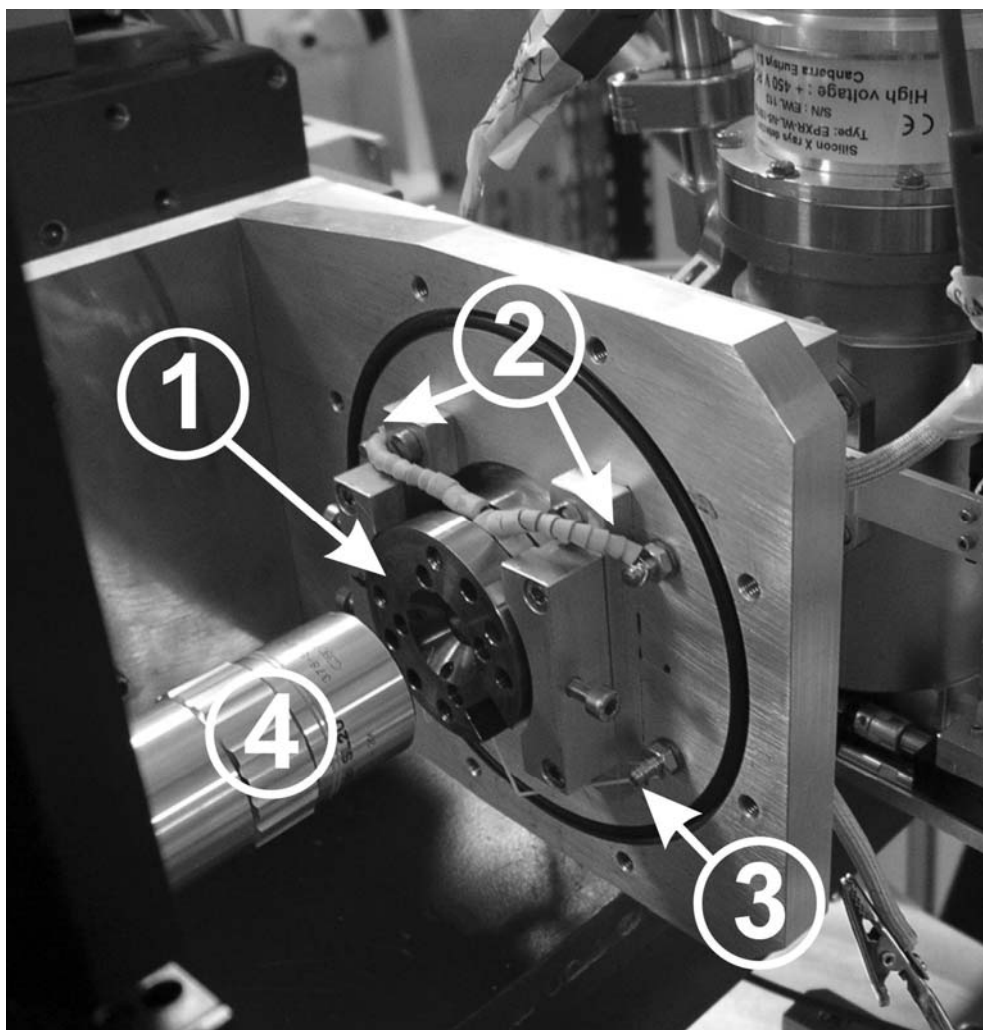

Fig. 2.2.6. The DAC with internal resistive heater (1). 2 – The heater-wires connection; 3 – thermocouple connection; and 4 – the microscope objective used for the ruby fluorescence detection.

Last decade the technique was developed to measure IXS from a sample under high pressures (Krisch et al., 1997). One of the topics of present study was to investigate the elasticity of Fe-Ni alloy under high pressure and temperature. In order to perform such measurements the inelastic x-ray scattering ID28 at ESRF was adapted

for heating in a diamond anvil cell. The four-pin modified Merrill-Bassett DAC equipped with the internal resistive heater was used (Fig. 2.2.6). When a polycrystalline sample is studied, a diamond anvil cell should be placed in the vacuum chamber in order to reduce additional x-ray scattering from the air. The standard vacuum chamber was adopted in order to provide electrical connectors for resistive heater and thermocouple (Fig. 2.2.7). The DAC heating assembly developed at Bayerisches Geoinstitut allow maintaining temperatures as high as 1000 K for several days, allowing performing many time-consuming experiments (including IXS) under high pressures and high temperatures.
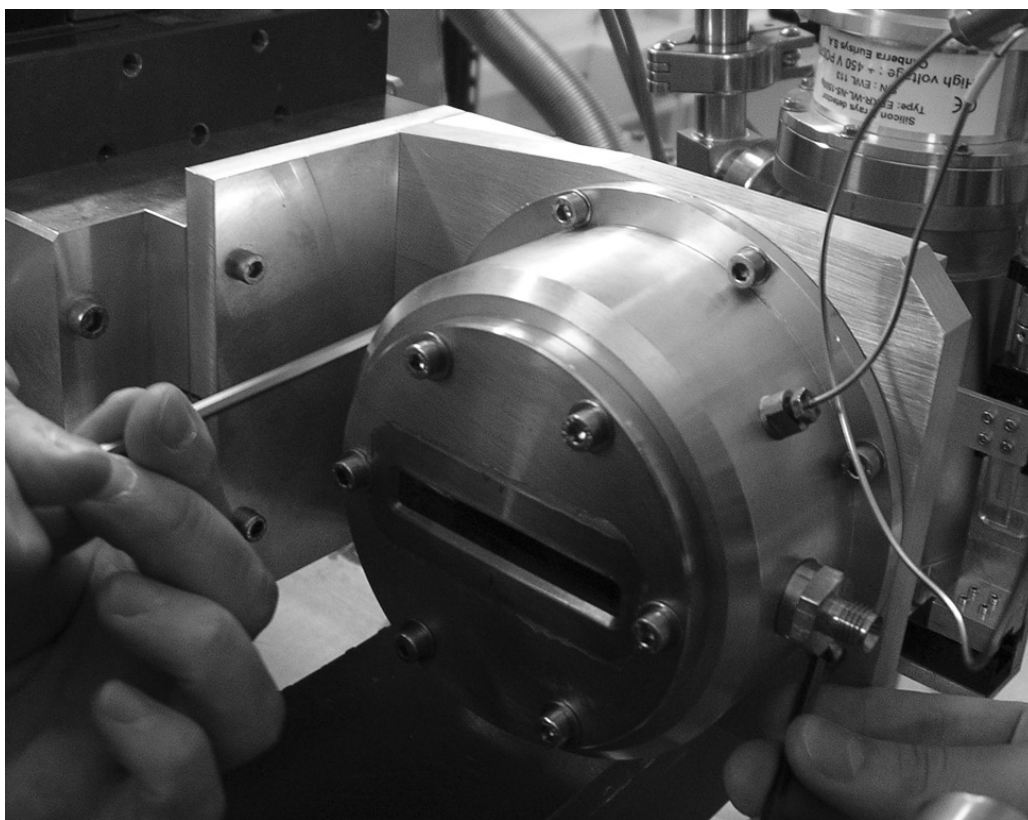
Fig. 2.2.7. View of a special-designed vacuum chamber with a DAC (inside) for IXS measurements at high-*P, T* at ID28.

Chapter 3

Results and discussion

3.1 Elasticity and magnetization in wüstite: High-frequency interferometry measurements, neutron diffraction study, and inelastic x-ray scattering experiments

Wüstite is an iron monoxide with nominal FeO composition. However, despite its apparent simplicity, FeO is a complex material, because wüstite is never "ideal" at room temperature and pressure, but rather it is non-stoichiometric with cation deficiencies. As a result it should be described by the formula Fe_xO where x is variable down to 0.88 (hereafter Fe_xO is designated FeO in this chapter). Wüstite has long been of interest on account particularly of its very wide range of non-stoichiometry and its antiferromagnetic behaviour at certain conditions. Later the importance of magnesiowüstite $(Mg,Fe)_xO$ as a mineral phase in the Earth's lower mantle and indications of substantial oxygen solubility in the Earth's liquid outer core have focused attention on the high-pressure behaviour of wüstite. Ringwood (1977) proposed a compositional model of the Earth's core in which FeO was the major light

component. This makes FeO possibly the only common major component of both the metallic core and the oxide mantle. Studies of the phase transitions, oxidation-reduction, disproportionation and metallization of wüstite are thus central to understanding core formation, core-mantle interaction, and inner-core solidification (Dubretsev and Pankov, 1972; Bullen, 1973; Mao, 1974; Stevenson, 1981).

Moreover the iron monoxide is an important member of the highly correlated transition metal monoxide group including NiO, CoO, and MnO that raise a continuous interest due to their complex structural, electronic and magnetic properties.

Under ambient conditions, wüstite has the NaCl (B1)-type structure. At low temperature near 90 K the FeO x-ray diffraction pattern shows a small degree of trigonal distortion (Willis and Rooksby, 1953). At room temperature a departure from cubic symmetry at pressures from 9 to 24 GPa was reported (Zou et al., 1980; Jacobsen et al., 2005b). The transition pressure depends on the composition of FeO and also on the certain experiment conditions.

A magnetic ordering (Néel) transition at ambient pressure in FeO was observed around 195 K, and structural distortion was assumed to be a magnetostriction effect, similar to MnO, CoO and NiO (Smart and Greenwald, 1951). In high-pressure Mössbauer experiments (Nasu, 1994; Pasternak et al., 1997) the Néel transition was also recorded, but the exact transition pressure at room temperature was not known so far. The value of the Néel temperature varies also with Fe_xO composition (McCammon, 1992). Many physical properties of FeO are significantly influenced by its defect structure. Several systematic studies of this compound show, for example, that the lattice parameter varies linearly as a function of x in the Fe_xO formula (Simons, 1980; McCammon and Liu, 1984).

The elastic properties of wüstite are also dependent on its defect concentration or stoichiometry, and this dependence seems to be non monotonous (Zhang, 2000; McCammon, 1993). This variation has generally not been well understood by either experiments or theories. Data on bulk modulus and its pressure derivative from different studies are strongly scattered, however. The behaviour of the pressure (or temperature) derivatives of individual elastic constants is also not simple. The individual C_{44} elastic constant softens upon increasing pressure (or decreasing temperature) up to (down to) the structure transition (Sumino et al., 1980).

The studies of elasticity and its possible correlation with magnetization and structure transition of FeO are presented in this chapter.

3.1.1 Elasticity measurements: Ultrasonic interferometry data

The study of elastic properties of the material at room temperature and pressures up to 9.6 GPa was carried out using a gigahertz ultrasonic interferometry technique for the DAC. Details of acoustic interferometry and data reduction are given in the previous chapter.

A single crystal of FeO was synthesized by the floating zone technique (Berthon et al., 1979), with measured cell parameter of a =4.3068(1) Å, corresponding to the $Fe_{0.943}O$ composition (McCammon and Liu, 1984). The sample was cut to several peaces each of which was oriented along the certain crystallographic direction using the single crystal x-ray diffraction technique. After initial bench-top experiments (Jacobsen et al., 2002a) with FeO crystals oriented parallel to [100] and [111] directions, the samples were polished to thin plates measuring about 40 μm in thickness for high-pressure work. A series of experiments was performed. Every next

time the sample of certain orientation measuring about 200 μm in diameter was placed into the pre-indented hole of a T301 steel gasket, and compressed between 0.5 mm culet diamond anvils in a Merrill-Bassett style DAC (Jayaraman, 1983). All the samples were compressed using a 16:3:1 methanol:ethanol:water mixture as a pressure transmitting medium, along with some amount of silica aerogel in order to press the sample against one of the diamond anvils. Several ruby spheres were loaded in the sample chamber for pressure measurements (Mao et al., 1986) (Fig. 3.1.1). The uncertainty was 0.1 GPa at the highest pressure reached in this study (9.6 GPa).
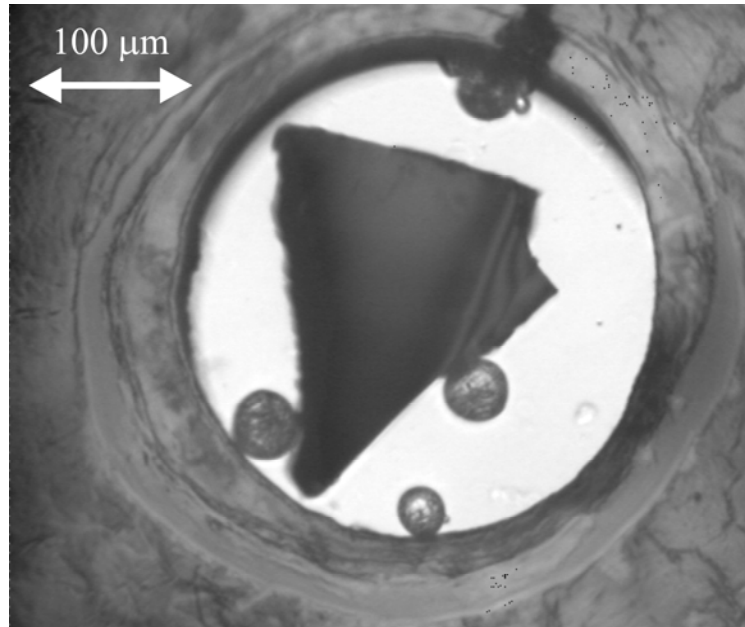

Fig. 3.1.1. The sample of $Fe_{0.94}O$ and the ruby spheres inside a diamond anvil cell.

Measured single-crystal travel time data t_P<100>, t_S<100>, and t_S<111> were converted to sound wave velocity using the calculated sample thickness, determined initially from bench-top velocities measurements (Jacobsen et al., 2002a). The measured thickness usually has 0.001 mm uncertainty, which is about 2% for DAC-samples, while only about 0.3% for bench-top samples (measuring several hundreds

of microns in thickness). Hence, sound wave velocities measured at ambient conditions (in thick samples) are usually taken as a reference for further high-pressure and temperature experiments. An isothermal equation of state for FeO (Jackson et al., 1990) was used to calculate the change in sample length with pressure. The complete elastic tensor was obtained using the pure-mode solutions to the Christoffel equations (Eqs. 2.5-2.8) and is plotted in figure 3.1.2-A and B along with the isotropic adiabatic bulk (K_S) and shear (G) moduli.

A change in pressure-dependence slope was observed for both C_{11} and C_{12} elastic constants at 4.7 ± 0.2 GPa (see Fig. 3.1.2-A and B, Table 3.1). The reversibility of the anomaly was tested and confirmed by measuring t_P<100> on both compression and decompression. The unusual behaviour of the slope is also clear in the variation of isotropic modulus (Fig. 3.1.2-A). Both moduli were calculated using the linear fits to the individual elastic constant experimental data.
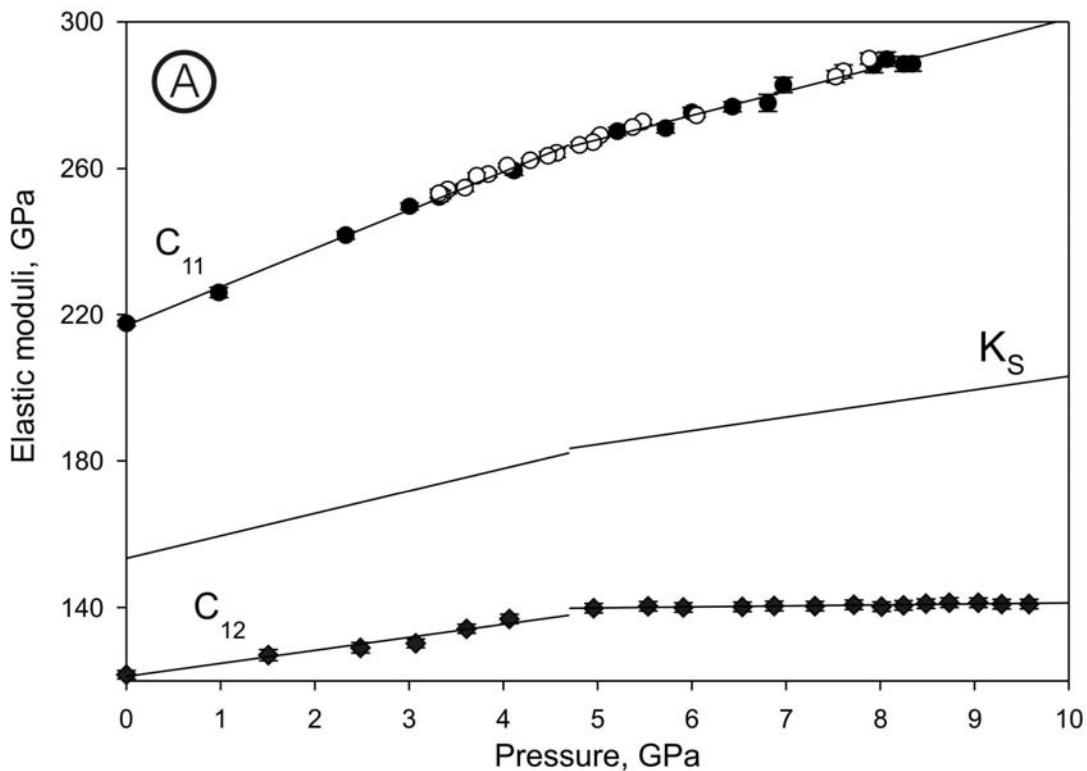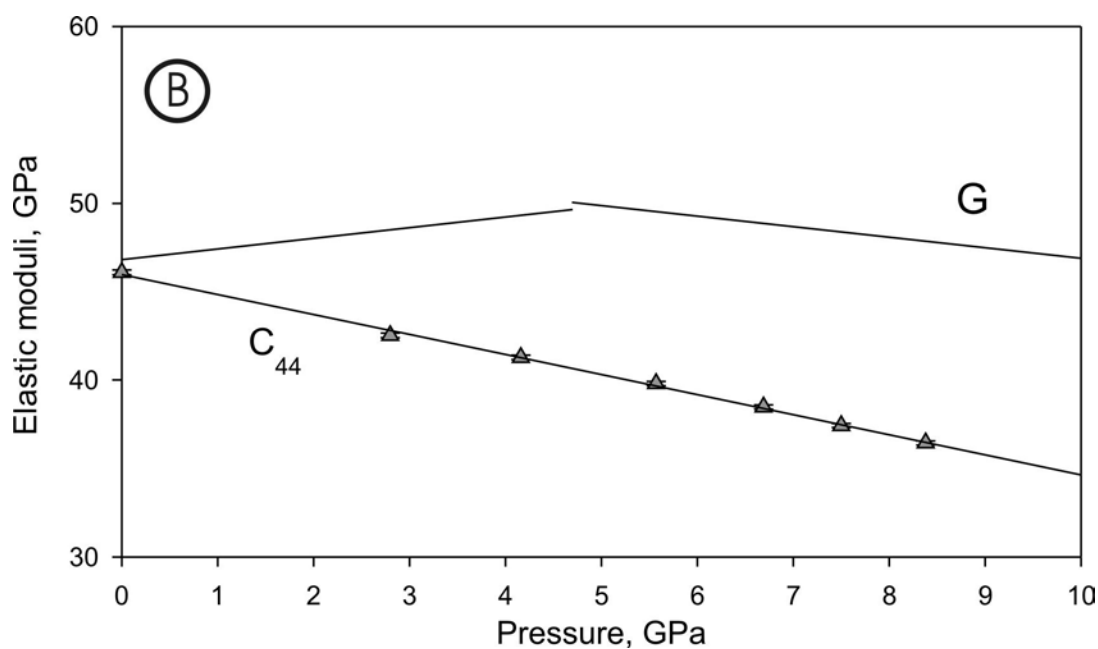
Fig. 3.1.2-A, B. The elastic tensor and isotropic adiabatic moduli for Fe$_{0.94}$O. Filled and open circles for C_{11} elastic constant indicate points measured on compression and decompression, respectively. Lines are linear fits to the data (see Table 3-1).

Table 3-1. Coefficients of the linear fits to the elastic moduli of Fe$_{0.94}$O to the equation $A + B \times P$ (GPa).

Modulus and pressure range		A	B
C_{11}	$P < 4.7$ GPa	217 ± 1	10.5 ± 0.3
	$4.7 < P < 10$ GPa	234.9 ± 0.5	6.6 ± 0.2
C_{12}	$P < 4.7$ GPa	121 ± 1	3.5 ± 0.7
	$4.7 < P < 10$ GPa	138.4 ± 0.5	0.27 ± 0.7
C_{44}	$0 < P < 10$ GPa	45.9 ± 0.7	-1.13 ± 0.03
K_S	$P < 4.7$ GPa	153 ± 1	6.1 ± 0.4
	$4.7 < P < 10$ GPa	165 ± 1	3.7 ± 0.3
G	$P < 4.7$ GPa	46.8 ± 0.4	0.6 ± 0.1
	$4.7 < P < 10$ GPa	49 ± 1	-0.22 ± 0.03

The reason for this discontinuity is suggested by the results of high-pressure Mössbauer spectroscopic (MS) studies (Kantor et al., 2004b). At a pressure of 5.0 ± 0.5 GPa the beginning of magnetic ordering in polycrystalline ^{57}Fe-enriched $Fe_{0.95}O$ compressed in a methanol:ethanol hydrostatic pressure-transmitting medium was observed. The results of this work show that the magnetic phase boundary between anti-ferromagnetic and paramagnetic phases does not coincide with the reported location of the structural phase boundary between cubic and rhombohedral phases of FeO, and that they differ from each other by at least 10 GPa at room temperature. In the event that the structural and magnetic phase boundaries do not in fact coincide, this raises an important question regarding magnetic ordering in the cubic structure. The remarkable coincidence in transition pressures suggests that magnetic ordering in FeO is manifested in changes of elastic properties detected by the high-precision ultrasonic data.

The above shown data indicate the existence of a new cubic magnetically ordered phase of FeO at pressures higher than 5.0 ± 0.5 GPa and up to the structural transition. The Mössbauer spectra of different phases of FeO should be different.

In order to see it the MS studies of the same sample were carried out using the same methodology as described previously (Kantor et al., 2004b) but with argon as a pressure-transmitting medium and up to higher pressures. It was found that Mössbauer spectra of the cubic and the rhombohedral magnetic phases differ in some ways (Fig. 3.1.3). Mössbauer spectrum at 11.1 GPa consists of two main components: a broad magnetic part with unresolved lines and a "paramagnetic" doublet, which persists up to the structural phase transformation at ~17 GPa (Mao et al., 1996). Mössbauer spectrum of the rhombohedral phase at 23.8 GPa consists only of a

relatively well-resolved sextet. These results also support the idea of the existence of cubic magnetic phase of studied FeO.
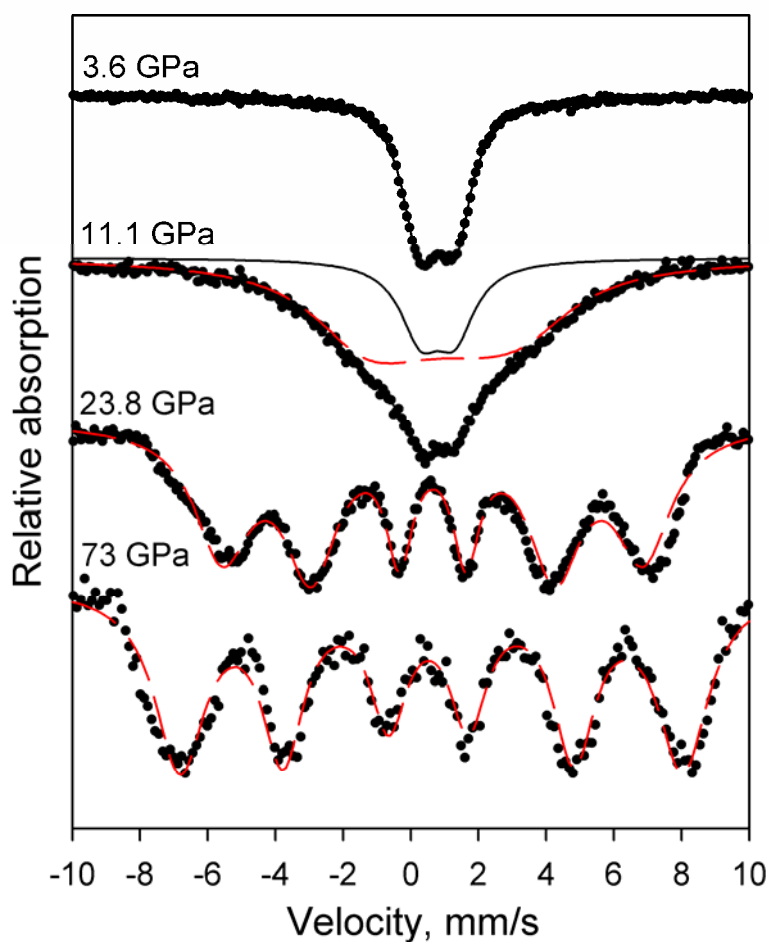

Fig. 3.1.3. Selected Mössbauer spectra of $Fe_{0.95}O$ wüstite at different pressures: 3.6 GPa – paramagnetic cubic phase; 11.1 GPa – magnetically ordered cubic phase with a paramagnetic doublet (solid line) and broad magnetic component (dashed line); 23.8 and 73 GPa – antiferromagnetic rhombohedral phase with a resolved magnetic sextet (dashed line).

3.1.2 Elasticity of FeO up to 20 GPa: Inelastic x-ray scattering measurements

In order to complete the elasticity data of the cubic phase of wüstite the further investigations were performed using inelastic x-ray scattering technique up to 20 GPa at room temperature. The series of experiments were carried out at ID28, European Synchrotron Radiation Facility in Grenoble.

The single crystal of wüstite was synthesized by the floating zone technique (Berthon et al., 1979), with measured cell parameter of $a = 4.3093(2)$ Å, corresponding to the $Fe_{0.948}O$ composition (McCammon and Liu, 1984). Using x-ray diffraction the single crystal was oriented along the [110] crystallographic direction and polished down to 29 microns. The oriented sample measuring about 100 microns in diameter was placed into the preindented hole of rhenium gasket, and compressed between 0.4 mm culet diamond anvils. The DAC was loaded with helium as a pressure-transmitting medium along with a few ruby spheres. Pressure was measured using the ruby fluorescence scale (Mao et al., 1986).

Simple rotation of the cell around the incident beam direction allowed access to the longitudinal acoustic (LA) phonon branches along the [001] and [110] directions, and the transverse acoustic (TA) branches along the [111] and the [100] directions. In Fig. 3.1.4 the example of the collected IXS spectra is reported. It is characterized by an elastic contribution centred at zero energy and two symmetric features, the Stokes and anti-Stokes peaks of the FeO acoustic phonons. Typically, three to five IXS spectra were recorded in the low q part of the acoustic phonon branch, and the sound velocity was determined by a linear fit to the $E(q)$ values with an error of 1%–2% (Fig. 3.1.4, inset).

The corresponding sound velocities were determined from the linear part of the acoustic phonon branch, and the three independent elastic moduli were then derived using the Christoffel equations (Eqs. 2.5-2.9).
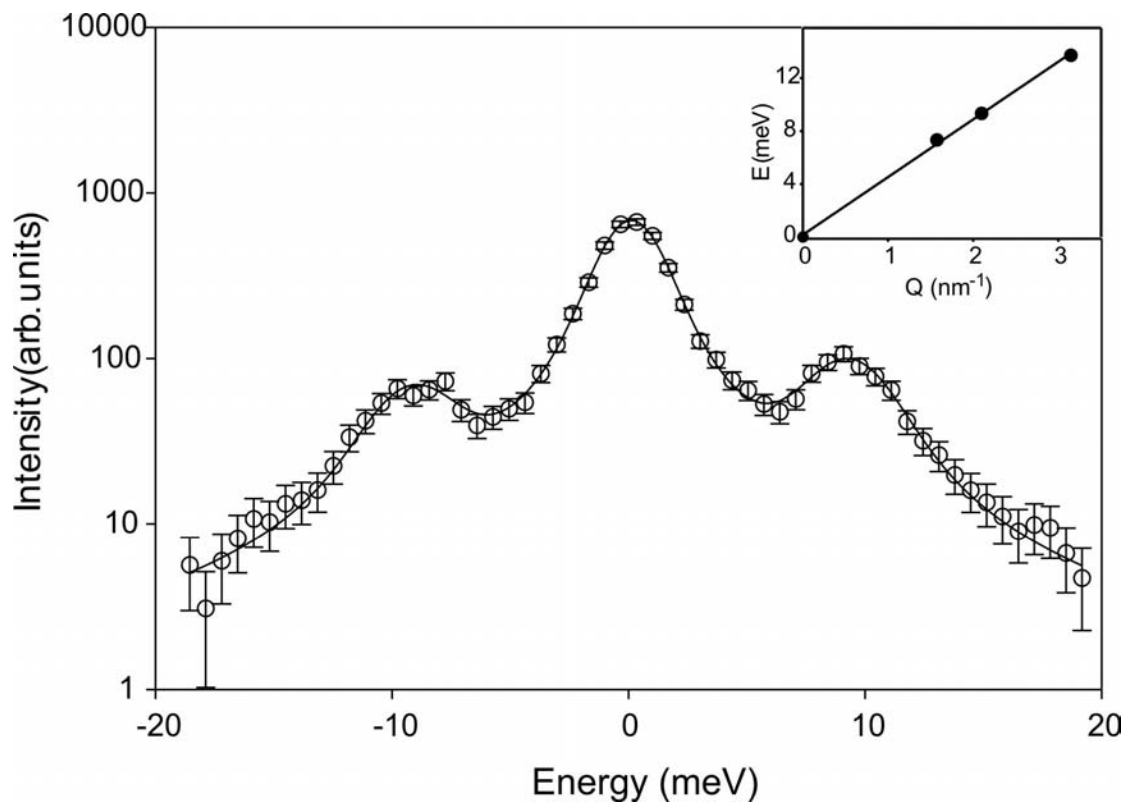

Fig. 3.1.4. A representative IXS spectrum of $Fe_{0.95}O$ single crystal recorded at 9.2 GPa and a reduced momentum transfer value $q = 2.1$ nm^{-1}. Inset: example of the linear fit to the experimental $E(q)$ relation with one adjusted parameter. Only the low-Q part of the first Brillouin zone shown, which extends up to approximately 16 nm^{-1}.

The pressure evaluation of three independent elastic constants is plotted in Fig. 3.1.5. It is clear that the negative slope of the C_{44} elastic constant persists up to the transition pressure point, and C_{44} rapidly increases above cubic-to-trigonal transition pressure. Two other constants continue smoothly increasing without any drastic anomalies in the whole investigated pressure range.
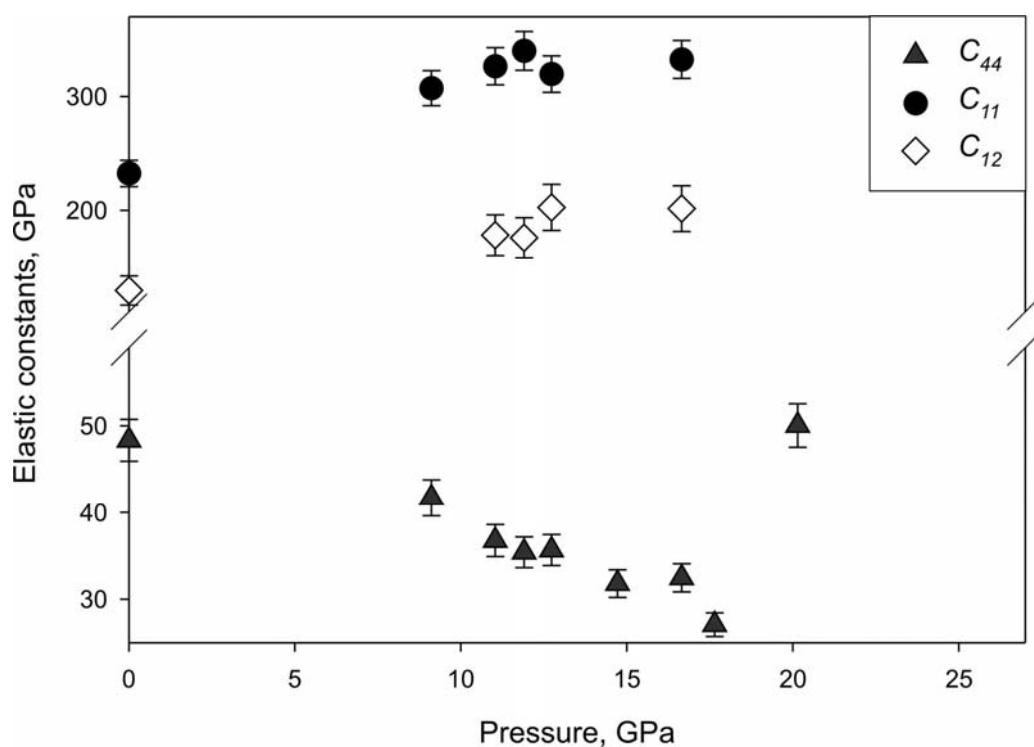
Fig. 3.1.5. Pressure evaluation of individual elastic constants of Fe$_{0.95}$O measured by IXS.
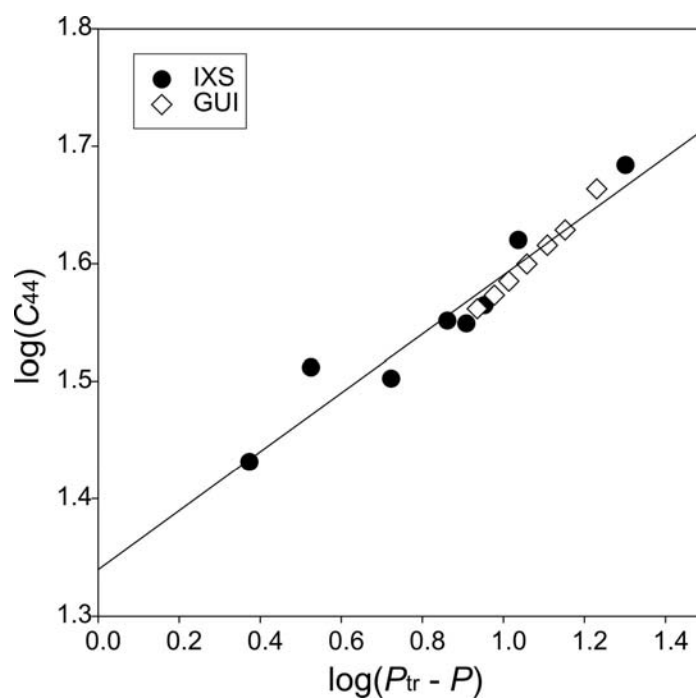

Fig. 3.1.6. Pressure-induced C_{44} mode softening in FeO at room temperature. Linear relation between log(P_{tr}-P), where P_{tr} is the transition pressure and log(C_{44}) exists.

Table 3-2. Experimental values for volume (x-ray diffraction measurements), pressure (determined using ruby fluorescence pressure scale), and adiabatic elastic moduli (IXS measurement) of $Fe_{0.95}O$.

$P*$ (GPa)	V (Å³ per unit cell)	C_{11} (GPa)	C_{12} (GPa)	C_{44} (GPa)
0.001[§]	80.02(3)	232(3)	129(4)	48.3(6)
9.12(5)	76.03(4)	307(4)	n.a.	41.7(6)
11.03(5)	75.18(5)	326(4)	178(5)	36.7(5)
11.90(5)	74.74(5)	340(4)	176(5)	35.4(6)
12.73(5)	74.45(4)	320(4)	203(6)	35.6(7)
14.72(5)	73.68(6)	n.a.	n.a.	31.8(6)
16.65(5)	73.10(4)	332(4)	202(5)	32.5(8)
17.64(5)	72.69(5)	n.a	n.a	27(1)

[§] – measured outside the diamond anvil cell

n.a. – value was not measured

Elastic mode softening in the vicinity of distortional structural transition is a quite common behaviour. Significant decrease of some of elastic constants reveals dynamical instability of a crystal lattice. Usually in the vicinity of a transition the soft modes decrease exponentially, and a linear relation between $\log(C_{ij})$ and $\log(T_{tr}-T)$ or $\log(P_{tr}-P)$ for temperature- and pressure-induced transitions exists (Ohno et al., 2006), where T_{tr} and P_{tr} are temperature and pressure of the transition respectively. In case of FeO this relation is also valid (Fig. 3.1.6). C_{44} elastic mode softening in FeO was also observed by mean of neutron inelastic scattering up to 12 GPa (Klotz, 2001). The fact that the mode's softening was observed in the whole Brillouin zone and not just near Γ-point allows concluding that this softening reflects lattice dynamics instability rather than anomalous magneto-elastic coupling. In parallel to the IXS spectra, the

Bragg angles of the (002) and (220) reflections were recorded, in order to provide an independent determination of volume and density for each pressure point. Table 3-2 summarizes the experimental results of this study.

3.1.3   Relation between structural and magnetic transitions in FeO: Neutron diffraction data

The *fcc*-based antiferromagnetic structures are among the most difficult structures to treat theoretically: at least two exchange parameters are required to describe their magnetic interactions. The molecular-field theory predictions (Brillouin function) agrees poor with the experimental magnetization curves, and it was shown that either biquadratic exchange interactions (Rodbell et al., 1963) or corrections for lattice distortion (Lines, 1965) should be included into the model, suggesting the influence of lattice distortion on magnetization. The random phase Green's-function theory defines lattice distortion in type II *fcc* antiferromagnets to be the function of elastic constants, and spin distribution (in other words, magnetization) (Morosin, 1970).

All theoretical approaches used so far assume not only strong magneto-elastic coupling, but also coincidence of these two transitions (Struzhkin et al., 2001) for all transition metal monoxides (TMM). As is shown in sections 3.1.1 and 3.1.2, in FeO at high pressures and room temperature these two transitions are decoupled. In order to verify if these transitions coincide at low temperatures and whether these relations are similar for different TMMs or they are unique FeO feature, a low-temperature neutron diffraction study of FeO and MnO was performed.

For MnO at ambient pressure the Néel transition and structural distortion occurs probably at the same temperature (~118 K), although there is no simultaneous study of magnetic and structural properties of the same MnO sample. For FeO, the Néel temperature varies with the composition from 192 to 209 K (McCammon, 1992; Seehra and Srinivasan, 1984), and no systematic study of FeO crystal structure changing at low temperature was ever held before. High-resolution neutron diffraction is probably the best method for determination of magneto-structural correlation since one diffraction pattern contains both structural and magnetic reflections, providing information about crystallographic structure and magnetic properties simultaneously.

Such experiments were performed on the powder samples of FeO and MnO. Manganese oxide was chosen as a structural analogue of FeO with the same type of the magnetic structure.

FeO powder sample was synthesized from a metallic iron in a CO/CO_2 gas-flowing furnace with the controlled oxygen fugacity. After treating for 24 hours at 900°C and log (fO_2) = -11.5 the sample was quenched in water. Measured cell parameter of FeO was 4.296(2) Å, corresponding to $Fe_{0.92}O$ composition (McCammon and Liu, 1984). MnO powder sample of 99.99% purity was pursed from "ALFA products". Room temperature lattice parameter a of MnO was measured by powder x-ray diffraction to be 4.4455(4) Å. Both samples were carefully grained in an agate mill, and x-ray powder diffraction analysis confirmed single-phase composition of both samples. About 150 mg of each powder samples were loaded into vanadium capsules and placed in a liquid He cryostat for neutron diffraction measurements.

Powder neutron diffraction studies were performed on G6-1 cold neutron two-axis diffractometer in Laboratoire Lèon Brillouin, Saclay, France. A monochromatic neutron beam was selected by a graphite monochromator with initial wavelength of

4.741 Å. The diffractometer was equipped with a linear 400-cells BF_3 multidetector. Diffraction patterns were collected in 2Θ range of 45 – 145 degrees with a 0.1-degree step. Diffraction peaks characteristics (positions, FWHM and integrated intensity) were extracted for each peak individually using a PeakFit software package assuming linear local background.

MnO neutron diffraction data

Collected MnO neutron diffraction patterns above the Néel transition contain only one structural reflection 111. Below magnetic ordering transition two new magnetic reflections appeared (Fig. 3.1.7), which were previously indexed as 1/2 1/2 1/2 and -3/2 1/2 1/2 (Shull et al., 1951). Fractional indexes are used for magnetic reflections because magnetic cell is twice the "chemical" unit cell along all three edges. Hence, the chemical high-temperature 111 reflection is transformed to the 222 reflection in the magnetic unit cell. To avoid confusion here the "chemical" reflections indexes and unit cell are kept, and the fractional indexes for magnetic reflections are used. Due to rhombohedral distortion of cubic lattice at low temperatures, the structural 111 reflection splits into two: -111 and 111, as is shown in Fig. 3.1.7. The degree of such splitting characterizes lattice distortion. In fact, magnetic reflections should also be splitted into two (for 1/2 1/2 1/2) or three (for 3/2 1/2 1/2). Reflection 1/2 1/2 1/2 splits to 1/2 1/2 1/2 and -1/2 1/2 1/2, but the latter one is not allowed by symmetry (Shaked et al., 1988). Similarly, only -3/2 1/2 1/2 reflection is observed at ~122 degrees 2 Θ.
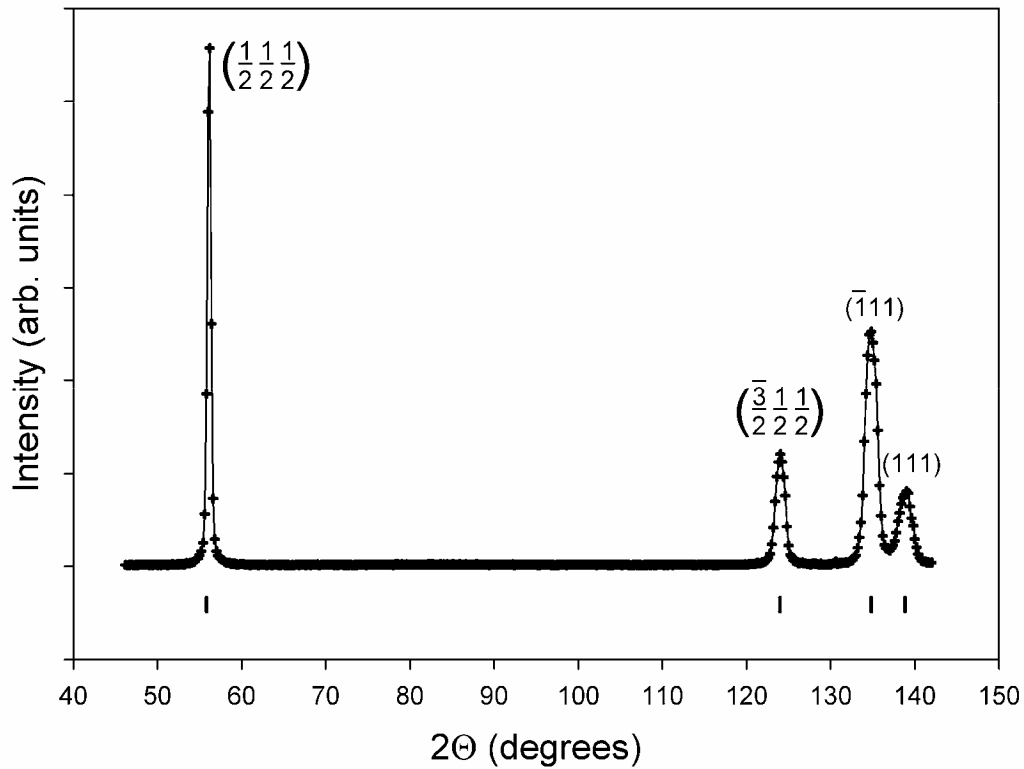
Fig. 3.1.7. Neutron diffraction pattern of MnO at 1.5 K. Ticks show the calculated reflection positions.

Fig. 3.1.8 shows temperature variation of the lattice parameter a and angle α of the pseudo-cubic cell, calculated from two structural reflections 111 and -111. The data are in good agreement with previous x-ray diffraction study results (Morosin, 1970) (Fig. 3.1.8). Integrated intensity of a magnetic reflection is proportional to the square of spontaneous sublattice magnetization $(M/M_0)^2$. Experimentally observed magnetization curves for both MnO and FeO are shown in Fig. 3.1.9.
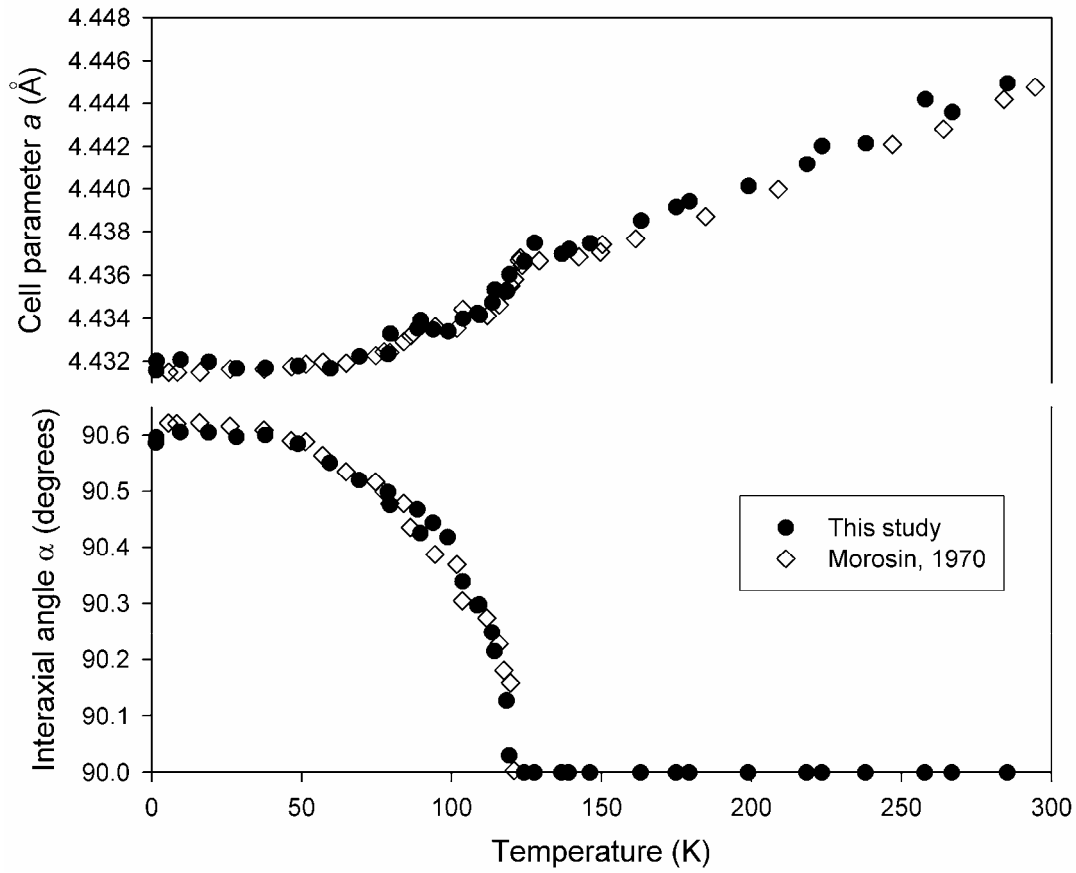
Fig. 3.1.8. Temperature dependence of cell parameters *a* (upper graph) and α (lower graph) of MnO. Solid circles – this study, open diamonds – from Morosin, 1970.

Within this study it was found that a simple Ising model satisfactory fits in a temperature range from 60 to 120 K. According to the Ising model, spontaneous magnetization in the vicinity of transition temperature is given by

$$\frac{M}{M_0} \sim \left(1 - \frac{T}{T_N}\right)^{2\beta},$$ (3.1)

where M is magnetization at given temperature T, T_N is the Néel temperature and constant β is independent of temperature. Resulting fit gives $T_N = 118.0 \pm 0.1$ K (in perfect agreement with previous results (Morosin, 1970; Shull et al., 1951; Srinivasan and Seehra, 1983) and β = 0.0826.
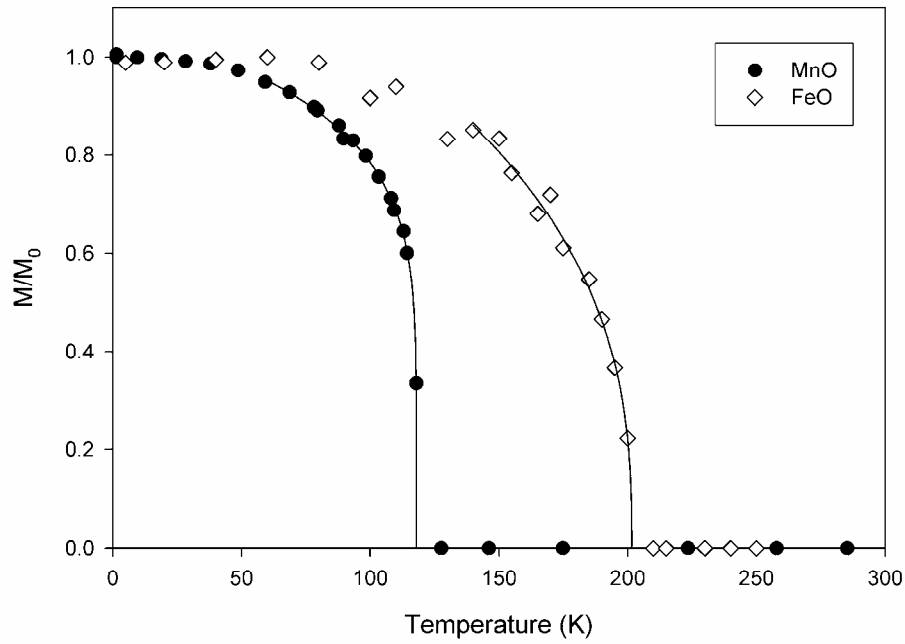
124

Fig. 3.1.9. Magnetization curves for MnO (solid circles) and FeO (open diamonds). Solid lines show fits to the Ising model (Eq. 3.1). Temperature uncertainties are comparable with symbols size.

Since trigonal distortion of a cubic lattice results mainly in interaxial angle changing and lattice parameter contraction is negligible small, the value of $(\alpha - \alpha_0)$ can be used as an quantitative measure of the distortion, and M/M_0 can be used as a measure of magnetization. As was mentioned above, there is no satisfactory analytical form either for M/M_0, or for $\Delta\alpha$ temperature dependences. Nevertheless the relations between these two quantities can be studied. At every given temperature one can measure both values simultaneously and plot $\Delta\alpha$ as a function of spontaneous magnetization without any reference to temperature (Fig. 3.1.10). If the Néel transition and structural distortion are assumed to coincide and a strong magneto-structural correlation exists, such a plot should be a continuous curve, starting from zero (in other words, at zero magnetization $\Delta\alpha$ is also equal to zero, and since some

magnetic order appears, interaxial angle starts to change). Such a curve (dashed line in Fig. 3.1.10) can be drawn, and experimental data fits satisfactory to $\Delta\alpha \sim (M/M_0)^2$ function.
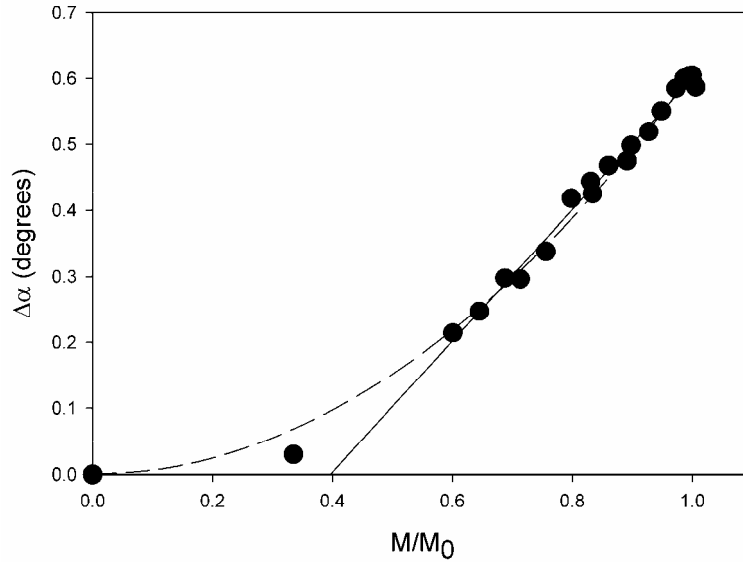

Fig. 3.1.10. Correlation between magnetization and lattice distortion in MnO. Dashed line is quadratic correlation and coinciding transitions, and solid line is linear correlation and non-coinciding transitions (see text).

Contrary, if one suggests that these two transitions diverges, resulting function $\Delta\alpha = f(M/M_0)$ must have non-zero intercept (in other words, there should be some points, when magnetization exists, but $\Delta\alpha$ is equal to zero). The present experimental data could be fitted also to this model (Fig. 3.1.10, solid line), giving even more simple linear correlation between $\Delta\alpha$ and (M/M_0). In this case MnO remains cubic until (M/M_0) reaches value of about 0.4. Magnetization curve of MnO is extremely steep just below the Néel temperature (see Fig. 3.1.9), and this value is reached at about 117.5 K. In other words, magnetic and structural transitions would differ for only 0.5 K in temperature that is comparable with temperature uncertainties and fluctuations in

the described experiment. Therefore, the accuracy of present study is not enough to distinguish between these two possible cases in MnO.

Neutron diffraction study of FeO

Data for FeO were collected with monochromator and focusing device which allowed to observe additionally to magnetic 3/2 1/2 1/2 reflection from primary beam (wavelength 4.741 Å) also reflections produced due to first harmonic of the beam with wavelength 2.3705 Å (structural 200 and 220 reflections). Lattice parameters of cubic FeO were determined from structural 200 and 220 reflections, and for rhombohedral phase (below ~160 K) from 200, 220 and -220 reflections. Figure 3.1.11 shows variation of lattice parameters with temperature.

Note, that contrary to MnO (Fig. 3.1.8) almost no anomaly in thermal expansion is observed near the Néel transition (around 200 K). The absolute value of $\Delta\alpha$ for FeO is about six times smaller than for MnO, resulting in higher relative uncertainties. Simple comparison of Figs. 3.1.9 and 3.1.11 shows that magnetic ordering does not coincide with structural distortion. Ising fit of FeO magnetization curve in temperature interval from 150 to 200 K (solid line in Fig. 3.1.9) gives T_N equal to 201.6 ± 0.1 K (expected value of T_N for this composition is about 201.9 K (Seehra and Srinivasan, 1984)) and $\beta = 0.1864$.
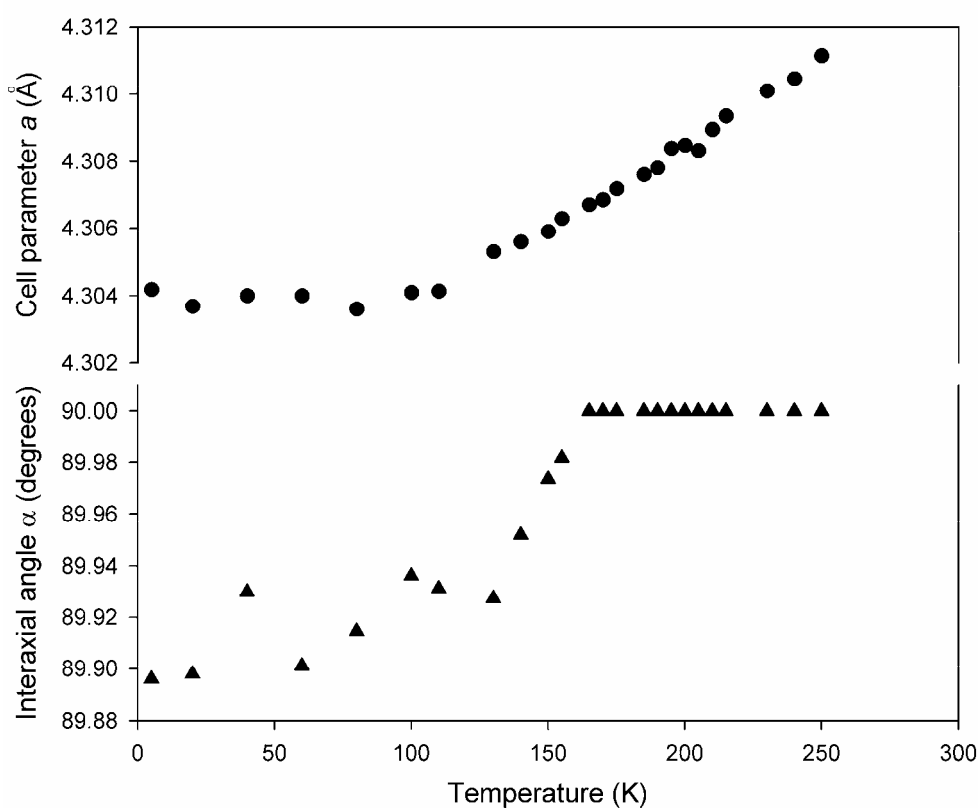
Fig. 3.1.11. Cell parameters a and α of FeO as a function of temperature.

Correlation between magnetization and trigonal distortion for FeO is shown in Fig. 3.1.12. Contrary to MnO, collected data for FeO show that correlation is absent (FeO remains cubic) in M/M_0 range from 0 to 0.7 that covers all temperatures higher than ~160 K. Below this temperature linear correlation between $\Delta\alpha$ and M/M_0 is observed. Results obtained for FeO indicate univocally that structural distortion occurs at much lower temperature (about 160 K) than the Néel transition (201 K).
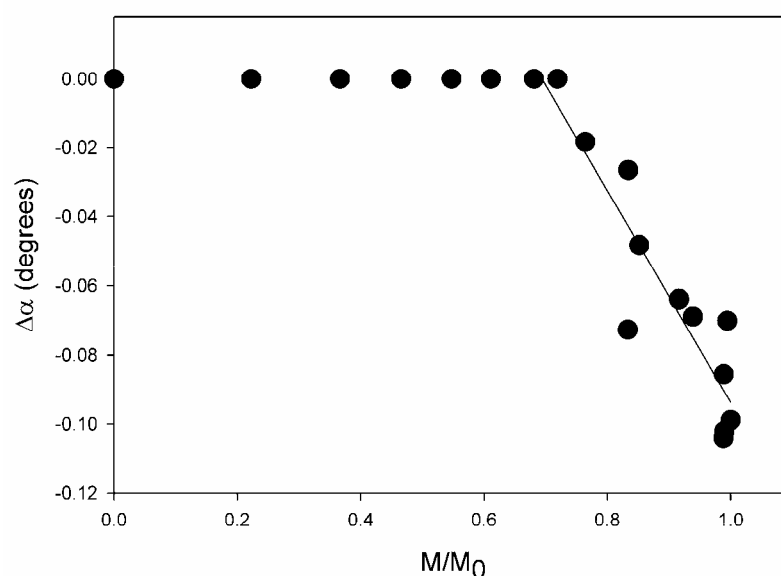
Fig. 3.1.12. Correlation between magnetization and lattice distortion in FeO. Solid line shows linear correlation in M/M_0 in a range from 0.7 to 1.

The above shown neutron diffraction and elasticity data indicate that magnetically ordered cubic phase of $Fe_{0.92}O$ exists also at high pressures at room and low temperatures, and at ambient pressure at a large temperature range. Later combined neutron diffraction, x-ray and Mössbauer study of FeO and MnO show that in FeO structural and magnetic transitions are not coupled in the whole studied pressure (up to 70 GPa) and temperature (1.5-1100 K) range (Fig. 3.1.13). In MnO at pressures up to about 3 GPa these two transitions coincide, however, at higher pressures a decrease of T_N was observed with appearance of a rhombohedral paramagnetic phase (Fig. 3.1.14) (Kantor et al., 2007b).
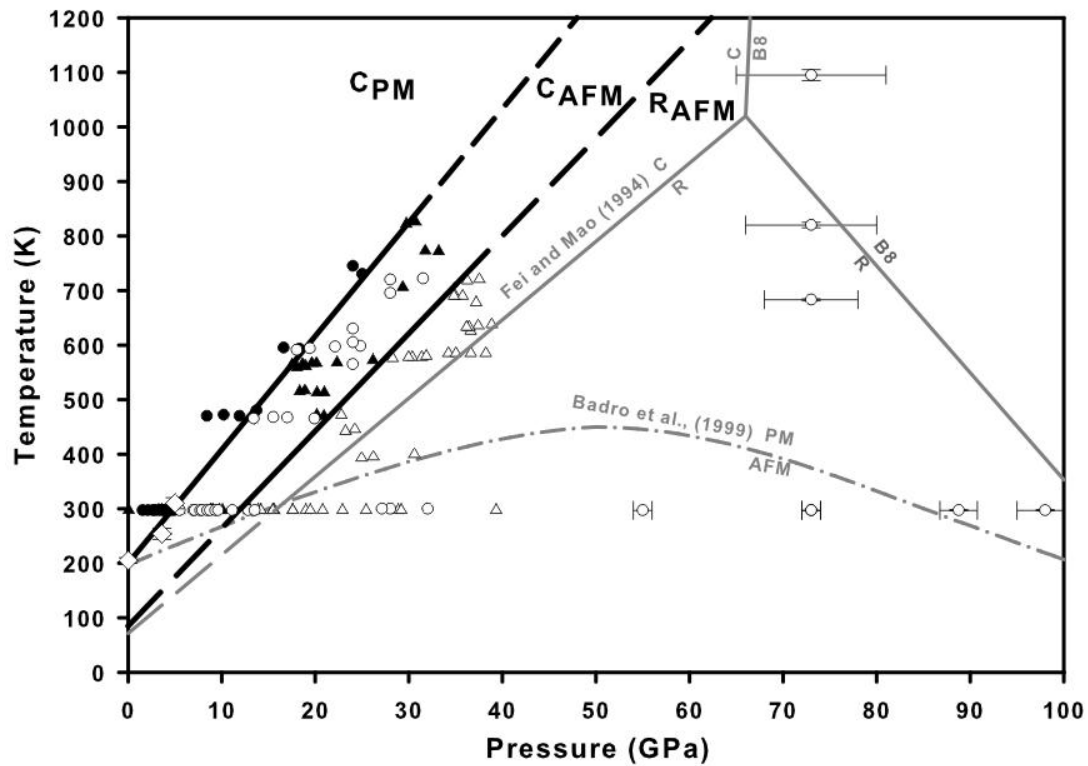
Fig. 3.1.13. Phase diagram of non-stoichiometric wüstite. Black lines – phase boundaries between cubic paramagnetic (C_{PM}), cubic antiferromagnetic (C_{AFM}), and rhombohedral antiferromagnetic (R_{AFM}) phases obtained in this study. Circles – Mössbauer spectroscopic runs: solid circles – paramagnetic phase, open circles – magnetically ordered phase. Triangles – x-ray diffraction studies: solid triangles – cubic phase, open triangles – rhombohedral phase. Diamonds show Néel temperature values obtained from neutron diffraction studies. The structural phase boundary by Fei and Mao (1994) and magnetic phase boundary proposed by Badro et al. (1999) are also shown for comparison in grey. C, R, and B8 are cubic, rhombohedral and NiAs-like hexagonal phases, respectively, and PM and AFM are paramagnetic and antiferromagnetic phases, respectively (after Kantor et al., 2007b).
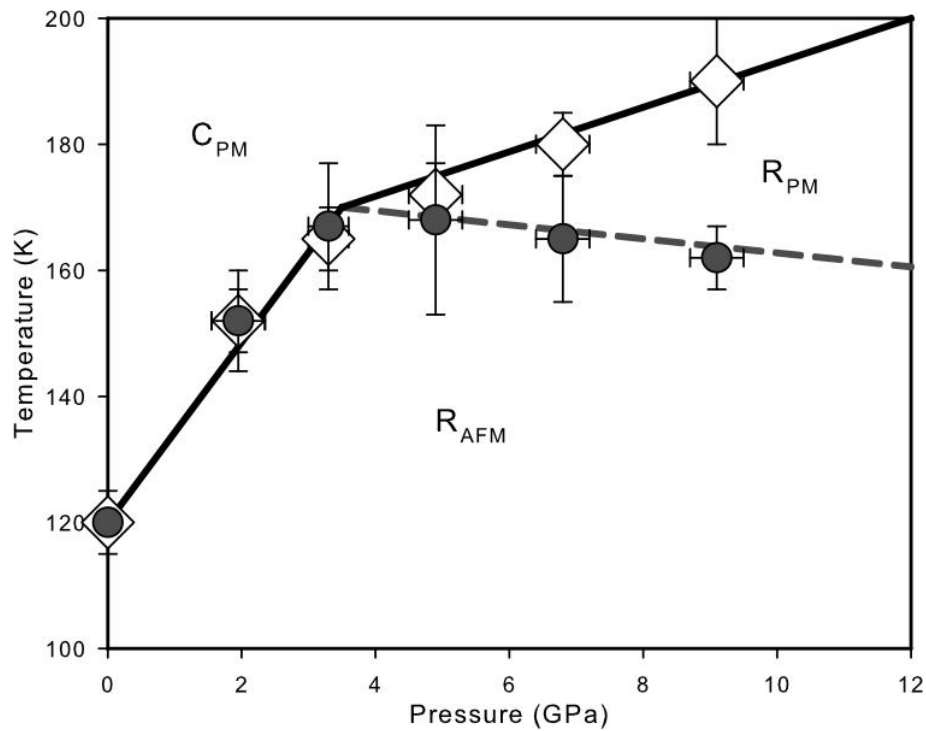
Fig. 3.1.14. Phase diagram of MnO. Open diamonds and the solid line are the phase boundary between cubic (C) and rhombohedral (R) phases. Filled circles and the dashed line are the boundary between paramagnetic (PM) and antiferromagnetic (AFM) phases (after Kantor et al., 2007b).

The important question appears concerning the actual magnetic structure of this new cubic antiferromagnetic phase of FeO.

3.1.4 Cubic magnetic structure

The available experimental and theoretical data are not sufficient to determine the magnetic structure of the FeO cubic phase. However, from the shown above data a qualitative model of the cubic magnetic structure of FeO that is consistent with experimental observations could be proposed.

At ambient pressure and low temperatures FeO is known to be type-II antiferromagnet (AF-II) with a crystal structure that has rhombohedral symmetry (Shull et al., 1951). According to random-phase Green's-function theory for AF-II *fcc* structures, spin-phonon interactions result in changes of the interaxial angle (α) and cell dimensions (*a*) (Morosin, 1970; Rodbell and Owen, 1964). Namely:

$$\Delta\alpha = Nz_1 J_1 \varepsilon_1 \left(\langle S_i \cdot S_j \rangle_{nn^p} - \langle S_i \cdot S_j \rangle_{nn^a} \right) / 24 C_{44} \qquad (3.2)$$

$$\delta a / a = Nz_2 J_2 \varepsilon_2 \langle S_i \cdot S_j \rangle_{nnn^a} / 6 \left(C_{11} + 2C_{12} \right) \qquad (3.3)$$

where α is the rhombohedral setting interaxial angle ($\alpha = 60$ for the cubic structure), N is the number of spins in the system, z_1 (=12) and z_2 (=6) are the number of nearest-neighbour (*nn*) and next-nearest-neighbour (*nnn*) metal ions, $<...>_{nn^p}$, $<...>_{nn^a}$ and $<...>_{nnn^a}$ refer to the thermal averages over parallel *nn*, antiparallel *nn*, and antiparallel *nnn*, respectively, J_1 and J_2 are *nn* and *nnn* exchange interactions, $\varepsilon_1 = -r(\partial \ln J_1)/\partial r$ and $\varepsilon_2 = -r(\partial \ln J_2)/\partial r$, r is interspin distance, and finally C_{11}, C_{12} and C_{44} are the appropriate (cubic) elastic constants.

Equation (3.3) implies that in AF-II structures, *nnn* interactions are coupled with changes in C_{11}, C_{12} and volume striction. It is reasonable to assume that a cubic antiferromagnetic structure of FeO exists (at room temperature and pressures between ~5 and ~17 GPa), and that in a cubic magnetic structure the *nnn* interactions are the same as in the rhombohedral AF-II structure. Since C_{44} changes smoothly and continuously up to 9 GPa and $\Delta\alpha = 0$ in this pressure range (Mao et al., 1996), the *nn* spin distribution in the cubic magnetic phase of FeO is not equal to that in the classical AF-II structure.

In the classical rhombohedral (R_{AFM}) structure the parallel spins form sheets within 111 planes of the lattice, where each adjacent sheet is antiparallel. Magnetic

interactions between sheets give rise to a slightly attractive or repulsive force resulting in rhombohedral distortion of the lattice below Néel transition. In the R_{AFM} structure, all the next-nearest neighbours are antiparallel, and only a half of the nearest neighbours are antiferromagnetically coupled, while the other half being coupled ferromagnetically (Tebble and Craik, 1969) (Fig. 3.1.15a). Assuming *nnn* interactions (of FeO) the same as in the R_{AFM} type, in the proposed structure the spins are distributed in the first coordination shell in a different way: six *nn* with antiparallel spins lie in the same close-packing layer as the central ion, while six *nn* with parallel spins lie in upper and lower hexagonal layers (Fig. 3.1.15b).
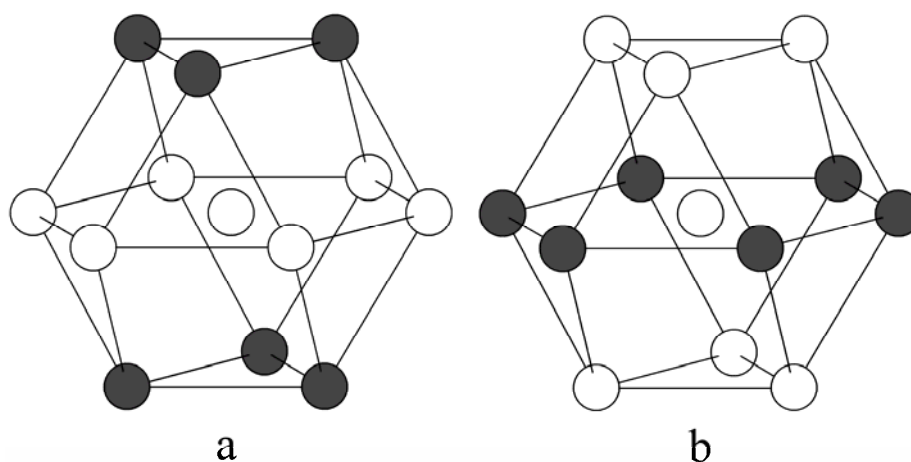

Fig. 3.1.15. Nearest-neighbour environment of the metal ion in the (a) R_{AFM} and (b) C_{AFM} structures. Ions with ''+'' spins are represented by open circles and ions with ''-'' spins are shown by filled circles. The cubic <111> direction is vertical.

This cubic antiferromagnetic structure (C_{AFM}) is closely related to the classical R_{AFM} type, but the symmetry remains cubic. Relatively to the cubic *fcc* lattice, the proposed magnetic structure has doubled cell dimensions and a space group $Fd\bar{3}m$, while the crystallographic space group remains $Fm\bar{3}m$. The C_{AFM} structure can be considered as an intermediate step towards the R_{AFM} structure since every hexagonal

layer consists primarily of ions with parallel spins with only one quarter of ions having antiparallel spins.

In principal neutron diffraction is able to distinguish between different types of magnetic ordering. However, the analysis shows that non-collinear C_{AFM} structure and "canonical" R_{AFM} magnetic would produce similar neutron powder diffraction, and shown low temperature neutron data agree with the proposed model. A low-temperature single-crystal neutron diffraction study is necessary to resolve this problem.

3.1.5 Conclusions

In order to summarize, this part of the work presents the first determination of the full elastic tensor (C_{ij}) of FeO to high precision at hydrostatic pressures up to 9.6 GPa, using gigahertz ultrasonic interferometry in the DAC; and shows that a unique combination of Mössbauer spectroscopy and GHz-ultrasonic experiments in the DAC reveals new information about magneto-elastic coupling and structurally hidden phase transformations. A pressure-induced mode softening of the C_{44} elastic constant by 20% at 10 GPa, consistent with previous ultrasonic measurements to 3 GPa (Jackson et al., 1990) was monitored by GUI. An unusual discontinuity in the pressure derivatives of C_{11} and C_{12} at 4.7 ± 0.2 GPa is consistent with the pressure at which a magnetic ordering starts, as observed by high-pressure Mössbauer study. The results indicate that an intermediate partially magnetic but still cubic phase of FeO probably exists at room temperature and in pressure range from ~5 GPa to ~17 GPa. The neutron diffraction study proves the existence of cubic magnetic phase of FeO also at low temperatures at ambient and high pressures.

Inelastic x-ray scattering experiment extended pressure range of measurements up to 20 GPa, and individual elastic constants, measured by IXS and GUI, are in a reasonable agreement. Additional analysis of combined IXS and XRD study of FeO revealed very unusual features of high-pressure behaviour of FeO that could be interpreted as a strong anelastic relaxation, as is discussed in the following chapter.

3.2 Anelastic behaviour of $Fe_{0.95}O$ under high pressures: Evidence from static compressibility and inelastic x-ray scattering experiments

The elasticity measurements of $Fe_{0.95}O$ by IXS to 20 GPa, described in the preceding section, were combined with x-ray diffraction in a DAC, which provided data on unit cell volume and, hence, density as a function of pressure (measured using ruby fluorescence gauge). Both series of experiments allowed extracting independently the bulk modulus of the studied material. Normally, for many materials the values of bulk modulus obtained from static compressibility and dynamic measurements should coincide within the experimental error (with the conversion factor between isothermal and adiabatic bulk moduli), as was shown, for example, for periclase MgO (Zha et al., 2000) and magnetite Fe_3O_4 (Reichmann and Jacobsen, 2004).

In the present study the effective adiabatic bulk modulus K_S was calculated for every dataset (at every pressure point) using the individual elastic constants, showed in the previous section. The bulk modulus was calculated according to the Eq. 2-13

(see section 2.1) and converted into isothermal modulus K_T using the following equation:

$$K_T = K_S(1 + \alpha\gamma T)^{-1}$$ (3.4)

where values for α and γ (thermal expansion and Grüneisen parameter respectively) are taken from Saxena et al. (1993). The difference between adiabatic and isothermal bulk moduli for the studied material did not exceed 2 %. The coefficients of a finite-strain third-order Birch-Murnaghan equation of state (EoS) were determined using K_T-V relation (Zha et al., 2000). Pressure-volume dependence was also fitted independently with the same type of EoS. Here only the results obtained using the third-order Birch-Murnaghan equation of state are discussed, but 4th order Birch-Murnaghan EoS or other forms of equations of state ("universal" natural strain, Vienet EoS) were also tested and they did not affect the results discussed hereafter.

In order to estimate visually K_0 and K_0' values the F-f plot (Angel, 2000) is very helpful. It can be applied to any isothermal EoS based upon finite strain. For the Birch-Murnaghan EoS, based upon the Eulerian definition of finite strain f_E (Eq. 1.32, Chapter 1), a "normalized stress" is defined as

$$F_E = P / 3f_E(1 + 2f_E)^{5/2}$$ (3.5)

When P-V data are transformed into f_E and F_E and plotted with f_E as the abscissa a direct indication of the compressional behaviour can be obtained. If all of the data points lay on a horizontal line of constant F, then the K_0' equals to 4. This indicates that data can be fitted with a second-order truncation of the Birch-Murnaghan EoS. A positive slope implies K_0' > 4, while a negative slope corresponds to K_0' < 4. The slope is equal to $3K_0(K'-4)/2$, and the data can be adequately described by a third order truncation of the Birch-Murnaghan EoS (BM3). In very rare cases, when the f_E –

136

F_E plot is not linear, a 4th order EoS is necessary. In all cases the intersection of the fit with the F_E axis corresponds to the K_0 value.

The values of the effective ambient conditions bulk modulus determined from IXS and compressibility measurements coincide within the experimental error (K_T = 162 ± 3 GPa). However, K' values differ significantly (5.3 ± 0.2 for IXS data vs. 1.79 ± 0.9 for diffraction data) (Fig. 3.2.1). At pressures of about 17 GPa (just below the cubic-to-rhombohedral transition) difference in bulk modulus reaches ~40 GPa, at least one order of magnitude larger than the associated experimental uncertainty.

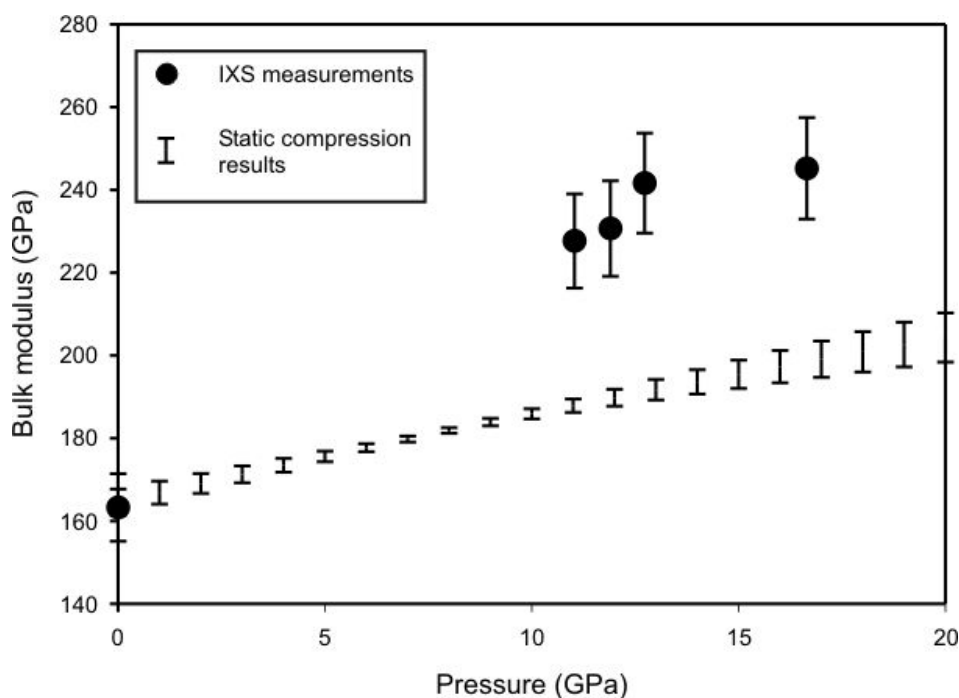Fig. 3.2.1. Bulk modulus of $Fe_{0.95}O$ as a function of pressure.

In principle there could be several explanations for the difference between bulk moduli measured by static and dynamic techniques. The first idea raised up is the strong magneto-elastic coupling occurs in wüstite. The results of Struzhkin and co-authors (2001), for example, suggest that a strong magnetoelastic coupling in FeO is

the driving force behind the changes in the phonon spectrum of the material. However the present elasticity measurements by GUI, described in the section 3.1, indicate the occurrence of very weak magnetoelastic coupling: there, actually, is a change in pressure derivatives of some individual elastic constants, but the change is very small and can be detected only by such an accurate method as GUI. Inspection of the corresponding theory of magnon-phonon coupling in antiferromagnetic materials (Peletminskii, 1960) shows that the value of the bulk modulus determined from phonon dispersion should be lower, than the value obtained from static measurements. The reason for this is the appearance of interaction between elastic waves and spin waves, which leads to a change in the velocity of sound and to an additional sound absorption. The latter could not be detected by static compressibility measurements, because spin waves are not excited in this case. In a low-Q part the effect results in decreasing sound velocities in the material. In the present study the opposite effect was observed. The unusual compressional behaviour of Fe_xO could be explained by anelastic relaxation (Nowick and Berry, 1972) in wüstite, which occurs due to point defects associated with its nonstoichiometry.

If any anelastic relaxation exists (when the equilibrium strain for a given stress is achieved only after certain finite time interval) the effective elastic moduli measured by different methods would systematically vary, depending on sampling frequency, absolute temperature, and material properties (Nowick and Berry, 1972). Anelasticity of a solid appears due to defects or other crystal imperfections when the energy minimum is achieved not only by varying the atomic geometry but also by changes in the materials' mesostructure (e.g. structure with a characteristic length larger than the crystal unit cell size), such as twin domain walls, dislocations, stacking faults, etc.

Jeanloz and Hazen (1983) suggested that wüstite could behave anelastically and related this phenomenon to defect structure. The variation of elastic properties with defect concentration or stoichiometry is a fundamental problem in the study of defect materials and has generally not been well understood by either experiments or theories (Jeanloz and Hazen, 1983; Zhang, 2000).

The lattice parameter a of Fe_xO varies nearly linearly with composition (McCammon and Liu, 1984; Simons, 1980), while bulk moduli measurements are highly controversial – reported values range from 142 GPa to 182 GPa (Mao et al., 1996). It was suggested that the bulk modulus K_T varies non-linearly with wüstite composition (Zhang, 2000; McCammon and Liu, 1984). Other authors suggested that difference between static and dynamic measurements of bulk moduli is more important than the compositional dependence (Jeanloz and Hazen, 1983).

In the wüstite structure defects form clusters of different size and geometry (Long and Grandjean, 1991), and the distribution of defect clusters is known to be not random (Welberry and Christy, 1997). Computer simulations show that different defect clusters and their distribution results in different values of free energy, equilibrium volume, and bulk modulus even for the same composition (Minervini and Grimes, 1999; Haavick et al., 2000). Therefore, the redistribution of defects is the most likely mechanism of anelastic relaxation in Fe_xO.

Presented here observations show that significant anelastic behaviour appears only at high pressure, when a certain strain is applied. The energy decrease could be assumed due to anelastic relaxation and described by a polynomial function of strain

$$- \Delta E^{anelastic} = Af^2 + Bf^3 + Cf^4..., \tag{3.6}$$

where f is the Eulerian strain (Eq. 1.32).

The elastic part of strain-induced energy change is described here with the generally used Birch-Murnaghan EoS (Eq. 1.41). Taking into account thermodynamic relations

$$P = -\left(\frac{\partial E}{\partial V}\right)_S \tag{3.7}$$

and

$$K_T = -V\left(\frac{\partial P}{\partial V}\right)_T \tag{3.8}$$

the anelastic "excess" pressure and bulk modulus could also be calculated. The experimental data can be well fitted with only the cubic term of strain, $\Delta E^{anelastic} = Bf^3$, with B equal to 826 ± 47 eV per formula unit (one oxygen atom). This model describes both the elastic contribution (elastic limit) probed by acoustic phonons and the total contribution (elastic limit + anelastic relaxation), determined by static compression experiments (Fig. 3.2.2).

If Fe_xO data would be used to constrain the primary pressure scale (Zha et al., 2000), the calculated pressure around 20 GPa would be about 4 GPa higher, than the real pressure for the corresponding strain. Of cause, most materials would not show such a strong anelasticity, but the differences of the order of tens of gigapascals that are discussed when comparing different equations of states (Dewaele et al., 2004) could in principle be explained by anelastic relaxation caused by defect diffusion that exist in any real crystals.
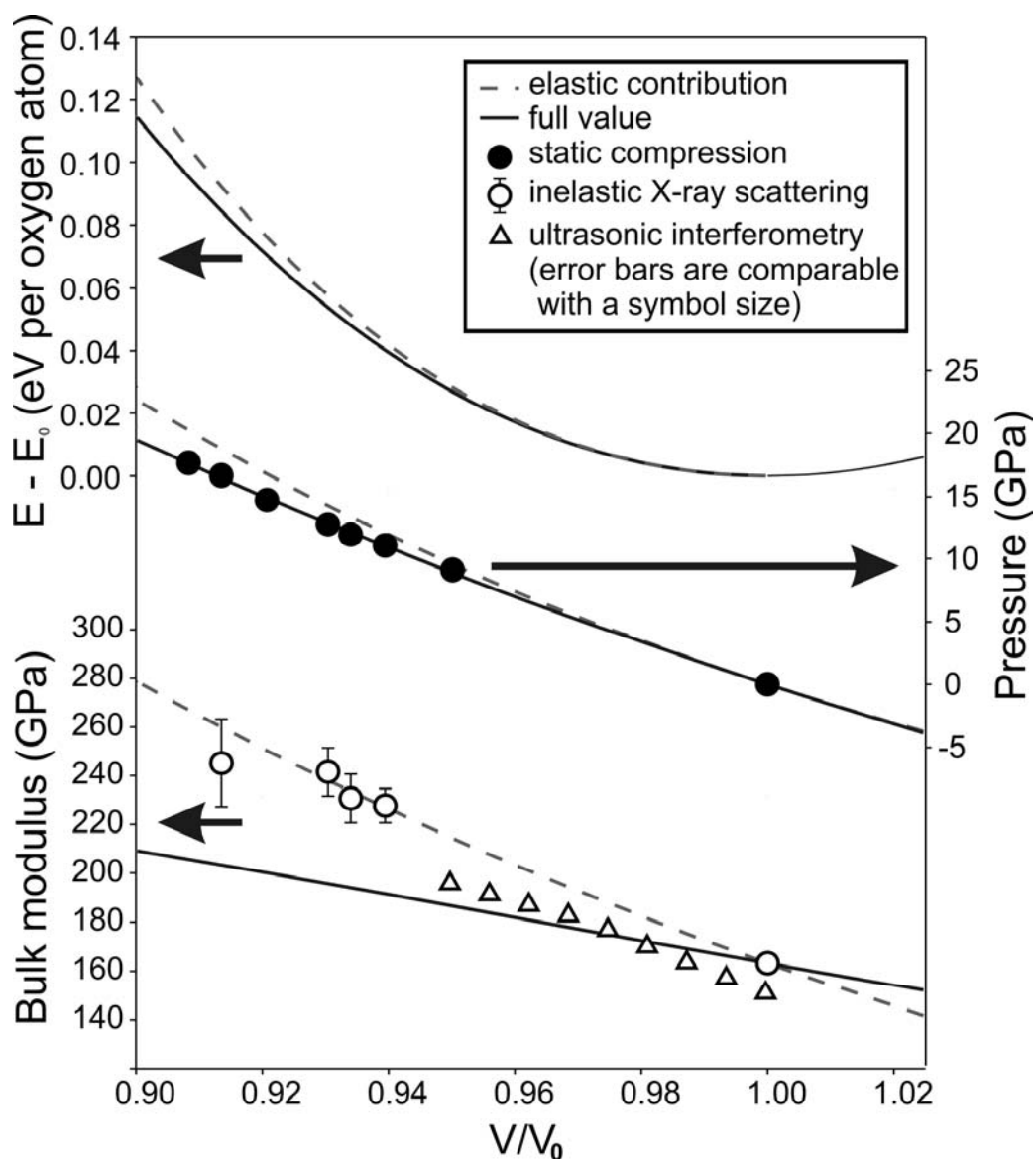
Fig. 3.2.2. The empirical model for the strain-induced anelastic relaxation: volume dependence of free energy, pressure, and bulk modulus (top to bottom). Dashed lines show the elastic contribution, calculated according to the BM3 EoS; solid lines display the result including anelastic relaxation as given by eq. 3.6. Experimental values for static pressure (solid circles) represent full stress; experimental values of the bulk moduli determined by IXS (present study of $Fe_{0.95}O$) and gigahertz ultrasonic interferometry (study of $Fe_{0.94}O$ by Kantor et al. (2004a)) probe only the elastic contribution (open circles and triangles, respectively). Systematic offset of the bulk modulus measured with ultrasonic interferometry can be explained with the uncertainty in the initial sample thickness measurement, which will not affect the slope, virtually coinciding with those shown by dashed line.

Elastic properties determined from the seismic waves velocities would be frequency-dependent and high-frequency measurements (Kantor et al., 2004a) would be close to the "elastic limit", while low-frequency measurements would reflect a sum of elastic and anelastic contributions. The main implication of this study for high-pressure mineral physics is that high-frequency and phonon dispersion measurements could give effective elastic moduli different from those seen by low-frequency seismic waves in geophysical observations. In case of any internal structural relaxations, associated with atomic diffusion, a certain characteristic time τ is required to reach an equilibrium state. If the inverse sampling frequency is smaller than τ, only elastic relaxation occurs, and the measured bulk modulus and K' would be higher, that those measured for inverse frequency larger than τ. All materials with significant amount of defects and all solid solutions and alloys could possess anelastic relaxation, and Fe_xO is probably one of the clearest cases.

Although the present study is not a systematic one, the proposed model could explain major reason for controversy of elastic behaviour of wüstite that exists for several decades. The parameters in Eq. 3.6 vary with composition together with the "elastic" parameters K and K'. In case when parameter A in Eq. 3.6 is not equal to zero, the bulk moduli measured by static and dynamic methods would also be different, as suggested by Jeanloz and Hazen (1983).

Due to the pressure-induced anelastic relaxation initial value of K' could be small, and the commonly used second-order truncation of finite strain equation of state (assuming $K' = 4$) is not longer valid. Most of the powder diffraction compressibility studies does not allow the determination of volume and pressure precisely enough to refine K' value and the determination of K is not reliable (K and K' are strongly correlated parameters). Non-hydrostatic compression also affects

significantly the data and cannot be compared directly to hydrostatic compressibility. Therefore, reliable values of K_T and K' from static compression could be obtained only from single-crystal x-ray diffraction studies under hydrostatic conditions (Jacobsen et al., 2005b; Ding et al., 2005; Shu et al., 1998). The author re-analyzed such available data for various Fe_xO single crystals using the third order Birch-Murnaghan equation of state and compared K_0 and K' values to those reported from dynamic measurements (Fig. 3.2.3). A fairly good agreement between static and dynamic measurements of K_0 was found; although dynamic values for K_0 are systematically lower (all the shown data are converted to isothermal values). A compositional variation of K_0 could also be seen. As suggested by empirical model of anelastic relaxation in wüstite, K' values are significantly different in static and dynamic experiments, which imply that this model is valid for Fe_xO with various composition.

Combined IXS and x-ray diffraction study of Fe_xO shows that anelastic relaxation at high pressure could be enormously strong and could not be considered as a negligible effect *a priori*. All solid solutions (and all minerals are solid solutions), non-stoichiometric compounds, materials with complex mesostructure (particularly nano-structured solids) have the internal degree of freedom, and could therefore experience internal relaxation and show deviations from normal elastic behaviour.
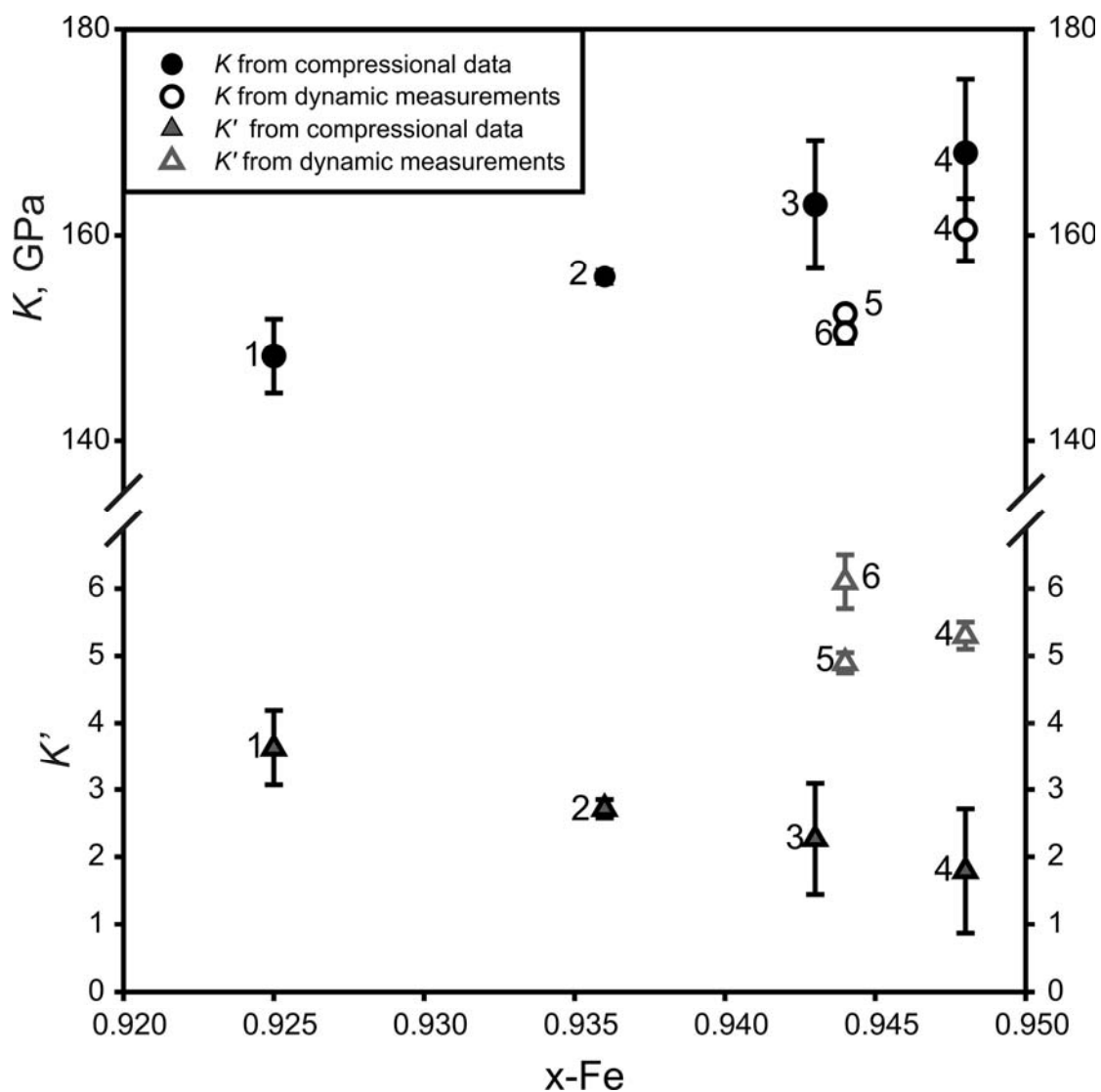
Fig. 3.2.3. Isothermal bulk modulus of Fe$_x$O and its pressure derivative as a function of composition. Dynamic measurements are indicated by open symbols, whereas static measurements are shown as filled symbols. The composition was calculated from the lattice parameter (McCammon and Liu, 1984) quoted in each study. Compressional data were taken from: 1 – Jacobsen et al., 2005b; 2 – Ding et al., 2005; 3 – Shu et al., 1998; 4 – present study. Dynamic techniques used to determine the bulk modulus include ultrasonic measurements (5 - Jackson et al., 1990; 6 – Kantor et al., 2004a) and inelastic x-ray scattering (4 – present study).

3.3 IXS study of polycrystalline Fe$_{0.78}$Ni$_{0.22}$-alloy at high pressures and temperature

Properties of major constituents of the Earth's core, iron and its alloys, have long been of great interest to geophysicists. Cosmochemical data and the composition of iron meteorites suggest that Earth's core contains a significant (5 to 25 %) amount of nickel (Anderson, 1989). Iron-nickel alloy with 5-25% Ni content is also thought to be the main component of the cores of the Mars, Mercury, Moon, satellites of Saturn and Jupiter (Encrenaz et al., 1995; Robbins et al., 1995; Bottke et al., 2006). Information on the behaviour of Fe–Ni alloys at high pressure and temperature (P–T), such as phase relations and thermal equations of state, is essential for interpreting seismic and geomagnetic observations and for computer modelling of the Earth's deep interior. While pure Fe at high P–T has been the subject of numerous studies (Mao et al., 1990; Saxena et al., 1995; Yoo et al., 1995; Boehler, 1993; Andrault et al., 1997; Dubrovinsky et al., 2000b; Crowhurst et al., 2005; Antonangeli et al., 2004), there are far fewer studies on Fe–Ni alloys (Huang et al., 1992; Lin et al., 2003; Mao et al., 2005; Dubrovinsky and Dubrovinskaia, 2003).

At ambient conditions, the stable phase of α-Fe has the body-centred cubic (*bcc*) structure. This phase transforms into a γ–Fe (*fcc*) phase upon increasing temperature above 1185 K, and then transforms to δ-Fe (another *bcc*–structured) phase before melting (Saxena et al., 1995). At high pressure, both *bcc* and *fcc* phases transform into the ε (or *hcp*) phase (Takahashi and Bassett, 1964). This phase has a broad stability region, and ε–Fe is generally considered to be stable at the inner core conditions (Hemley and Mao, 2001). Some theoretical calculations (Belonoshko et al.,

2003) predict the *bcc* structure of iron in this region near the melting temperature. Also, the *bcc* phase of Fe could be stabilized at the inner core conditions by dissolving some amount of "light" elements, in particular, silicon (Vocadlo et al., 2003; Lin et al., 2002). Recent experimental studies by Dubrovinsky et al. (2007) confirmed that iron alloys with significant nickel, sulphur or silicon content adopt the *bcc*-structure at the Earth's inner core conditions. Pure Ni is thought to be in the *fcc* structure at pressures over 300 GPa and up to the melting temperature (Yoo et al., 2000). The ambient pressure phase diagram of Fe-Ni alloys shows the existence of both *fcc* and *bcc* phases; the *fcc* phase, depending on composition, has a complex magnetic behaviour, and is known to exist in different magnetic states (Hausch and Warlimont, 1973; Dubrovinsky et al., 2001a; Meyer and Entel, 1995). The lower temperature field (T < 400 °C) of the Fe–Ni phase diagram has a complex configuration that includes a paramagnetic low-Ni disordered *fcc* phase, as well as the ordered compounds FeNi (tetrataenite) and Ni_3Fe (Guenzburger and Terra, 2005). The high-pressure phase diagram of Fe-Ni alloys is still not well constrained, and details of stability fields of *bcc*, *fcc* and *hcp* phases are not clear even for low-Ni (below 25 at%) alloys (Mao et al., 1990; Huang et al., 1988; Lin et al., 2003; Mao et al., 2005; Dubrovinsky and Dubrovinskaia, 2003).

Seismological observations provide us constraints concerning pressure, density and sound wave velocities in the outer liquid and inner solid core, but experimental data of Fe-Ni elasticity at appropriate conditions are missing. Although sound wave velocities in pure ε–iron were measured at high pressures and temperatures (Lin et al., 2005), the effect of its transition to the γ-phase and on the Ni content were not known so far. However even relatively small amounts of additional components could change phase relations and thermophysical properties of iron alloys

(Boehler, 1993; Mao et al., 2005; Lin et al., 2002; Dubrovinsky et al., 2001a; Schilfgaarde et al., 1999; Vidale and Earle, 2000): addition of Ni is thought to increase the *fcc* phase stability field. Therefore, the understanding and interpretation of composition and properties of the Earth's core (such as seismic anisotropy, fine-scale heterogeneity, super-rotation (Vidale and Earle, 2000; Breger et al., 2000)) require detailed studies of the Fe-Ni system at high pressures and temperature.

The described in the previous chapter method for measuring phonon dispersion curves at extreme conditions was applied to the investigation of the elasticity of the certain iron-nickel alloy. The first *in situ* measurements of the longitudinal sound velocities V_P in *fcc* $Fe_{0.78}Ni_{0.22}$ alloy were performed at high pressures and temperature by means of inelastic x-ray scattering from polycrystalline material. The composition was chosen as one of the high-end probable Ni-concentrations in the Earth's core in order to see the strongest possible effect of Ni addition on the bulk sound velocities in the alloy. The study was combined with the determination of the EoS of the alloy by x-ray diffraction (XRD) that provided to derive as well the transverse velocity V_S.

A single-crystal of iron-nickel alloy containing 22 at% Ni, commercially available from the IBS Company (Germany), was synthesized by the Chochralski method. The metastable *fcc* crystal, quenched from high temperature, completely transformed to the polycrystalline *bcc* phase (during crystal cutting and polishing) as confirmed by XRD studies. The Mössbauer spectrum of the starting material, collected at ambient conditions, shows a magnetically ordered structure with a hyperfine field of about 34 T and a significant B_{HF} distribution, typical for *bcc* Fe-Ni alloys (Narayanasamy et al., 1979) (Fig. 3.3.1a). The sample was polished to a thin plate of about 19 µm thickness, loaded into a diamond anvil cell and compressed

above 12 GPa. As a result it completely transformed to the polycrystalline high-pressure *fcc* phase used for further measurements.
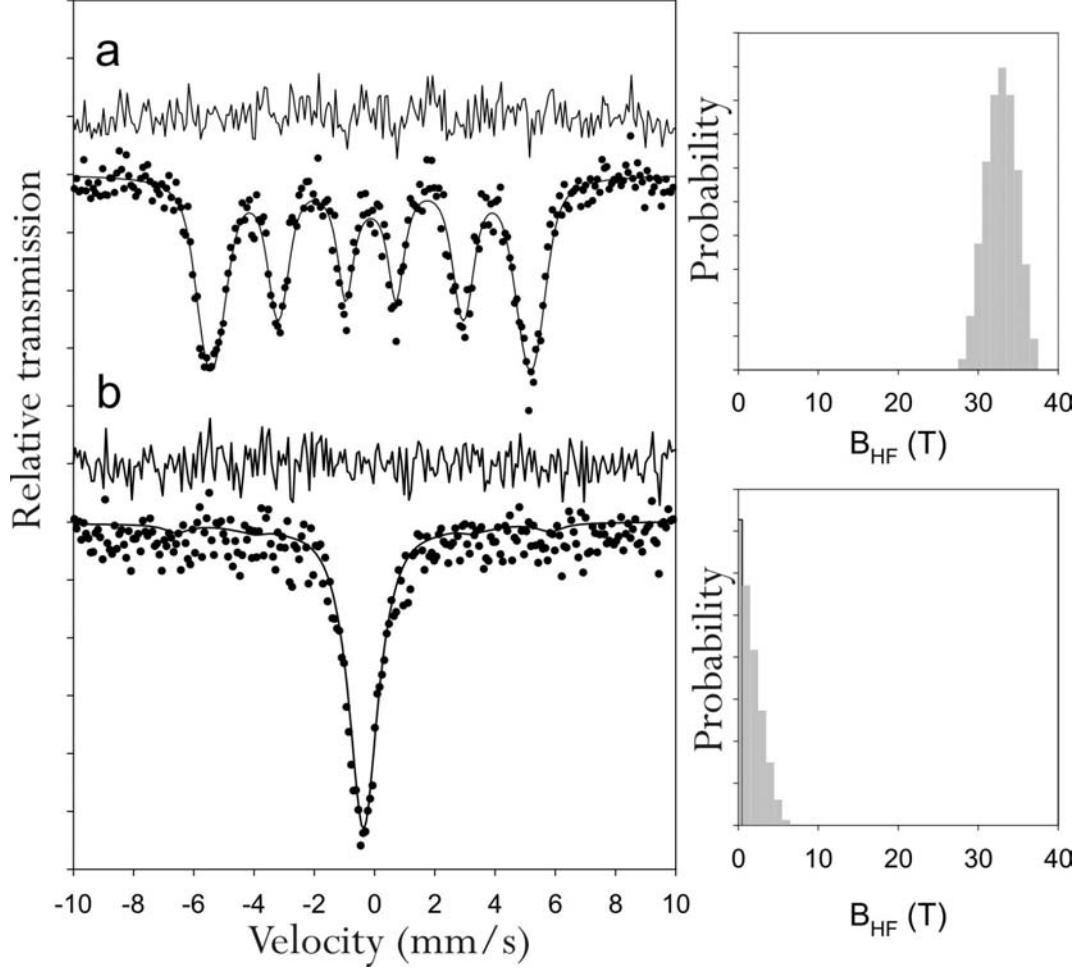

Fig. 3.3.1. ^{57}Fe Mössbauer spectra of Fe$_{0.78}$Ni$_{0.22}$ alloy at ambient conditions (a, *bcc* phase) and at 23 GPa (b, *fcc* phase). Black dots are the experimental data; solid lines are the total fits. Residuals are shown above each curve, and a hyperfine field distribution is shown at the right of each spectrum. Velocity scale is relative to the ^{57}Co/Rh source.

A four-pin modified Merrill-Basset type DAC (Dubrovinskaia and Dubrovinsky, 2003) equipped with an internal miniature platinum resistive heater was used to compress and heat the sample. Diamonds with 250 μm culet diameter were used as anvils. A rhenium gasket with 260 μm initial thickness was pre-indented to

~45 μm and a hole of 125 μm in diameter was drilled. A Fe-Ni sample was loaded along with a large amount (~50 % of volume) of pure polycrystalline LiF. One of the loadings was performed without LiF and we didn't observe any difference between experiments with and without LiF. Several small ruby chips were loaded into the sample chamber for pressure measurements (Mao et al., 1986). Temperature dependence of the ruby fluorescence was taken from Rekhi et al. (1999). Temperature was measured using an ultra-thin R-type thermocouple, located close (within less than 1 mm) to the sample chamber. The thermocouple was fixed with a ceramic bond on the surface of the metal gasket right near the diamond/gasket interface.

IXS measurements were performed on the ID28 beamline at the ESRF. The instrument was operated in the Si(888) configuration, with an incident photon energy of 15.817 keV and a total instrumental energy resolution of 5.5 meV full width at half maximum (FWHM). The transverse dimensions of the focused x-ray beam of 25×60 μm^2 (horizontal×vertical, FWHM) were further reduced by slits to approximately 10×15 μm^2. The momentum resolution was set by slits in front of the analyzers to 0.25 nm^{-1}. Two sets of experiments, at room temperature and at 715 (10) K, have been performed. The special-designed vacuum chamber, described in the section 2.2 of the present work, was used for performing all the experiments. Before and after each measurement (taking about 10 hours) an in-situ 1-D monochromatic x-ray diffraction pattern was collected for lattice parameter determination exactly from the same sample. The final pressure value was calculated from the lattice parameters (see below).

High-pressure and high-temperature angle-dispersive XRD study of the same Fe-Ni alloy compressed in LiF pressure-transmitting medium was performed using the high-resolution powder diffractometer of the Swiss-Norwegian BM01 beamline at

the ESRF. Sample loading and experimental protocol was exactly the same as for the IXS measurements, in order to avoid any systematic uncertainty. A monochromatic beam with 0.7995 Å wavelength was used and the diffracted intensities were registered with a MAR345 image plate. Experimentally measured pressure-volume relations at room temperature and at 715 K were reduced to the isothermal third order Birch-Murnaghan equations of state with a least-square minimization routine.

Powder x-ray diffraction revealed that $Fe_{0.78}Ni_{0.22}$ alloy is stable in the *fcc* phase throughout the whole studied *P*, *T* range. An example of the analysed integrated pattern of the spectrum collected at 24.4(2) GPa and room temperature is shown in Fig. 3.3.2. The Debye-Scherrer rings of the studied sample show no evidence of "spotty" diffraction or inhomogeneous intensity distribution, indicating the absence of notable preferred orientation. The Mössbauer spectrum of the *fcc* phase, collected from ^{57}Fe enriched $Fe_{0.78}Ni_{0.22}$ alloy at 23 GPa shows negligible magnetic interactions (Fig. 3.3.1b). The measured volume in the 20 to 72 GPa pressure range was fitted to the third order isothermal equations of state at 300 K and at 715 K with the following coefficients:

K_{300}=161 (1) GPa, K'_{300}=4.97(1), V_{300}=6.89(1) cm^3/mole

K_{715}=160 (1) GPa, K'_{715}=4.97(2), V_{715}=6.96(1) cm^3/mole

All the parameters were fitted, since ambient pressure volume at 300 and 715 K cannot be measured (high-pressure *fcc* phase is not quenchable) and is estimated from the obtained EoS. These parameters were used to calculate the pressure and bulk modulus *K* from the measured volume for every *P-T* point of the IXS experiment.
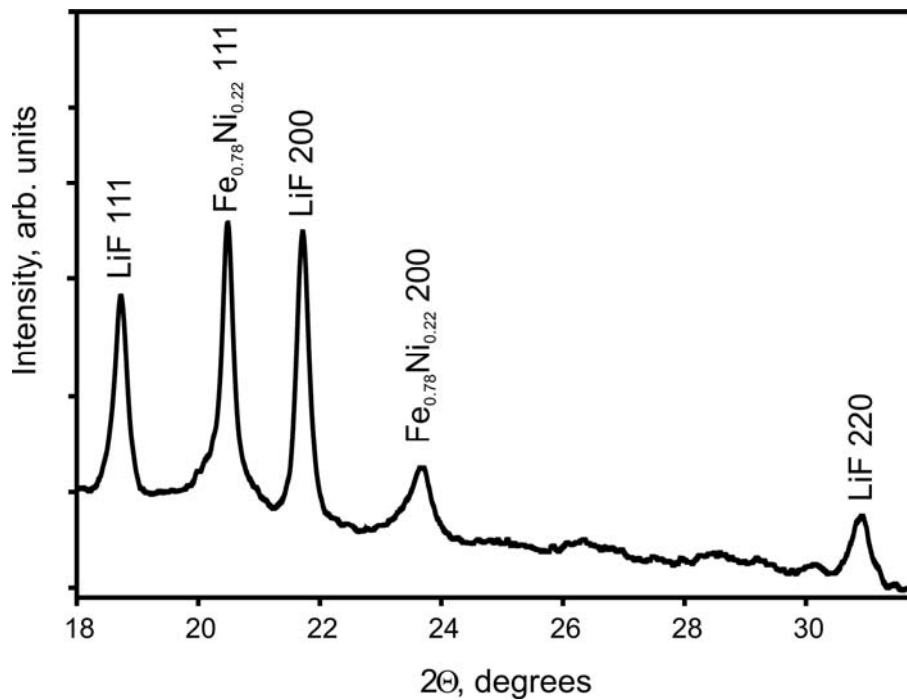
Fig. 3.3.2. Typical example of analysed integrated XRD patterns
of the spectrum collected at 24.4 GPa and room temperature.

Fig. 3.3.3 shows an example of the IXS spectra collected at the highest reached pressure (71.7 GPa) and 715 K. It is characterized by an elastic contribution centred around zero energy, and two inelastic features, corresponding to the longitudinal acoustic phonons of Fe-Ni and the transverse acoustic phonon of diamond. Due to the much higher sound velocity (~11 km/s) the diamond contribution moves rapidly out of the spectral window of interest with increasing momentum transfer. The energy position $E(Q)$ (Q is the wave vector) of the phonons was extracted using a model function composed of several Lorentzian's plus Gaussian peak functions, and the number of peak components was kept constant for each fit. The origin of small Gaussian smearing of inelastic peaks is probably small fluctuations of pressure and temperature during data collection, as well as possible pressure gradients and non-systematic instrumental errors. This model function was fitted to the IXS spectra, utilizing a standard χ^2 minimization routine. In the case of

loading with LiF we also saw its LA phonon, but the contribution was clearly apparent due to the higher sound speed in LiF. Transverse phonon modes of the $Fe_{0.78}Ni_{0.22}$ alloy cannot be distinguished in the experiment, and only longitudinal sound velocities could be obtained directly from IXS measurements. Six to ten $E(Q)$ (for Q from 3 to 12.6 nm^{-1}) values were used to describe the LA phonon dispersions at every measured P, T condition.
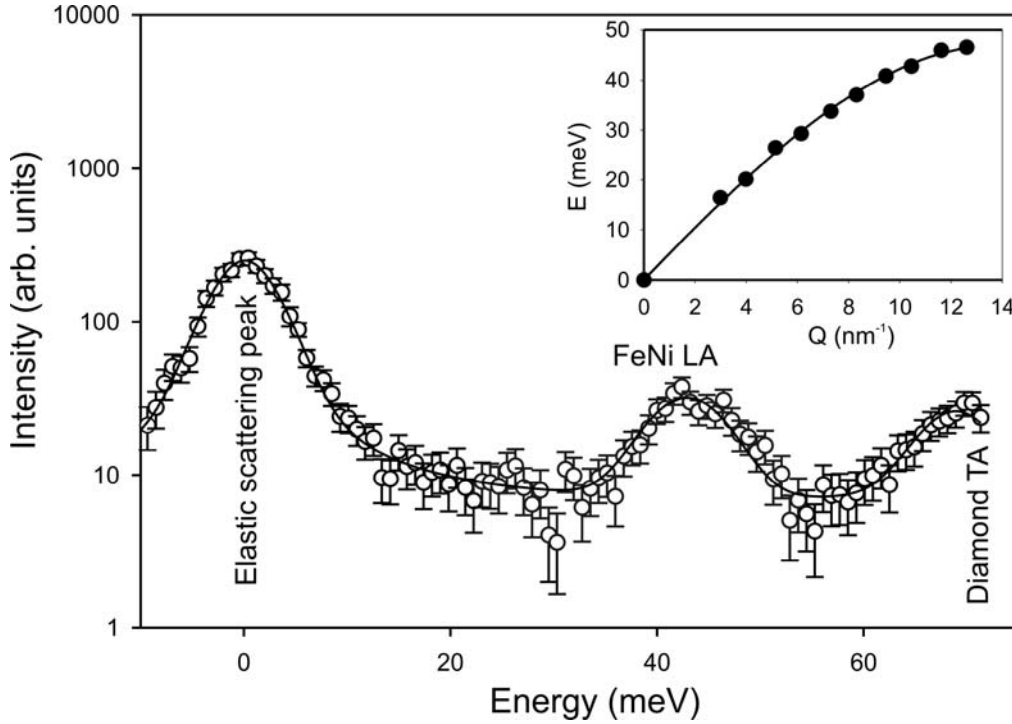
Fig. 3.3.3. Representative IXS spectrum of polycrystalline $Fe_{0.78}Ni_{0.22}$ alloy, collected at 71.7 GPa and 715 K (Q=10.45 nm^{-1}). Inset: an example of the sinusoidal fit to the experimental $E(Q)$ relation.

The procedure of the data collection and reduction is described in details in the previous chapter of the present work (see section 2.2). The values for compressional wave velocities were extracted from the sinusoidal fit to the $E(Q)$ relation (see Fig. 2.2.3 or Fig. 3.3.3, inset) using Eq. 2.24 (see section 2.2). Since no evidence of anisotropy was observed by XRD, the sample was consider as an isotropic polycrystalline material, and the shear sound velocities V_S were extracted according to

the Eq. 2.25 (see section 2.2). In the equation the isothermal (instead of adiabatic) bulk modulus was used. Numerical estimates show that the difference between K_T and K_S in our case is negligible (less than 2 %). Values of the isothermal bulk modulus K for a given density ρ were calculated from measured EoS parameters (see above). The values of other generally used isotropic elastic moduli (shear modulus G, Young's modulus E, and Poisson's ratio ν) could be easily calculated and are listed in table 3-3 along with V_P and V_S values.

Table 3-3. Aggregate longitudinal and transverse velocities, bulk, shear, Young's moduli and Poisson ratio of *fcc* $Fe_{0.78}Ni_{0.22}$ alloy as obtained from IXS and x-ray diffraction measurements.

	P, GPa	ρ, g/cm^3	V_P, km/s	V_S, km/s	K, GPa	G, GPa	ν	E, GPa
300 K	12.4 (0.7)	8.74	6.579 (0.3)	3.675 (0.3)	221 (2)	118 (3)	0.2733	301
	20.4 (1.0)	9.04	6.994 (0.2)	3.877 (0.2)	258 (2)	136 (3)	0.2757	347
	30.4 (1.5)	9.37	7.348 (0.2)	4.095 (0.2)	302 (3)	157 (4)	0.2783	402
	35.3 (1.8)	9.52	7.293 (0.4)	3.797 (0.3)	323 (2)	137 (3)	0.3141	361
	40.6 (2.0)	9.67	7.545 (0.4)	3.729 (0.3)	346 (3)	135 (3)	0.3281	357
	65.9 (2.1)	10.31	8.557 (0.4)	4.691 (0.3)	452 (4)	227 (2)	0.2496	583
715 K	21.5 (0.6)	8.997	6.392 (0.3)	2.981 (0.2)	261 (3)	80 (2)	0.2984	218
	37.1 (0.8)	9.457	7.428 (0.4)	3.912 (0.3)	329 (3)	145 (3)	0.2650	379
	52.0 (1.3)	9.857	7.783 (0.4)	3.948 (0.3)	392 (3)	154 (3)	0.2771	408
	54.3 (1.2)	9.945	7.692 (0.4)	3.743 (0.3)	403 (4)	139 (3)	0.2885	375
	71.7 (1.7)	10.35	8.315 (0.4)	4.179 (0.3)	474 (4)	181 (3)	0.2798	481

Sound wave velocities, plotted against density, are shown in Figs. 3.3.4 – 3.3.6. The data for *fcc* $Fe_{0.78}Ni_{0.22}$ are in good agreement with those for ε–iron and iron-nickel alloy measured by Lin et al. (2003) (Fig. 3.3.4). The sound velocities for

pure *hcp*-Co and Ni are systematically lower at the same density. This difference cannot be explained by the atomic mass difference only, implying that simple mass corrections to the alloys elastic properties are invalid.
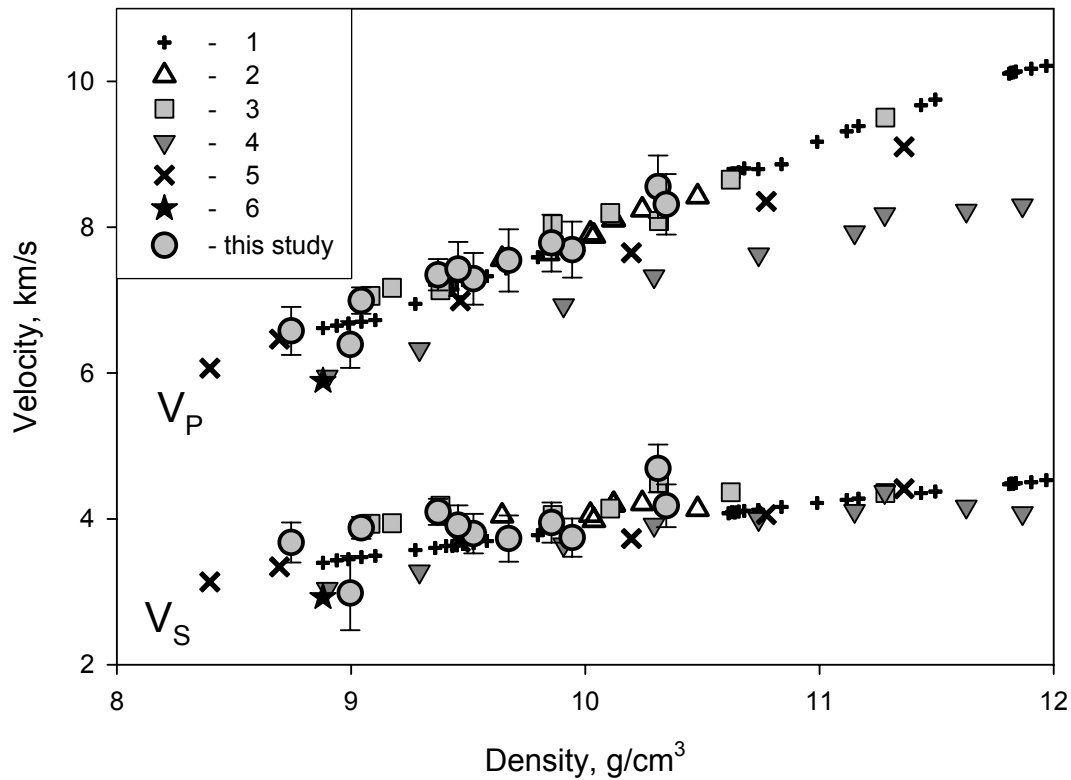

Fig. 3.3.4. Sound velocities of $Fe_{0.78}Ni_{0.22}$ alloy at ambient and high temperature (filled circles) in comparison with data for pure ε-iron: 1 – Dubrovinsky et al. (2001b), 2 – Lin et al. (2005), 3 – Antonangeli et al. (2004), *hcp* Co – 4 (Antonangeli et al., 2005), $Fe_{0.87}Ni_{0.13}$ alloy – 5 (Lin et al., 2003) and 6 – sound wave velocities for pure *fcc* Ni at ambient conditions.

The well-known linear relation between longitudinal velocities and density (so called "Birch's law") (Birch, 1961) that is usually used in geosciences for extrapolations to the Earth's inner core conditions is generally satisfied within the uncertainties of our measurements. Present IXS study shows no detectable difference between room and high temperature results when normalized to density (Fig. 3.3.5).
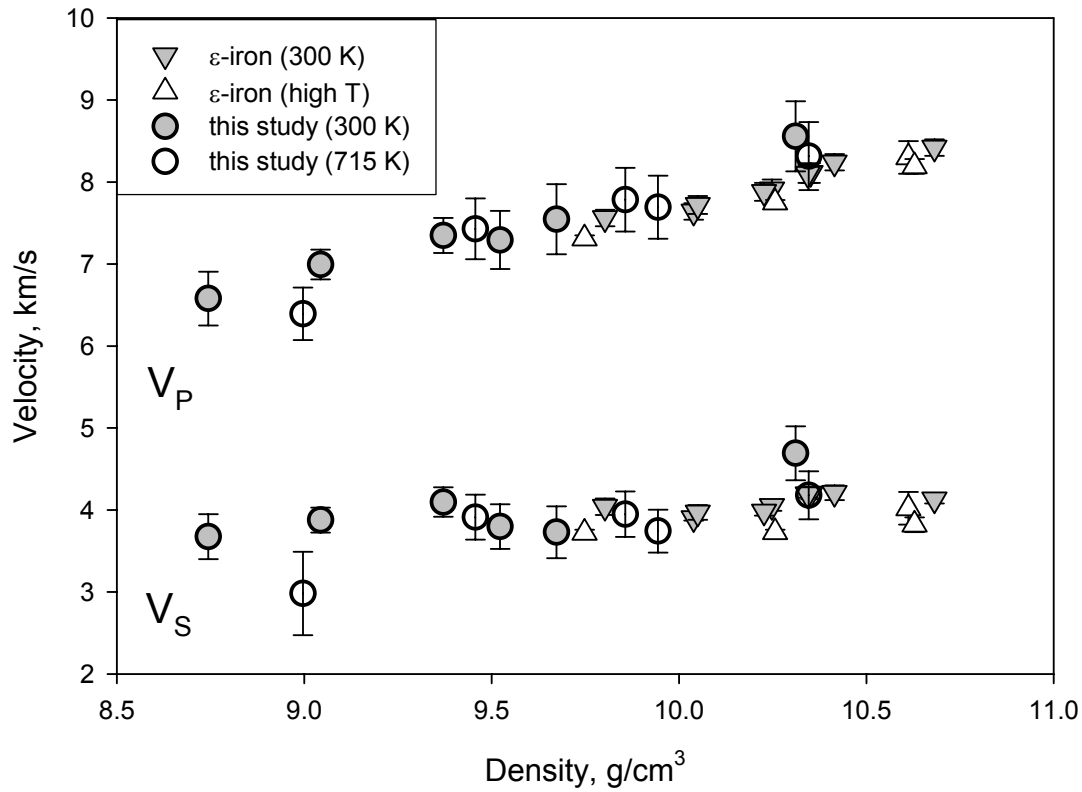
Fig. 3.3.5. Sound velocities of $Fe_{0.78}Ni_{0.22}$ alloy at ambient and high temperature in comparison with high and room temperature data for ε-iron (Lin et al., 2005).

The only exception is one high-temperature point at pressure 21.5 GPa (corresponding to the density ~9 g/cm^3), which is notably lower. This point could accidentally fall into narrow pressure and temperature region with anomalous compressibility in FeNi alloy also known as the *invar effect* (Dubrovinsky et al., 2001a) and thus the elastic behaviour of *fcc* $Fe_{0.78}Ni_{0.22}$ alloy at low pressure (< 25 GPa) region require additional studies. The absence of a significant temperature effect on V_P agrees with theoretical calculations (Steinle-Neumann et al., 2001): even at temperatures about 4000 K, longitudinal sound wave velocities in ε-iron are thought to decrease only by 2-3% (Fig. 3.3.6). At T < 1000 K the temperature effect is

probably not detectable with the present experimental accuracy. In contrast to this, a recent nuclear-resonant inelastic x-ray scattering study (Lin et al., 2005) reported that ε-iron does not follow Birch's law at high temperatures, and that sound velocities significantly decrease with temperature for a given density. Present results could not confirm such anomaly for Fe-Ni alloy in studied pressure – temperature range.
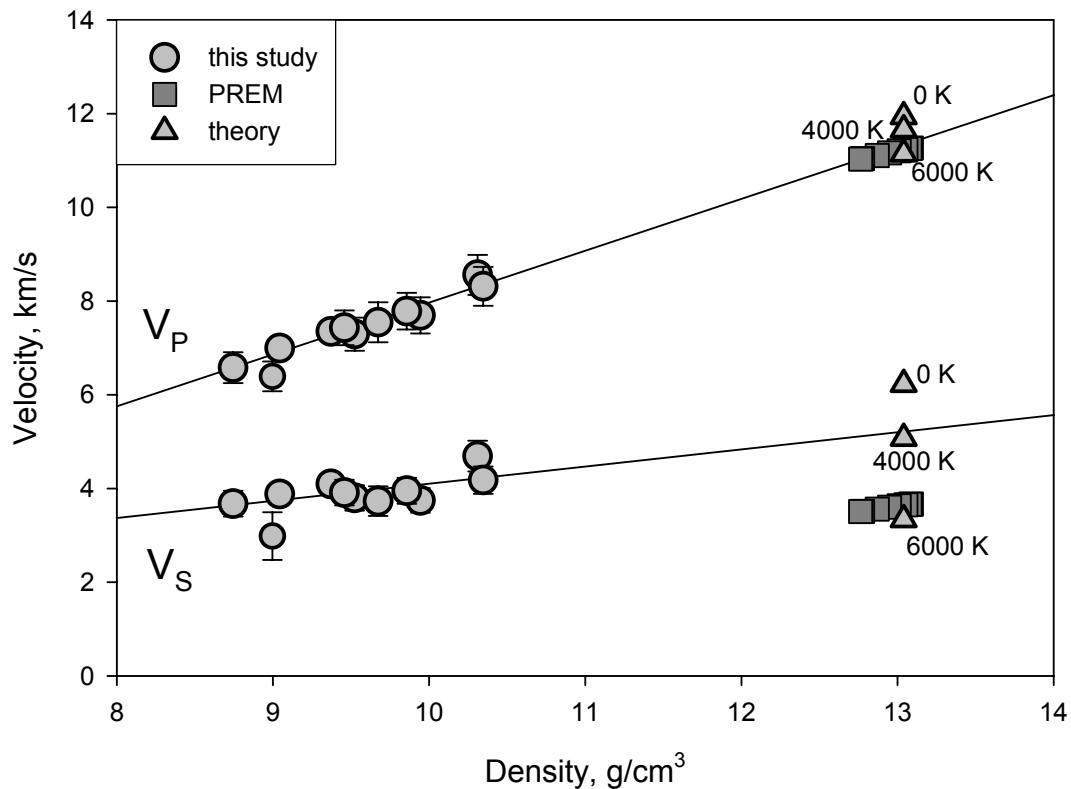
Fig. 3.3.6. The present study (line shows linear fit to the data for $Fe_{0.78}Ni_{0.22}$ extended to the inner core conditions) in comparison with the seismic observations (PREM) (Dziewonski and Anderson, 1981) and calculated sound wave velocities for ε-iron at different temperatures (Steinle-Neumann et al., 2001).

When extrapolate current data to Earth's inner core conditions and compare with PREM (Dziewonski and Anderson, 1981), almost no difference can be seen in longitudinal wave velocities, but V_S is significantly higher than the values expected in

Earth's core (Fig. 3.3.6). If we assume similar temperature corrections as for pure ε-iron (Steinle-Neumann et al., 2001), both V_P and V_S would be below the PREM model for *fcc* $Fe_{0.78}Ni_{0.22}$ alloy. Could this difference be attributed to the presence of "light" elements, such as oxygen or sulphur, in the inner core? It is known that the density of the core is somewhat lower than what is expected for pure iron or iron-nickel alloy at corresponding conditions (Dziewonski and Anderson, 1981; Dubrovinsky et al., 2000b). Incorporation of a few percent of "light" elements to the core could solve the problem. At the same time "light" elements would influence elastic properties of the core, and also increase sound velocities. For example, numeric estimations for addition of silicon in form of FeSi-alloy to pure iron would result in decreasing density and increasing sound wave velocities (Lin et al., 2003; Steinle-Neumann et al., 2001).

Previous studies (Mao et al., 2005; Huang et al., 1992) in combination with the present work show that there is still no unambiguous answer about phase stability fields of *bcc*, *fcc* and *hcp* structures of FeNi alloys with different content of Ni under high pressure. It is clear that even small changes in Ni content result in dramatic changes of the *fcc* stability field. In present case (22 at. % of Ni) the stability field of the *fcc* phase is larger than was reported by Mao et al. (2005) for $Fe_{0.95}Ni_{0.05}$, $Fe_{0.85}Ni_{0.15}$, $Fe_{0.80}Ni_{0.20}$ and by Huang et al. (1992) for $Fe_{0.70}Ni_{0.30}$.

In order to conclude, in the present section x-ray inelastic scattering measurements allowed the longitudinal acoustic wave velocity to be measured that gives, combined with the measured EoS, the full isotropic elasticity of the material. And no significant deviation of the elastic properties from those of pure ε–iron was observed and furthermore no deviation from Birch's law. Although the bulk elasticity of *fcc* Fe-Ni alloy and ε–Fe seem to be very similar, the elastic anisotropy of

hexagonal and cubic phases should be quite different (Cohen et al., 1997). If the metal phase in the inner core is not hexagonal, but cubic (or a mixture of the two phases exists), seismic anisotropy may provide a better way to discriminate between them two.

Conclusions

The main goals of this study were to extend gigahertz ultrasonic interferometry (GUI) into the simultaneous high–pressure high-temperature regime, and to apply this instrument in new studies of geophysically relevant materials. The problem of magneto-elastic coupling in transition metal monoxides including FeO, MnO, as well as elasticity of metals (iron-nickel alloy) have been investigated using several techniques, including GUI, Mössbauer spectroscopy (MS), and inelastic x-ray scattering.

The first series of the experiments carried out within the Project, before the high-temperature assembly was developed, resulted in determination of the complete elastic tensor of wüstite (Fe_xO) to 10 GPa (Kantor et al., 2004a). This phase is an end-member of the MgO-FeO solid solution, considered to be the second most abundant phase in the lower mantle at 660-2890 km depth. This study extended previous data to 3 GPa (Jackson et al., 1990), and revealed a new interesting behaviour of elastic constants of wüstite related to magnetoelastic coupling in the 4-6 GPa pressure range. In agreement with previous studies, dC_{44}/dP is negative, reducing the value of C_{44} by 20% at 10 GPa. A discontinuity in the pressure derivatives of C_{11} and C_{12} at 4.7 ± 0.2 GPa are consistent with the pressure at which magnetic ordering starts, as observed by high-pressure MS in a ^{57}Fe-enriched sample of $Fe_{0.95}O$. The results indicate that an

intermediate magnetically ordered but still cubic phase of $Fe_{0.94}O$ exists at room temperature and in pressure range from ~5 GPa to ~17 GPa.

The magneto-elastic coupling observed in $Fe_{0.94}O$ by GUI experiment was investigated further using neutron diffraction technique at low temperature and ambient pressure (Kantor et al., 2005b). The obtained results demonstrate that structural distortion in wüstite occurs at much lower temperature (about 160 K) than the Néel transition (202 K). Therefore, magnetically ordered cubic phase of Fe_xO that was observed at high pressures seems to exist also at ambient pressure at a large temperature range. This result implies that existing theories which directly links of magnetostriction and spontaneous magnetization in *fcc* ferromagnets monoxides are not valid at least for FeO, and probably also for other transition metal monoxides.

The high-pressure elastic behaviour of wüstite was also studied using inelastic x-ray scattering technique up to 20 GPa. The experiment was combined with x-ray diffraction in diamond anvil cell, which provided data on unit cell volume and, hence, density as a function of pressure. The cubic-to-rhombohedral phase transformation was observed between 17.6 GPa and 19.8 GPa.

The bulk modulus of Fe_xO determined from IXS and compressibility measurements coincide within the experimental error ($K_T = 162 \pm 3$ GPa). However, *K'* values differ significantly (5.3 ± 0.2 for IXS data versus 1.79 ± 0.9 for diffraction data). At pressures about 17 GPa (just below the cubic-to-rhombohedral transition) the difference in bulk modulus reaches ~40 GPa, at least one order of magnitude larger than the associated experimental uncertainty. This unusual compressional behaviour of Fe_xO can be explained by anelastic relaxation, which in the case of wüstite at high pressure is enormously strong and could not be considered as a negligible effect *a priori*.

The main implication for high-pressure mineral physics is that high-frequency and phonon dispersion measurements could give effective elastic moduli different from those seen by low-frequency seismic waves in geophysical observations. In case of any internal structural relaxations, associated with atomic diffusion, a certain characteristic time τ is required to reach an equilibrium state. If the inverse sampling frequency is smaller than τ, only elastic relaxation occurs, and the measured bulk modulus and K' would be higher, that those measured for inverse frequency larger that τ. All materials with significant amount of defects and all solid solutions and alloys could possess anelastic relaxation and Fe_xO is probably one of the extreme cases.

A method for measuring inelastic x-ray scattering in externally heated diamond anvil cells has been developed. The high-pressure and temperature elasticity investigation was performed on a FeNi-alloy. It was the first *in situ* measurement of the longitudinal sound velocity V_P in *fcc* $Fe_{0.78}Ni_{0.22}$ alloy at high pressure and temperature by means of inelastic x-ray scattering from polycrystalline material (Kantor et al., 2007a). The composition was chosen as one of the high-end probable Ni-concentration in the Earth's core in order to evaluate the strongest possible effect of it on the bulk sound velocities in the alloy. Combined with the determination of the EoS by x-ray diffraction, the transverse velocities V_S were derived as well.

Powder x-ray diffraction revealed that $Fe_{0.78}Ni_{0.22}$ alloy is stable in the *fcc* phase throughout the whole studied P, T range. Sound velocities in $Fe_{0.78}Ni_{0.22}$ alloy do not significantly deviate from those of pure ε−iron and furthermore no deviation from Birch's law (linear relation between density and longitudinal seismic velocity) for the studied material was observed. Although the bulk elasticity of *fcc* Fe-Ni alloy and ε−Fe seem to be very similar, the elastic anisotropy of hexagonal and cubic

phases should be quite different (Cohen et al., 1997). If the metal phase in the inner core is not hexagonal, but cubic (or a mixture of the two phases exists), anisotropy may provide a better way to discriminate between them two.

The high *P-T* gigahertz ultrasonic system was developed for the purpose of determining the full elastic tensor of single-crystals under high pressure and temperature simultaneously. The pressure is limited now only by preserving single-crystal at high pressure and maintaining the parallel-faced sample inside a DAC. GUI experiments were conducted at pressures up to 10 GPa. In the future, loading with a helium pressure-transmitting medium could increase this pressure limit, and use of neon pressure medium would allow high-temperature experiments. With the increasing temperature it was found that the intensity of the acoustic signal decreases. This problem can be potentially solved using additional high-frequency amplifier, which increases the intensity in several times.

GUI system is also helpful in measuring the bulk elasticity of nanocrystalline and liquid materials but the problem of thickness determination should be solved beforehand. Measuring sound velocities in metals proved to be challenging, and is yet unsuccessful. Despite concerted effort to produce polished facets, the malleability of metal results in a thin distorted, possibly polycrystalline layer on the surface. Because the acoustic waves at GHz-frequencies have near-optical wavelengths (1-10 mm), any disturbance of the crystalline solid on this scale scatters or absorbs the incident acoustic wave-field. In the future, it may be possible to use ion beams or chemical etching to produce crystalline surfaces on metals for high-frequency acoustic measurements.

The GHz-ultrasonic interferometry technique is promising for many geologically important applications, but is quite complicated for routine usage. The

very high requirements for the sample quality and the complicated assembly (custom buffer rods and transducers, which are not available commercially and have been prepared by magnetron sputtering) are the primary limits in the application of GUI system, preventing wider employment of the technique at this time. There are currently only three GHz-systems worldwide: in Bayreuth (BGI), at GFZ-Potsdam by H.J. Reichmann and at Northwestern University (Evanston, IL) by S.D. Jacobsen. The technological challenges associated with the technique are also balanced by the novelty of results possible only with GUI. The technique holds exciting potential for the future of mineral physics.

Acknowledgments

Finally, I would like to acknowledge many people who participated in these studies. First of all, Leonid Dubrovinsky and Steven Jacobsen who provided their support and advice throughout my PhD studies. My teachers, V.S. Urusov, D.Yu. Pushcharovsky, Yu.K. Egorov-Tismenko from Moscow State University, who guided my scientific interests and skills during my undergraduate and Masters studies. Special thanks to H.-J. Reichmann who was always open for any questions and discussions. Many people at the synchrotron in France assisted me in performing the experiments, and I would like to thank here also Michael Krisch, Alexei Bossak, and Michael Hanfland. I want to thank all the scientific employees of Bayerisches Geoinstitut for their help and assistance. Special thanks to the technical staff at the University of Bayreuth, Hubert Schulze, Klaus Müller, Georg Herrmannsdörfer, Heinz Fischer and Stefan Übelhack for their technical ingenuity – mein herzlicher Dank! Ohne Eure Hilfe wäre diese Arbeit nicht möglich gewesen. Vielen Dank auch an Detlef Krauße für die Hilfe bei zahlreichen Computerproblemen, an Petra Buchert, Lydia Kison-Herzing und Stefan Keyssner die mir bei vielen organisatorischen Schwierigkeiten geholfen haben.

Bibliography

Abramson, E. H., Brown, J. M., and Slutsky, L. J. Applications of impulsive stimulated scattering in the Earth and planetary sciences. Annu. Rev. Phys. Chem. **50**, 279–313 (1999).

Agee, C. B. Phase transformations and seismic structure in the upper mantle and transition zone. In: *Ultrahigh-Pressure Mineralogy: Physics and Chemistry of the Earth's Deep Interior*, edited by Hemley, R. J. Mineralogical Society of America, Washington, D.C., pp. 165-203 (1998).

Akimoto, S., and Fujisawa, H. Olivine-spinel transition in system Mg_2SiO_4-Fe_2SiO_4 at 800°C. Earth Planet. Sci. Lett. **1**, 237-240 (1966).

Alfe, D., Price, G. D., and Gillan, M. J. Thermodynamics of hexagonal-close-packed iron under Earth's core conditions. Phys. Rev. B **64**, 045123,1 − 045123,16 (2001).

Anderson, D. L. Temperature and pressure derivatives of elastic constants with application to the mantle. J. Geophys. Res. **93**, 4688-4700 (1988).

Anderson, D. *Theory of Earth.* Blackwell Scientific Publications, Oxford, 366 pp. (1989).

Anderson, D. L. *New theory of the Earth*. University Press, Cambridge, 384 pp. (2007).

Anderson, D. L. and Bass, J. D. Transition region of Earth's upper mantle. Nature **320**, 321-328 (1986).

Anderson, O. L. An accurate determination of the equation of state by ultrasonic measurements. In: *Progress in Very High Pressure Research*, ed. by Bundy, F. P., Hibbard, W. R., and Strong, H. M. Wiley, New York, pp. 10-15 (1961).

Andrault, D., Fiquet, G., Kunz, M., Visocekas, F., and Häusermann, D. The orthorhombic structure of iron: an in situ study at high-temperature and high-pressure, Science **278**, 831-834 (1997).

Angel, R. J. Equations of state. In: *High-pressure and high-temperature crystal chemistry*, vol. 41, edited by Hazen, R. M., and Downs, R.T. MSA, p. 35-60 (2000).

Antonangeli, D., Occelli, F., Requardt, H., Badro, J., Fiquet, G., and Krisch, M. Elastic anisotropy in textured hcp-iron to 112 GPa from sound wave propagation measurements. Earth and Planet. Sci. Lett. **225**, 243-251 (2004).

Antonangeli, D., Krisch, M., Fiquet, G., Badro, J., Farber, D. L., Bossak, A., and Merkel, S. Aggregate and single-crystalline elasticity of hcp cobalt at high pressure. Phys. Rev. B **72**, 134303,1-134303,7 (2005).

Arlt, T., Bermejo, M., Blanco, M. A., Gerward, L., Jiang, J. Z., Olsen, J. S., and Recio, J. M. High-pressure polymorphs of anatase TiO2. Phys. Rev. B **61**, 14414-14419 (2000).

Ashcroft, N.W., and Mermin, N.D. *Solid State Physics*. Saunders College Publishing, Orlando, USA, pp. 826 (1976).

Baer, B. J., Brown, J. M., Zaug, J. M., Schiferl, D., and Chronister, E. L. Impulsive stimulated scattering in ice VI and ice VII. J. Chem. Phys. **108**, 4540-4544 (1998).

Badro, J., Struzhkin, V. V., Shu, J., Hemley, R. J., Mao, H. K., Kao, C. C., Rueff, J-P., and Shen, G. Magnetism in FeO at Megabar Pressures from X-Ray Emission Spectroscopy. Phys. Rev. Lett. **83**, 4101-4104 (1999).

Barnett, J. D., and Hall, H. T. High pressure – high temperature, X-ray diffraction apparatus. Rev. Sci. Instrum. **35**, 175-182 (1964).

Bass, J. D., and Anderson, D. L. Composition of the upper mantle: Geophysical tests of two petrological models. Geophys. Res. Lett. **11**, 237-240 (1984).

Bassett, W. A., Takahashi, T., and Stook, P. W. X-ray diffraction and optical observations on crystalline solids up to 300 kbar. Rev. Sci. Instrum. **38**, 37-42 (1967).

Bassett, W. A., and Brody, E. M. Brillouin scattering: A new way to measure elastic moduli at high pressures. In: *High-Pressure Research, Applications in Geophysics*. Academic Press, New York, pp. 519-531 (1977).

Bassett, W. A., Reichmann, H.-J., Angel, R. J., Spetzler, H., and Smyth, J. R. New diamond anvil cells for gigahertz ultrasonic interferometry and X-ray diffraction. Am. Miner. **85**, 283-287 (2000).

Belonoshko, A. B., Ahuja, R., and Johansson, B. Stability of the body-centred-cubic phase of iron in the Earth's inner core. Nature **424**, 1032-1034 (2003).

Berthon, J., Revcolevschi, A., Morikawa, H., and Touzelin, B. Growth of wüstite $Fe_{1-x}O$ crystals of various stoichiometries. J. Cryst. Growth **47**, 736-738 (1979).

Bina, C. R., and Wood, B. J. Olivine-spinel transitions: Experimental and thermodynamic constraints and implications for the nature of the 400-km discontinuity J. Geophys. Res. **92**, 4853-4866 (1987).

Birch, F. Elasticity and constitution of the earth's interior. J. Geophys. Res. **57**, 227-286 (1952).

Birch, F. Composition of the Earth's Mantle. Geophys. J. R. Astron. Soc. **4**, 295-311 (1961).

Boehler, R. Temperatures in the Earth's core from melting-point measurements of iron at high static pressures. Nature **363**, 534-536 (1993).

Bock, G. Synthetic seismogram images of upper mantle structure: No evidence for a 520-km discontinuity. J. Geophys. Res. **99**, 15843-15851 (1994).

Bottke, W. F., Nesvorny, D., Grimm, R. E., Morbidelli, A., and O'Brien, D. P. Iron meteorites as remnant of planetesimals formed in the terrestrial planet region. Nature **439**, 821-824 (2006).

Breger, L., Romanowicz, B., and Rousset, S. New constraints on the structure of the inner core from P'P'. Geophys. Res. Lett. **27**, 2781-2784 (2000).

Bridgman, P. W. Compressibility of thirty metals as a function of pressure and temperature. Proc. Amer. Acad. **58**, 166-242 (1923).

Bridgman, P. W. *The Physics of High Pressure,* Chapter 6. G. Bell and Sons, London, pp. 149-188 (1958).

Brillouin, L. Diffusion de la lumi`ere et des rayons X par un corps transparent homog`ene. Ann. Phys. (Paris) **17**, 88-122 (1921).

Brown, J. M., and McQueen, R. G. Phase transitions, Gruneisen parameter, and elasticity for shocked iron between 77 and 400 GPa. J. Geophys. Res. B **91 (7)**, 7485–7494 (1986).

Brown, J. M., Slutsky, L. J., Nelson, K. A., and Cheng, L.-T. Single-crystal elastic constants for San Carlos peridotite: An application of impulsive stimulated scattering. J. Geophys. Res. **95**, 9485-9492 (1989).

Brown, J. M., Abramson, E. H., and Angel, R. J. Triclinic elastic constants for low albite. Phys. Chem. Minerals **33**, 256-265 (2006).

Brugger, K. Pure modes for elastic waves in crystals. J. Appl. Phys. **36**, 759-768 (1965).

Bullen, K. E. The problem of earth's density variation. Bull. Seis. Soc. Am. **30**, 235-250 (1940).

Bullen, K.E. Cores of the terrestrial planets. Nature **243,** 68-70 (1973).

Burkel, E. Phonon spectroscopy by inelastic x-ray scattering. Rep. Prog. Phys. **63**, 171-232 (2000).

Chai, M., Brown, J. M., and Slutsky, L. T. The elastic constants of pyrope-grossular-almandine garnet to 20 GPa. Geophys. Res. Lett. **24**, 523–526 (1997a).

Chai, M., Brown, J. M., and Slutsky, L. T. The elastic constants of an aluminous orthopyroxene to 12.5 GPa. J. Geophys. Res. **102**, 14779–14785 (1997b).

Chen, G., Yoneda, A., Getting, I. C., and Spetzler, H. A. Cross pressure and temperature derivatives of selected elastic moduli for olivine from gigahertz ultrasonic interferometry. J. Geophys. Res. **101**, 25161-25171 (1996).

Chen, G., Miletich, R., Mueller, K., and Spetzler, H. A. Shear and compressional mode measurements with GHz ultrasonic interferometry and velocity-composition systematics for the pyrope-almandine solid solution series. Phys. Earth Planet. Interiors **99**, 273-287 (1997).

Cohen, R. E., Stixrude, L., and Wasserman, E. Tight-binding computations of elastic anisotropy of Fe, Xe, and Si under compression, Phys. Rev. B **56**, 8575-8589 (1997).

Cohen, R. E., Gulseren, O., and Hemley, R. J. Accuracy of equation-of-state formulations. Am. Mineral. **85**, 338-344 (2000).

Crowhurst, J. C., Hearn, G. R., Comins, J. D., Every, A. G., and Stoddart, P. R. Surface Brillouin scattering at high pressure: Application to a thin supported gold film. Phys. Rev. B **60**, R14990-R14993 (1999).

Crowhurst, J. C., Goncharov, A. F., Zaug, J. M. Impulsive stimulated light scattering from opaque materials at high pressure. J. Phys.: Condens. Matter. **16**, S1137-S1142, (2004).

Crowhurst, J. C., Goncharov, A. F., and Zaug, J. M. Direct measurements of the elastic properties of iron and cobalt to 120 GPa – implications for the composition of Earth's core. In: *Advanced in high-pressure technology for geophysical applications* edited by Chen, J., Wang, Y., Duffy, T. S., Shen, G., Dobrzhinetskaya, L. F. Elsevier, Amsterdam, pp. 3-23 (2005).

Dewaele, A., Loubeyre, P. and Mezouar, M. Equations of state of six metals above 94 GPa. Phys. Rev. B **70**, 094112,1-094112,8 (2004).

Ding, Y., Liu, H., Somayazulu, M., Meng, Y., Xu, J., Prewitt, C. T., Hemley, R. J., and Mao H. K. Zone-axis X-ray diffraction of single-crystal $Fe_{1-x}O$ under pressure. Phys. Rev. B **72**, 174109,1-174109,6 (2005).

Dorner, B., Burkel, E., and Peisl, J. An X-ray backscattering instrument with very high energy resolution. Nucl. Instrum. Methods A **246**, 450-451 (1986).

Dorner, B., Burkel, E., Illini, Th., and Peisl, J. Z. First measurements of a phonon dispersion curve by inelastic X-ray scattering. Z. Phys. B – Condensed Matter **69**, 179-183 (1987).

Dubretsev, V. A., and Pankov, V. On the composition of the Earth's core. Izv. Phys. Solid Earth **7**, 48-54 (1972).

Dubrovinskaia, N., and Dubrovinsky, L. Whole-cell heater for the diamond anvil cell. Rev. Sci. Instrum. **74**, 3433-3437 (2003).

Dubrovinsky, L. S., and Dubrovinskaia, N. A. High pressure crystallography at elevated temperatures: experimental approach. In: *High-pressure crystallography, Mathematics, Physics and Chemistry* edited by Katrusiak, A. and McMillan, P. Kluwer Academic Publishers, Boston, pp. 393-410 (2003).

Dubrovinsky, L., Dubrovinskaia, N., Saxena, S., and Le Behan, T. X-ray diffraction under non-hydrostatic conditions in experiments with diamond anvil cell:

173

wustite (FeO) as an example. Material Sciences and Engineering A **288**, 187-190 (2000a).

Dubrovinsky, L. S., Saxena, S. K., Tutti, F., and Le Bihan, T. X-ray study of thermal expansion and phase transition of iron at multimegabar pressure. Phys. Rev. Letters **84**, 1720-1723 (2000b).

Dubrovinsky, L. S., Dubrovinskaia, N. A., Abrikosov, I. A., Vennström, M., Westman, F., Carlson, S., Van Schilfgaarde, M., and Johansson, B. Pressure induced invar effect in Fe-Ni alloys. Phys. Rev. Lett. **86**, 4851-4854 (2001a).

Dubrovinsky, L. S., Dubrovinskaia, N. A., and Le Bihan, T. Aggregate sound velocities and acoustic Grueneisen parametr of iron up to 300 GPa and 1200 K. Proc. Natl. Acad. Sci. **98**, 9484-9489 (2001b).

Dubrovinsky, L., Dubrovinskaia, N., Narygina, O., Kantor, I., Kuznetzov, A., Prakapenka, V., Vitos, L., Johansson, B., Mikhaylushkin, A. S., Simak, S. I., and Abrikosov, I. A. Body-centred-cubic iron-nickel alloy in the Earth's core, Science **31**, 1880-1883 (2007).

Duffy, T. S., and Anderson, D. L. Seismic velocities in mantle minerals and the mineralogy of the upper mantle. J. Geophys. Res. **94**, 1895-1912 (1989).

Duffy, T. S., and Ahrens, T. J. Sound velocities at high pressure and temperature and their geophysical implications. J. Geophys. Res. B **97 (4)**, 4503–4520 (1992).

Duffy, T. S., and Ahrens, T. J. The temperature sensitivity of elastic wave velocity at high pressure; new results for molybdenum. Geophys. Res. Lett. **21 (6)**, 473–476 (1994).

Duffy, T. S., and Ahrens, T. J. Compressional sound velocity, equation of state, and constitutive response of shock-compressed magnesium oxide. J. Geophys. Res. **100 (B1)**, 529–542 (1995a).

Duffy, T. S., Zha, C., Downs, R. T., Mao, H.-K., and Hemly, R. J. Elasticity of forsterite to 16 GPa and the composition of the upper mantle. Science **378**, 170-173 (1995b).

Duffy, T. S. and Wang, C. S. Pressure-volume-temperature equations of state. Reviews in Mineralogy **37**, 425-457 (1998).

Duffy, T. S., Shen, G., Heinz, D. L., Shu, J., Ma, Y., Mao H.-K., Hemley, R. J., and Singh, A. K. Lattice strains in gold and rhenium under non-hydrostatic compression to 37 GPa. Phys. Rev. B **60**, 15063-15073 (1999).

Dziewonski, A. M., and Anderson, D. L. Preliminary reference Earth model. Phys. Earth Planet. Inter. **25**, 297-356 (1981).

Encrenaz, T., Bibring, J.-P., and Blanc, M. *The Solar System*. Springer-Verlag, Berlin Heidelberg, 350 pp. (1995).

Every, A. G. Effect of first-order spatial dispersion on phonon focusing: Application to quartz. Phys. Rev. B **36**, 1448-1456 (1987a).

Every, A. G. and McCurdy, A. K. Phonon focusing in piezoelectric crystals. Phys. Rev. B **36**, 1432-1447 (1987b).

Fayer, M. D. Holographic grating generation of ultrasonic waves. Quantum Electronics **22**, 1437-1452 (1986).

Fei, Y., Mao, H.-K., Shu, J., Parthasarathy, G., Bassett. W. A., and Ko, J. Simultaneous high-P, high-T X-ray diffraction study of β-$(Mg,Fe)_2SiO_4$ to 26 GPa and 900 K. J. Geophys. Res. **97**, 4489-4495 (1992).

Fei, Y., and Mao H.-K. In Situ Determination of the NiAs Phase of FeO at High Pressure and Temperature. Science **9**, 1678-1680 (1994).

Fiquet, G., Badro, J., Guyot, F., Requardt, H., and Krisch, M. Sound velocities in iron to 110 gigapascals. Science **291**, 468-471 (2001).

Fiquet, G., Badro, J., Guyot, F., Bellin, Ch., Krisch, M., Antonangeli, D., Requardt, H., Mermet, A., Farber, D., Aracne-Ruddle, C., and Zhang, J. Application of inelastic X-ray scattering to the measurements of acoustic wave velocities in geophysical materials at very high pressure. Phys. Earth Planet. Inter. **143**, 5-18 (2004).

Frost, D. J., and Langenhorst, F. The effect of Al_2O_3 on Fe-Mg partitioning between magnesiowüstite and magnesium silicate perovskite. Earth Planet. Sci. Lett. **199**, 227-241 (2002).

Fujisawa, H. Elastic wave velocities of forsterite and its β-spinel form and chemical boundary hypothesis for the 410-km discontinuity. J. Geophys. Res. **103**, 9591-9608 (1998).

Fukizawa, A., and Kinoshita, H. Shear velocity jump at the olivine-spinel transformation in Fe_2SiO_4 by ultrasonic measurements in situ. J. Phys. Earth **30**, 245-253 (1982).

Gaherty, J. B., Kato, M., and Jordan, T. H. Seismological structure of the upper mantle: A regional comparison of seismic layering. Phys. Earth Planet. Int. **110**, 21-41 (1999).

Gasparik, T. Phase relations in the transition zone. J. Geophys. Res. **95**, 15751-15769 (1990).

Grand, S. P., and Helmberger, D. V. Upper mantle shear structure of North America. Geophys. J. R. Astro. Soc. **76,** 399-438 (1984).

Grimvall, G. *Thermophysical properties of materials.* Elsevier, Stockholm, pp. 27-45 (1999).

Guenzburger, D., and Terra, J. Theoretical study of magnetism and Mössbauer hyperfine interactions in ordered FeNi and disordered fcc Fe-rich Fe–Ni alloys. Phys. Rev. B **72**, 024408,1-024408,9 (2005).

Gwanmesia, G. D., and Liebermann, R. C. Polycrystals of high-pressure phases of mantle minerals: Hot-pressing and characterization of physical properties. In: *High Pressure Research: Application to Earth and Planetary Sciences*, Vol. 3, edited by Syono, Y., and Manghnani, M. H. American Geophysical Union, Washington D.C., pp. 117-135 (1992).

Gwanmesia, G. D., Liebermann, R. C., and Guyot, F. Hot-pressing and characterization of polycrystals of ß-Mg_2SiO_4 for acoustic velocity measurements. Geophys. Res. Lett. **17**, 1331-1334 (1990a).

Gwanmesia, G. D., Rigden, S. M., Jackson, I., and Liebermann, R. C. Pressure dependence of elastic wave velocity for ß-Mg_2SiO_4 and the composition of Earth's mantle. Science **250**, 794-797 (1990b).

Haavik, C., Stolen, S., Hanfland, M., and Catlow, C. R. A. Effect of defect clustering on the high-pressure behaviour of wüstite. High-pressure X-ray diffraction and lattice energy simulations. Phys. Chem. Chem. Phys. **2**, 5333-5140 (2000).

Hausch, G., and Warlimont, H. Single crystalline elastic constants of ferromagnetic face centred cubic Fe-Ni invar alloys. Acta Metallurgica **21**, 401-414 (1973).

Hemley, R. J., and Mao, H. K. In-situ studies of iron under pressure: New windows on the Earth's core. Intern. Geol. Rev. **43**, 1-30 (2001).

Heydemann, L. M., and Houck, J. C. Ultrasonic and dilatometric measurements at very high pressures. In: *Accurate Characterization of the High Pressure Environment*, edited by Lloyd, E. C. National Bureau of Standards Special

Publication 326, Government Printing Office, Washington, D. C., USA, pp. 11-23 (1971).

Hill, R. The elastic behaviour of a crystalline aggregate. Proc. Phys. Soc. London **64**, 349-354 (1952).

Huang, E., Basset, W., and Weathers, M. S. Phase relations in Fe-Ni alloys at high pressures and temperatures. J. Geophys. Res. **93**, 7741-7746 (1988).

Huang, E., Basset, W., and Weathers, M. S. Phase diagram and elastic properties of Fe 30 % Ni alloy by synchrotron radiation. J. Geophys. Res. **97**, 4497-4502 (1992).

Ibach, H., and Lüth, H. *Solid-State Physics, An Introduction to Principles of Materials Science, corrected second printing of the second edition*. Springer-Verlag, Berlin, 164 pp. (1996).

Irifune, T. An experimental investigation of pyroxene-garnet transformation in a pyrolite composition and its bearing on the composition of the mantle. Phys. Earth Planet. Int. **45**, 324-336 (1987).

Irifune, T. Phase transformations in Earth's mantle and subducting slabs; implications for their compositions, seismic velocity and density structures and dynamics. Island Arc **2**, 55-71 (1993).

Isaak, D. G. Elastic properties of minerals and planetary objects. In: *Handbook of elastic properties of solids, liquids and gases* edited by Levy, M. Vol. 3. Academ. Press, San Diego, pp. 325-376 (2001).

Isaak, D. G., Anderson, O. L., and Goto, T. Elasticity of single-crystal forsterite measured to 1700 K. J. Geophys. Res. **94**, 5895–5906 (1989a).

Isaak, D. G., Anderson, O. L., and Goto, T. Measured elastic moduli of single-crystal MgO up to 1800 K. Phys. Chem. Minerals **16**, 704–713 (1989b).

Isaak, D. G., Carnes, J. D., and Anderson, O. L. Elasticity of fused silica spheres under pressure using resonant ultrasonic spectroscopy. J. Acoust. Soc. Am. **104**, 2200-2206 (1998a).

Isaak, D. G., Carnes, J. D., Anderson, O. L., Cynn, H., and Hake, E. Elasticity of TiO_2 rutile to 1800 K. Phys. Chem. Mineral. **26**, 31-43 (1998b).

Ita, J., and Stixrude, L. Petrology, elasticity, and composition of the mantle transition zone. J. Geophys. Res. **97**, 6849-6866 (1992).

Ito, E. The absence of oxide mixture in high-pressure phases of Mg-silicates. Geophys. Res. Lett. **4**, 72-74 (1977).

Ito, E., and Katsura, T. A temperature profile of the mantle transition zone. Geophys. Res. Lett. **16**, 425-428 (1989).

Ito, E., and Takahashi, E. Ultrahigh-pressure phase transformations and the constitution of the deep mantle. In: *High Pressure Research in Mineral Physics*, edited by Manghnani, M. H. and Syono, Y. American Geophysical Union, Washington, D.C., pp. 221-229 (1987).

Jackson, I. Elasticity, composition, and temperature of the Earth's lower mantle: a reappraisal. Geophys. J. Intl. **134,** 291-311 (1998).

Jackson, I., and Niesler, H. The elasticity of periclase to 3 GPa and some geophysical inmplications. In: *Advances in Earth and Planetary Sciences*, Vol. 12, edited by Akimoto, S., and Manghnani, M. N. Center for Academic Publishing, Tokyo, pp. 93-113 (1982).

Jackson, I., Khanna, S. K., Revcolevschi, A., and Berthon, J. Elasticity, shear-mode softening and highpressure polymorphism of wüstite ($Fe_{1-x}O$). J. Geophys. Res. **95**, 21671-21685 (1990).

Jackson, I., and Rigden, S. M. Composition and temperature of the Earth's mantle: Seismological models interpreted through experimental studies of earth materials. In: *The Earth's Mantle: Composition, Structure, and Evolution*, edited by Jackson, I. Cambridge University Press, Cambridge, U.K., pp. 405-460 (1998).

Jackson, J. M., Sinogeikin, S., and Bass, J. D. Sound velocities and elastic properties of γ–Mg_2SiO_4 to 873 K by Brillouin spectroscopy. Am. Min. **85,** 296-303 (2000).

Jacobsen, S. D., Reichmann, H. J., Spetzler, H. A., Mackwell, S. J., Smyth, J. R ., Angel, R. J., and McCammon, C. A. Structure and elasticity of single-crystal (Mg,Fe)O and a new method of generating shear waves for gigahertz ultrasonic interferometry. J. Geophys. Res. **107**, 2037,1-2037,14 (2002a).

Jacobsen, S. D., Spetzler, H. A., Reichmann, H. J., Smyth, J. R., Mackwell, S. J., Angel, R. J., and Bassett, W. A. Gigahertz ultrasonic interferometry at high P and T: new tools for obtaining a thermodynamic equation of state. J. Phys.: Condens. Matter **14**, 11525-11530 (2002b).

Jacobsen, S. D., Smyth, J. R., Spetzler, H. A., Holl, C. A., and Frost, D. J. Sound velocities and elastic constants of iron-bearing hydrous ringwoodite. Phys. Earth Planet. Interiors **143**, 47-56 (2004a).

Jacobsen, S. D., Spetzler, H. A., Reichmann, H. J., and Smyth, J. R. Shear waves in the diamondanvil cell reveal pressure-induced instability in (Mg,Fe)O. Proc. Natl Acad. Sci. USA **101**, 5867-5871 (2004b).

Jacobsen, S. D., Reichmann, H. J., Kantor, A. P., and Spetzler, H. A. A gigahertz ultrasonic interferometer for the diamond anvil cell and high-pressure elasticity of some iron-oxide minerals. In: *Advances in high-pressure technology for*

geophysical applications edited by Chen, J., Wang, Y., Duffy, T. S., Shen, G., and Dobrzhinetskaya, L. F. Elsevier, Amsterdam, pp. 25-49 (2005a).

Jacobsen, S. D., Lin, J. F., Angel, R. J., Shen, G., Prakapenka, V. B., Dera, P., Mao, H. K., and Hemley, R. J. Single-crystal synchrotron X-ray diffraction study of wüstite and magnesiowüstite at lower-mantle pressures. J. Synchrotron Rad. **12**, 577-583 (2005b).

Jamieson, J. C. Diamond cells for X-ray diffraction studies under high pressure. In: *Progress in Very High Pressure Research*, edited by Bundy, F. P., Hibbard, W. R., and Strong, H. M. Wiley, New York, pp. 10-15 (1961).

Jayaraman, A. Diamond anvil cell and high-pressure physical investigations. Rev. of Modern Physics **56**, 65-108 (1983).

Jeanloz, R. and Hazen, R. M. Compression, nonstoichiometry and bulk viscosity of wüstite. Nature **304**, 620-622 (1983).

Kantor, A. P, Jacobsen, S. D., Kantor, I. Y., Dubrovinsky, L. S., McCammon, C. A., Reichmann, H. J., and Goncharenko, I. N. Pressure-induced magnetization in FeO: evidence from elasticity and Mössbauer spectroscopy. Phys. Rev. Lett. **93**, 215502,1-215502,4 (2004a).

Kantor, I. Yu., McCammon, C. A., and Dubrovinsky, L. S. Mössbauer spectroscopic study of pressure induced magnetization in wüstite (FeO). J. Alloys Compd. **376**, 5-8 (2004b).

Kantor, A. P., Dubrovinsky L. S., Dubrovinskai, N. A., Kantor, I. Yu., and Goncharenko, I. N. Phase transitions in MnO and FeO at low temperatures: A neutron powder diffraction study. J. Alloys Compounds **402**, 42-45 (2005a).

Kantor, I. Yu., Dubrovinsky L. S., and McCammon C. A. Mössbauer spectroscopy at elevated pressures and temperatures: Spin transition in $(Mg_{0.8}Fe_{0.2})O$

ferropericlase. Proceedings of the Joint 20th AIRAPT – 43rd EHPRG International Conference on High Pressure Science and Technology, T5-P101, (2005b).

Kantor, A. P., Kantor, I. Yu., Kurnosov, A. V., Kuznetsov, A. Yu., Dubrovinskaia, N. A., Krisch, M., Bossak, A. A., Dmitriev, V. P., Urusov, V. S., Dubrovinsky, L. S. Sound wave velocities of fcc Fe-Ni alloy at high pressure and temperature by mean of inelastic X-ray scattering. Phys. Earth Planet. Int., *in press* (2007a).

Kantor, I. Yu., Dubrovinsky, L., McCammon, C., Dubrovinskaia, N., Goncharenko, I., Kantor, A. P., Kuznetsov, A., and Crichton, W. FeO and MnO high-pressure phase diagrams: relations between structural and magnetic properties. Phase Transition **80**, 1151-1163 (2007b).

Kato, M., and Jordan, T. H. Seismic structure of the upper mantle beneath the western Philippine Sea. Phys. Earth Planet. Int. **110,** 263-283 (1999).

Katsura, T., and Ito, E. The system Mg_2SiO_4-Fe_2SiO_4 al high pressure and temperatures: Precise determinations of stabilities of olivine, modified spinel and spinel. J. Geophys. Res. **94,** 15663-15670 (1989).

Kinoshita, H., Hamaya, N., and Fujisawa, H. Elastic properties of single crystal NaCl under high pressures to 80 kbar. J. Phys. Earth **27**, 337-350 (1979).

Kinsland, G. L. and Basset, W. A. Modification of the diamond anvil cell for measuring strain and the strength of materials at pressures up to 300 kilobars. Rev. Sci. Instrum. **47**, 130-133 (1976).

Kinsland, G. L. and Basset, W. A. Strength of MgO and NaCl polycrystals to confining pressures of 250 kbar at 25 °C. J. Appl. Phys. **48**, 978-985 (1977).

Klotz, S. Phonon dispersion curves by inelastic neutron scattering to 12 GPa. Z. Kristallogr. **216**, 420-429 (2001).

Klotz, S. and Braden, M. Phonon Dispersion of bcc Iron to 10 GPa. Phys. Rev. Lett. **85,** 3209-3212 (2000).

Klotz, S., Rousse, G., Strässle, Th., Bull, C. L., and Guthrie, M. Nuclear and magnetic structure of magnetite under pressure to 5.3 GPa and at low temperatures to 130 K by neutron scattering. Phys. Rev. B **74**, 0124101-0124104 (2006).

Krisch, M. Status of phonon studies at high pressure by inelastic x-ray scattering. J. Raman Spectroscopy **34**, 628-632 (2003).

Krisch, M. H., Mermet, A., San Miguel, A., Sette, F., and Masciovecchio, C. Acoustic-phonon dispersion in CdTe at 7.5 GPa. Phys. Rev. B **56**, 8691-8694 (1997).

Kung, J., Li, B., Weidner, D. J., Zhang, J., and Liebermann, R. C. Elasticity of $(Mg_{0.83},Fe_{0.17})O$ ferropericlase at high pressure: ultrasonic measurements in conjunction with X-radiation techniques. Earth Planet. Sci. Lett. **203**, 557-566 (2002).

Lauterbach, S., McCammon, C. A., van Aken, P., Langenhorst, F., and Seifert, F. Mössbauer and ELNES spectroscopy of $(Mg,Fe)(Si,Al)O_3$ perovskite: a highly oxidised component of the lower mantle. Contrib. Mineral. Petrol. **138**, 17-26 (2000).

LeFevre, L. V., and Helmberger, D. V. Upper mantle *P* velocity structure of the Canadian shield. J. Geophys. Res. **94**, 17749-17765 (1989).

Li, B., Gwanmesia, G. D., and Liebermann, R. C. Sound velocities of olivine and beta polymorphs of Mg_2SiO_4 at Earth's transition zone pressures. Geophys. Res. Lett. **23,** 2259-2262 (1996a).

Li, B. Jackson, I., Gasparik, T., and Liebermann, R. C. Elastic wave velocity measurement in multi-anvil apparatus to 10 GPa using ultrasonic interferometry. Phys. Earth Planet. Int. **98**, 79-91 (1996b).

Li, B., Liebermann, R. C., and Weidner, D. J. Elastic moduli of wadsleyite (*ß*-Mg$_2$SiO$_4$) to 7 Gigapascals and 873 Kelvin. Science **281,** 675-677 (1998a).

Li, B., Chen, C., Gwanmesia, G. D., and Liebermann, R. C. Sound velocity measurements at mantle transition zone conditions of pressure and temperature using ultrasonic interferometry in multianvil apparatus. In: *Properties of Earth and Planetary Materials at High Pressure and Temperature*, edited by Manghnani, M. H. and Yogi, T. American Geophysical Union, Washington D.C., pp. 41-61 (1998b).

Li, B., Liebermann, R. C., Weidner, D. J. *P–V–V$_P$–V$_S$–T* measurements on wadsleyite to 7GPa and 873 K: implications for the 410 km seismic discontinuity. J. Geophys. Res. **106 (B12)**, 30575–30591 (2001).

Li, B., Kung, J., and Liebermann, R. C. Modern techniques in measuring elasticity of Earth materials at high pressure and high temperature using ultrasonic interferometry in conjunction with synchrotron X-radiation in multi-anvil apparatus. Phys. Earth Planet. Inter. **143/144,** 559-574 (2004).

Liebermann, R. C., Chen, G., Li, B., Gwanmesia, G. D., Chen, J., Vaughan, M. T., and Weidner, D. J. Sound velocity measurements in oxides and silicates at simultaneous high pressures and high temperatures using ultrasonic techniques in multi-anvil apparatus in conjunction with synchrotron X-radiation determination of equation of state. Rev. High Pressure Sci. Technol. **7**, 75-78 (1998).

Liebermann, R. C., and Li, B. Elasticity al high pressures and temperatures. In: *Ultrahigh-Pressure Mineralogy: Physics and Chemistry of the Earth's Deep Interior*, edited by Hemley, R. J. Mineralogical Society of America, Washington, D. C., pp. 459-492 (1998).

Lin, J.-F., Heinz, D. L., Campbell, A. J., Devine, J. M., and Shen, G. Iron-silicon alloy in Earth's core? Science **295**, 313-315 (2002).

Lin, J.-F., Struzhkin, V. V., Sturhahn, W., Huang, E., Zhao, J., Hu, M. Y., Alp, E. E., Mao, H. K., Boctor, N., and Hemly, R. J. Sound velocities of iron-nickel and iron-silicon alloys at high pressures. Geophys. Res. Lett. **30**, 21121-21124 (2003).

Lin, J.-F., Sturhahn, W., Zhao, J., Shen, G., Mao, H. K., and Hemly, R. J. Sound velocities of hot dense iron: Birch's law revised. Science **308**, 1892-1894 (2005).

Lines, M. E. Antiferromagnetism in the face-centered cubic lattice. I. The random-phase Green's function approximation. Phys. Rev. **139**, A1304-A1312 (1965).

Liu, L. The post-spinet phases of forsterite. Nature **262,** 770-772 (1976).

Loa, I., Kunc, K., Syassen, K., Krisch, M., Mermet, A., and Hanfland, M. Inelastic X-ray scattering in Cs under pressure. High Pressure Res. **23**, 1-5 (2003).

Long, G. J. and Grandjear, F. Mössbauer effect, magnetical and structural studies of wüstite, $Fe_{1-x}O$. Advanced in solid state chemistry **2**, 187-221 (1991).

Mao, H. K. A discussion of the iron oxides at high pressure with implications for the chemical and thermal evolution of the Earth. Carnegie Inst. Washington Yearbook, 510-518 (1974).

Mao, H. K., Xu, J. A., and Bell, P. M. Calibration of the ruby pressure gauge to 800 kbar under quasihydrostatic conditions. J. Geophys. Res. **91**, 4673-4676 (1986).

Mao, H. K., Wu, Y., Chen, L. C., Shu, J. F., and Jephcoat, A. P. Static compression of iron to 300 GPa and $Fe_{0.8}Ni_{0.2}$ alloy to 260 GPa: implications for composition of the core. J. Geophys. Res. **95,** 21737-21742 (1990).

Mao, H. K., Shu, J., Fei, Y., Hu, J., and Hemley, R. J. The wüstite enigma. Phys. Earth Planet. Int. **96**, 135-145 (1996).

Mao, H.-K., Shu, J., Shen, G., Hemley, R. J., Li, B., and Singh, A. K. Elasticity and rheology of iron above 220 GPa and the nature of the Earth's inner core. Nature **396**, 741-743 (1998).

Mao, W. L., Campbell, A. J., Heinz, D. L., and Shen, G. Phase relations of Fe-Ni alloys at high pressure and temperature. Phys. Earth Planet. Int. **155**, 146-151 (2005).

Maradudin, A. A., Montroll, E. W., and Weiss, G. H. *Theory of lattice dynamics*. Academic press, New York and London, pp.231-289 (1963).

McCammon, C. A. Magnetic properties of Fe_xO (x>0.95): Variation of Neél temperature. J. Magn. Magn. Mat. **104-107**, 1937-1938 (1992).

McCammon, C. A. Effect of pressure on the composition of the lower mantle end member Fe_xO. Science **259**, 66-68 (1993).

McCammon, C. A. Perovskite as a possible sink for ferric iron in the lower mantle. Nature **387**, 694-696 (1997).

McCammon, C. A. The paradox of mantle redox. Science **308**, 807-808 (2005).

McCammon, C. A., and Liu, L. G. The effects of pressure and temperature on nonstoichiometric wustite, Fe_xO; the iron-rich phase-boundary. Chem. Miner. **10**, 106-113 (1984).

McSkimin, H. J. Ultrasonic measurement techniques applicable to small solid specimens. J. Acoust. Soc. Am. **22**, 413-418 (1950).

McSkimin, H. J. Pulse superposition method for measuring ultrasonic wave velocities in solids. J. Acoust. Soc. Am. **33**, 12-16 (1961).

McQueen, R.G. and Marsh, S. P. Equation of state for nineteen metallic elements from shock-wave measurements to two megabars. J. Appl. Phys. **31**, 1253-1269 (1960).

Meade, C., and Jeanloz, R. Yield strength of MgO to 40 GPa. J. Geophys. Res. **93**, 3261-3269 (1988).

Mechie, J., Egorkin, A. V, Fuchs, K., Ryberg, T., Solodilov, L., and Wenzel, F. P-wave mantle velocity structure beneath northern Eurasia from long-range recordings along the profile Quartz. Phys. Earth Planet Int. **79,** 269-286 (1993).

Meng, Y., Weidner, D. J., Gwanmesia, G. D., Liebermann, R. C., Vaughan, M. T., Wang, Y., Leinenweber, K., Pacalo, R. E., Yeganeh-Haeri, A., and Zhao, Y. In situ high *P-T* X-ray diffraction studies of three polymorphs (α, β, γ) of Mg_2SiO_4. J. Geophys. Res. **98,** 22199-22207 (1993).

Merkel, S., Jephcoat, A. P., Shu, J., Mao, H.-K., Gillet, P., and Hemley, R. J. Equation of state, elasticity, and shear strength of pyrite under high pressure. Phys. Chem. Minerals **29**, 1-9 (2002).

Meyer, R., and Entel, P. Molecular dynamics study of iron-nickel alloys. Journal de Physique IV **5**, 123-128 (1995).

Miller, R. J., Pierre, M., Rose, T. S., and Fayer, M. D. A coherent photoacoustic approach to excited-state absorption spectroscopy: Application in the investigation of a near-resonant contribution to ultrasonic diffraction. J. Phys. Chem. **88**, 3021-3025 (1984).

Minervini, L., and Grimes, R. W. Defect clustering in wüstite. J. Phys. Chem. Solids **60**, 235-245 (1999).

Ming, L.-C., and Bassett. W. A. The postspinel phases in the Mg_2SiO_4-Fe_2SiO_4 system. Science **187,** 66-68 (1975).

Morosin, B. Exchange striction effects in MnO and MnS. Physical Review B **1**, 236-243 (1970).

Mueller, H. J., Lauterjung, J., Schilling, F. R., Lathe, C., and Nover, G. Symmetric and asymmetric interferometric method for ultrasonic compressional and shear wave velocity measurements in piston-cylinder and multi-anvil high-pressure apparatus. Eur. J. Mineral. **14(3)**, 581-589 (2002).

Narayanasamy, A., Nagarajan, T., Muthukumarasamy, P., and Radhakrishnan, T. S. Hyperfine field distribution in disordered binary alloys. J. Phys. F: Metal Phys. **9**, 2261-2274 (1979).

Nasu, S. High pressure Mössbauer spectroscopy using a diamond anvil cell. Hyperfine Interactions **90**, 59-75 (1994).

Nelson, K. A., Casalegno, R., Miller, R. J., and Fayer, M. D. Laser-induced excited state and ultrasonic wave gratings. J. Chem. Phys. **77**, 1144-1152 (1982).

Niesler, H., and Jackson, I. Pressure derivatives of elastic wave velocities from ultrasonic interferometric measurements on jacketed polycrystals. J. Acoust. Soc. Am. **86**, 1573-1585 (1989).

Nolet, G., Grand, S. P, and Kennett, B. L. N. Seismic heterogeneity in the upper mantle. J. Geophys. Res. **99,** 23753-23766 (1994).

Nowick, A. S. and Berry, B. S. *Anelastic relaxation in crystalline solids*. Academic Press, New York, 677 p. (1972).

Nye, J. F. *Physical properties of crystals*. Oxford University Press, New York, 329 p. (1987).

Occelli, F., Krisch., M., Loubeyre, P., Sette, F., LeToullec, R., Masciovecchio, C., and Rueff, J. P. Phonon dispersion curves in an argon single crystal at high pressure by inelastic X-ray scattering. Phys. Rev. B **63**, 224306, 1-8 (2001).

Ohno, I., Abe, M., Kimura, M., Hanayama, Y., Oda, H., and Suzuki, I. Elasticity measurement of silica glass under gas pressure. Am. Miner. **85**, 288-291 (2000).

Ohno, I., Harada, K., and Yoshitomi, C. Temperature variation of elastic constants of quartz across the $\alpha - \beta$ transition. Phys. Chem. Minerals **33**, 1-9 (2006).

Pacalo, R. E., and Graham, E. K. Pressure and temperature dependence of the elastic properties of synthetic MnO. Phys. Chem. Minerals **18**, 69-80 (1991).

Pasternak, M. P., Taylor, R. D., Jeanloz, R., Li, X., Nguyen, J. H., and McCammon, C. A. High Pressure Collapse of Magnetism in $Fe_{0.94}O$: Mössbauer Spectroscopy Beyond 100 GPa. Phys. Rev. Letters **79**, 5046-5049 (1997).

Peletminskii, S. V. Coupled magnetoelastic oscillations in antiferromagnetics. Soviet Physics JETP **37 (10)**, 321-324 (1960).

Piermarini, G. J. and Weir, C. E. A diamond cell for X-ray diffraction studies at high pressure. J. Res. Natl. Bur. Stand. A **66**, 325-331 (1962).

Poirier, J.-P. *Introduction to the Physics of the Earth's Interior, 2nd edition.* Cambridge University Press, Cambridge, 326 p. (2000).

Poirier, J. P. and Tarantola, A. A logarithmic equation of state. Phys. Earth Planet. Inter. **109**, 1-8 (1998).

Reichmann, H. J., Angel, R. J., Spetzler, H., and Bassett, W. A. Ultrasonic interferometry and X-ray measurements of MgO in a new diamond anvil cell. Am. Miner. **83**, 1357-1360 (1998).

Reichmann, H. J., and Jacobsen, S. D. High-pressure elasticity of a natural magnetite crystal. Am. Mineral. **89**, 1061-1066 (2004).

Rekhi, S., Dubrovinsky, L. S., and Saxena, S. K. Temperature-induced ruby fluorescence shifts up to a pressure of 15 GPa in an externally heated diamond anvil cell. High Pres.-High Temp. **31**, 299-305 (1999).

Rigden, S. M., Gwanmesia, G. D., Jackson, I., and Liebermann, R. C. Progress in high-pressure ultrasonic interferometry, the pressure dependence of elasticity of Mg_2SiO_4 polymorphs and constraints on the composition of tire transition zone of the Earth's mantle. In: *High-Pressure Research: Applications to Earth and Planetary Srience*, Vol. 3, edited by Syono. Y., and Manglmani, M. H. American Geophysical Union, Washington D.C., pp. 167-182 (1992).

Ringwood, A. E. The olivine-spinet transition in the Earth's mantle. Nature **178,** 1303-1304 (1956).

Ringwood, A. E. *Composition and Petrology of the Earth's Mantle*. McGraw Hill, New York, 618 p. (1975).

Ringwood, A. E. Composition of the core and implications for origin of the Earth. Geoehem. J. **11,** 111-135 (1977).

Ringwood, A. E., and Major, A. Synthesis of Mg_2SiO_4-Fe_2SiO_4 spinel solid solutions. Earth Planet. Sci. Lett. **1,** 241-245 (1966).

Ringwood, A. E., and Major, A. The system Mg_2SiO_4-Fe_2SiO_4 at high pressure and temperatures. Phys. Earth Planet. Int. **3,** 89-108 (1970).

Robbins, R. R., Jefferys, W. H., and Shawl, S. J. *Discovering astronomy, third ed.* John Wiley and sons Inc., New York, 540 p. (1995).

Rodbell, D. S., Jacobs, I. S., Oven, J. and Harris, E. A. Biquadratic exchange and the behaviour of some antiferromagnetic substances. Phys. Rev. Letters **11**, 10-12 (1963).

Rodbell, D. S., and Owen, J. Sublattice Magnetization and Lattice Distortions in MnO and NiO. J. App. Phys. **35**, 1002-1003 (1964).

Romanowicz, B. Global mantle tomography: progress status in the past 10 years. Ann. Rev. of Earth and Planet. Science **31**, 303-328 (2003).

Rooksby, H. P. Structure of NiO. Nature **152**, 304-305 (1943).

Sasakura, T., Suito, K., and Fujisawa, H. Measurement of ultrasonic wave velocities in fused quartz under hydrostatic pressures up to 6.0 GPa. In: *Proceedings of the XIth International Conference of the International Association for the Advancement of High Pressure Science and Technology (AIRAPT)*, vol. 2. Kiev Naukova Dumka, USSR, pp. 60-72 (1989).

Sasakura, T., Yoneda, H., Suito, K., and Fujisawa, H. Variations of the elastic constants of InSb near the covalent-metal transition. High Pressure Research **4**, 318-320 (1990).

Saxena, S. K., Chatterjee, N., Fei, Y. and Shen, G. *Thermodynamic data on oxides and silicates*. Springer-Verlag, Berlin and Heidelberg, pp. 263-269 (1993).

Saxena, S. K., Dubrovinsky, L. S., Haggkvist, P., Cerenius, Y., Shen, G., and Mao, H. K. Synchrotron x-ray study of iron at high pressure and temperature. Science **269**, 1703-1704 (1995).

Schilfgaarde, M., Abrikosov, I. A., and Johansson, B. Origin of the Invar effect in iron-nickel alloys. Nature **400**, 46-49 (1999).

Seehra, M. S., and Srinivasan, G. J. Magnetic studies of nonstoichiometric Fe_zO and evidence for magnetic defect clusters. Phys. C: Solid State Phys. **17**, 883 (1984).

Shaked, H., Faber, J., and Hitterman, R. L. Low-temperature magnetic structure of MnO: a high-resolution neutron-diffraction study. Phys. Rev. B **38**, 11901-11903 (1988).

Shearer, P. M. Seismic imaging of upper-mantle structure with new evidence for a 520-km discontinuity. Nature **344**, 121-126 (1990).

Shearer, P. M. Constraints on upper mantle discontinuities from observations of long-period reflected and converted phases. J. Geophys. Res. **96,** 18147-18182 (1991).

Shearer, P. M. Transition zone velocity gradients and the 520-km discontinuity. J. Geophys. Res. **101,** 3053-3066 (1996).

Shen, A. H., Reichmann, H. J., Chen, G., Angel, R. J., Bassett, W. A., and Spetzler, H. GHz ultrasonic interferometry in a diamond anvil cell: P-wave velocities in periclase to 4.4 GPa and 207 °C. In: *Properties of Earth and Planetary Materials at High Pressure and Temperature*, edited by Manghnani, M. H. and Yogi, T. American Geophysical Union, Washington D.C., pp. 41-61 (1998).

Shu, J., Mao H. K., Hu J., Fei Y. and Hemley R. J. Single-crystal X-ray diffraction of wüstite to 30 GPa hydrostatic pressure. N. Jb. Miner. Abh. **172**, 309-323 (1998).

Shull, C. G., Strauser, W. A., and Wollan, E. O. Neutron diffraction by paramagnetic and antiferromagnetic substances. Phys. Rev. **83**, 333-345 (1951).

Simons, B. Composition-lattice parameter relationship of the magnesiowusitte solid solution series. Ann. Rep. Geophys. Lab **79**, 376-380 (1980).

Sinelnikov, Y. D, Chen, G., Neuville, D. R., Vaughan, M. T., and Liebermann, R. C. Ultrasonic shear wave velocities of $MgSiO_3$ perovskite at 8GPa and 800K and lower mantle composition. Science **281**, 677–679 (1998).

Singh, A. K., Mao, H. K., Shu, J., and Hemley, R. J. Estimation of single-crystal elastic moduli from polycrystalline X-ray diffraction at high pressure: Application to FeO and iron. Phys. Rev. Lett. **80**, 2157-2160 (1998).

Sinogeikin, S. V., and Bass, J. D. Elasticity of majorite and a majorite–pyrope solid solution to high pressure: implications for the transition zone. Geophys. Res. Lett. **29 (2)**, 52–55 (2002).

Smart, J. S., and Greenwald, S. Crystal structure transitions in antiferromagnetic compounds at the Curie temperature. Phys. Rev. **82**, 113-114 (1951).

Solozhenko, V. L., Häusermann, D., Mezouar, and Kunz, M. M. Equation of state of wurtzitic boron nitride to 66 GPa. Appl. Phzs. Lett. **72**, 1691-1693 (1998).

Spetzler, H. A., Shen, G., Whitehead, S., and Getting, I. C. A new ultrasonic interferometer for determination of equation of state parameters of sub-millimeter single crystals. Pure and Appl. Geophys. **141**, 341-377 (1993).

Spetzler, H., Shen, A., Chen, G., Herrmannsdoerfer, G., Schulze, H., and Weigel, R. Ultrasonic measurements in a diamond anvil cell. Phys. Earth Planet. Int. **98**, 93-99 (1996).

Srinivasan, G., and Seehra, M. S. Nature of magnetic transitions in MnO, Fe_zO, CoO, and NiO. Phys. Rev. B **28**, 6542-6544 (1983).

Stacey, F. D. Theory of thermal and elastic properties of the lower mantle and core. Phys. Earth Planet. Int. **89,** 219-245 (1995).

Stacey, F. D. Thermoelasticity of a mineral composite and a reconsideratation of lower mantle properties. Phys. Earth Planet. Int. **106,** 219-236 (1998).

Stacey, F. D., and Isaak, D. G. Extrapolation of lower mantle properties to zero pressure: Constraints on composition and temperature. Am. Min. **85,** 345-353 (2000).

Steinle-Neumann, G., Stixrude, L., Cohen, R. E., and Gülseren, O. Elasticity of iron at the temperature of the Earth's inner core. Nature **413**, 57-60 (2001).

Stevenson, D. J. Models of the Earth's core. Science **241**, 611-619 (1981).

Struzhkin, V. V., Mao, H. K., Hu, J., Schwoerer-Böhning, M., Shu, J., Hemley, R. J., Sturhahn, W., Hu, M. Y. , Alp, E. E., Eng, P., and Shen, G. Nuclear Inelastic X-Ray Scattering of FeO to 48 GPa. Phys. Rev. Lett. **87**, 255501,1-255501,4 (2001).

Sumino, Y., Kumazawa, M., Nishizawa, O., and Pluschkell, W. The elastic constants of single crystal $Fe_{1-x}O$, MnO and CoO, and the elasticity of stoichiometric magnesiowustite. J. Phys. Earth **28**, 475-495 (1980).

Sutton, A. P. *Electronic Structure of Materials*. Oxford University Press, Oxford, 260 p. (1993).

Swamy, V., and Dubrovinsky, L. S. Bulk modulus of anatase. J. Phys. Chem. Minerals **62**, 673-675 (2001).

Swamy, V., Dubrovinsky, L. S., and Dubrovinskaia, N. A. Compressibility of baddeleyite-type TiO_2 from static compression to 40 GPa. J. Alloys Comp. **340**, 46-48 (2002).

Takahashi, T., and Bassett, W. A. A high pressure polymorph of iron. Science **145**, 483-486 (1964).

Tebble, R. S., and Craik, D. J. *Magnetic materials*. Wiley-Interscience, New York, 181 p. (1969).

Vereschagin, L. F. X-ray study of solids at high pressure. In: *Physics of Solids at High Pressures*, ed. by Tomizuka, C. T. and Emrick, R. M. Academic Press, New York, pp. 460-477 (1965).

Vidale, J. E., and Earle, P. S. Fine-scale heterogeneity in the Earth's inner core. Nature **404**, 273-275 (2000).

Vinet, P., Ferrante, J., Smith, J. R., and Rose, J. H. A universal equation of state for solids. J. Phys. C **19**, L467-L473 (1986).

Vinet, P., Rose, J. H., Ferrante, J., and Smith, J. R. Universal features of the equation of state of solids. J. Phys.: Condens. Matter **1**, 1941-1963 (1989).

Vocadlo, L., Alfe, D., Gillan, M. J., Wood, I. J., Brodholt, J. P., and Price, G. D. Possible thermal and chemical stabilization of body-centred-cubic iron in the Earth's core. Nature **424**, 536-539 (2003).

Walck, M. C. The *P*-wave upper mantle structure beneath an active spreading center: the Gulf of California. Geophys. J. R. Astronom. Soc. **76**, 697-723 (1984).

Webb, S. L., Jackson, I., and Fitzgerald, J. D. High-pressure elasticity, shear-mode softening and polymorphism in MnO. Phys Earth Planet Inter **52**, 117-131 (1988).

Weidner, D. J. A mineral physics test of a pyrolite mantle. Geophys. Res. Lett. **12,** 417-420 (1985).

Weidner, D. J. Mantle model based on measured physical properties of minerals. In: *Chemistry and Physics of Terrestrial Planets*, edited by Saxena, S. K. Springer-Verlag, New York, pp. 251-274 (1986).

Weidner, D. J., and Ito, F. Mineral physics contraints on a uniform mantle composition. In: *High-Pressure Research in Mineral Physics*, edited by Manghnani, M. H. and Syono, Y. American Geophysical Union, Washington, D.C., pp. 439-446 (1987).

Welberry, T. R. and Christy, A. G. Defect distribution and the diffuse X-ray diffraction pattern of wüstite, $Fe_{1-x}O$. Phys Chem Minerals **24**, 24-38 (1997).

Willis, B. T. M., and Rooksby, H. P. Change of structure of ferrous oxide at low temperature. Acta Cryst. **6**, 827-831 (1953).

Yan, Y.-X., Cheng, L.-T., and Nelson, K. A. Impulsive stimulated scattering. In: *Advances in Non-linear Spectroscopy*, edited by Clark, R. J. H., and Hester, R. E. Wiley, New York, pp. 299-355 (1998).

Yoneda, H. Pressure derivatives of elastic constants of single crystal MgO and MgAl$_2$O$_4$. J. Phys. Earth **38**, 19-55 (1990).

Yoneda, H., and Morioka, M. Pressure derivatives of elastic constants of single crystal forsterite. In: *High Pressure Research: Application to Earth and Planetary Sciences*, edited by Syono, Y., and Manghnami, M. H. American Geophysical Union, Washington, D. C., pp. 207-214 (1992).

Yoo, C. S., Akella, J., Campbell, A. J., Mao, H. K., and Hemley, R. J. Phase diagram of iron by in situ x-ray diffraction: implications for Earth's core. Science **270**, 1473-1475 (1995).

Yoo, C. S., Cynn, H., Söderlind, P., and Iota, V. New β(fcc)-cobalt to 210 GPa. Phys. Rev. Lett. **84**, 4132-4135 (2000).

Zaug, J., Abramson, E., Brown, J. M., and Slutsky, L. J. Elastic constants, equations of state and thermal diffusivity at high pressure. In: *High-Pressure Research: Applications to Earth and Planetary Srience*, vol. 3, edited by Syono. Y., and Manglmani, M. H. American Geophysical Union, Washington D.C., pp. 157-166 (1992).

Zaug, J., Abramson, E. H., Brown, J. M., and Slutsky, L. J. Sound velocities in olivine at Earth mantle pressure. Science **260**, 1487–1489 (1993).

Zha, C. S., Mao, H. K., and Hemley, R. J. Elasticity of MgO and a primary pressure scale to 55 GPa. Proc. Natl. Acad. Sci. **97**, 13494-13499 (2000).

Zhang, J. Effect of defects on the elastic properties of wüstite. Phys. Rev. Letters **84**, 507-510 (2000).

Zhao, D. and Kayal, J. R. Impact of seismic tomography on earth sciences. Seismology **79**, 1208-1214 (2000).

Zou, G., Mao, H. K., Bell, P. M., and Virgo D. High-pressure experiments on the iron oxide wüstite ($Fe_{1-x}O$). Carnegie Institution of Washington Yearbook **79**, 374-376 (1980).

List of publications

Kantor, A. P, Jacobsen, S. D., Kantor, I. Y., Dubrovinsky, L. S., McCammon, C. A., Reichmann, H. J., and Goncharenko, I. N. Pressure-induced magnetization in FeO: evidence from elasticity and Mössbauer spectroscopy. Phys. Rev. Lett. **93**, 215502,1-215502,4 (2004).

Jacobsen, S. D., Reichmann, H. J., **Kantor, A. P.,** and Spetzler, H. A. A gigahertz ultrasonic interferometer for the diamond anvil cell and high-pressure elasticity of some iron-oxide minerals. In: *Advances in high-pressure technology for geophysical applications* edited by Chen, J., Wang, Y., Duffy, T. S., Shen, G., and Dobrzhinetskaya, L. F. Elsevier, Amsterdam, pp. 25-49 (2005).

Kantor, A. P., Dubrovinsky L. S., Dubrovinskai, N. A., Kantor, I. Yu., and Goncharenko, I. N. Phase transitions in MnO and FeO at low temperatures: A neutron powder diffraction study. J. Alloys Compounds **402**, 42-45 (2005).

Kantor I.Yu., Dubrovinsky L.S., **Kantor A.P.,** Urusov, V. S., McCammon, C. A., and Crichton, W. Trigonal Distortion of Ferropericlase $(Mg_{0.8}Fe_{0.2})O$ at High Pressures. Doklady Physics **403**, 343-345 (2005).

Kantor, A. P., Kantor, I. Yu., Dubrovinsky, L. S., Krisch, M., Bossak, A., Dmitriev, V. P., and Urusov, V. S. Measuring the Speed of Sound in an Iron–Nickel Alloy at High Pressure by Inelastic X-Ray Scattering. Doklady Physics **51**, 584-587 (2006).

Kantor, **A. P.,** Kantor, I. Yu., Kurnosov, A. V., Kuznetsov, A. Yu., Dubrovinskaia, N. A., Krisch, M., Bossak, A. A., Dmitriev, V. P., Urusov, V. S., Dubrovinsky, L. S. Sound wave velocities of fcc Fe-Ni alloy at high pressure and temperature by mean of inelastic X-ray scattering. Phys. Earth Planet. Int., *in press* (2007).

Kantor, I. Yu., Dubrovinsky, L., McCammon, C., Dubrovinskaia, N., Goncharenko, I., **Kantor, A. P.,** Kuznetsov, A., and Crichton, W. FeO and MnO high-pressure phase diagrams: relations between structural and magnetic properties. Phase Transition **80**, 1151-1163 (2007).

Erklärung

Hiermit erkläre ich, dass ich die vorliegende Arbeit selbständig verlaßt und keine anderen als die von mir angegebenen Quellen und Hilfsmittel benutzt habe.

Ferner erkläre ich, daß ich nicht anderweitig versucht habe, mit oder ohne Erfolg, eine Dissertation einzureichen und auch keine gleichartige Doktorprüfung an einer anderen Hochschule endgültig nicht bestanden habe.

Bayreuth, im Juli 2007

Anastasia Kantor.